
STORE—
Osborne
A 10.00
A 10.00 TOTL
A 10.00 AMT TEND
A 00.00 BAL DUE
THANK YOU
6771 24 JUN 67

THE MECHANISM OF MELTING OF INDIUM

by

Adam Osborne

A dissertation submitted to the Faculty of the University of Delaware in partial fulfillment of the requirements for the degree of Master of Chemical Engineering.

June, 1966

ACKNOWLEDGEMENT

This work was performed under the direction of Dr. J. M. Schultz. For his capable direction, and his patient and invaluable assistance in interpreting the experimental data, the author is grateful.

SUMMARY

It is the purpose of this thesis to shed light on the mechanisms whereby solid crystalline substances melt. Owing to the vastness of the field encompassed and the time consuming nature of the experimental work, one crystalline solid, indium metal, was selected for investigation. Indium metal has the advantages of a low melting point, a simple crystal structure, and commercial availability at very high purity.

Polycrystalline samples of indium metal were heated in an inert atmosphere, and X-ray diffraction patterns were made at temperatures ranging from the melting point to 20°F below the melting point. By analysis of the diffraction patterns, in conjunction with data for the cold metal, the effect of heating on the crystalline structure was deduced. It was the original intent to concentrate the investigation on the effect of very small temperature increments, of the order of 1/3°F. However, physical considerations of the experimental equipment made this impossible, and the complexity of the effects detected further de-emphasised the change-with-temperature aspects of this work.

CHAPTER I

PREVIOUS WORK

Previous work on melting may be considered in four catagories:

a) Early general statements on the cause of melting.

b) Thermal and other physical property determinations close to the melting point.

c) Investigations of the crystalline defects associated with melting.

d) Theroretical and experimental evaluations of the causes of crystal defects.

Early statements on the cause of melting were, in general, intelligent guesses, but they formed the basis for later work. Lindemann (1) assumed solids to be made up of elementary oscillators, and his work was the foundation for later theories based on molecular force fields. Frenkel (2) suggested that melting was an amorphatizing process starting well below the melting point. He extended this work to

develop the theory of "heterophase fluctuations." (3,4) According to this theory, a phase change is caused by a build up of agglomerations of "heterophase molecules," to surpass a critical level at the melting temperature. These "heterophase molecules" are considered to be transiently present, causing fluctuating agglomerations at all times. Following a similar line of thought, Brillouin (5) suggested that the melting point is the temperature at which crystal rigidity coefficients vanish.

Ubbelohde's work on the solid state abnormalities of octadecane (6) is conveniently reviewed in conjunction with the work of Frenkel and Brillouin. Ubbelohde ascribed the abnormalities close to the melting point of octadecane as owing to "premelting," which he found to be a purely solid state phenomenon, rather than the formation of liquid pockets within the solid structure. This conclusion was arrived at for two reasons:

a) It was calculated that if impurities should give rise to liquid pockets below the melting temperature, the concentration of such impurities which would be necessary, if they were to account for the abnormalities in specific heat, would be impossibly large.

b) X-ray studies showed that the impurities

in octadecane formed almost perfect solid solutions, and the maximum depression of the setting point never exceeded 1.5°C.

Other work on physical properties close to the melting point include Roberts' (7) determination that the expansion of Bismuth decreases rapidly near the melting point, and the later comparative work of Hachkovsky and Stralkov (8). The latter authors worked with zinc and cadmium, and found a rapid increase in their rate of expansion, perpendicular to the hexagonal crystal plane, starting 5°C below the melting point. The work of Jack and Sebba (9) on the melting of gallium is of particular interest. They conclude that melting is propagated along individual lattice planes. The work is considered in greater detail later.

Much work is reported on crystalline changes accompanying the process of melting. Working with paraffins and ketones, Oldham and Ubbelohde (10) showed that melting was associated with the break up of long range order, caused by lattice flaws. Siol (11) gave the cause of melting as lattice perturbations consisting of pairs of atoms which are displaced with respect to each other. Their interaction requires a critical concentration which characterizes the molten state, at which individual pairs start to unite into dislocation rings.

The origins of crystal distortion have been variously ascribed to lattice vibration and interstitial sites (12, 13, 14). Utilising the theory of Eshelby (15), Feder and Nowick (16) measured the vacancy concentrations in titanium and aluminium, by experimentally determining the difference between crystalline expansion as measured by X-ray diffraction and dilatometry. Lukasik (17) attempted to measure the heterophase fluctuations in liquid benzene and o-cresol, close to the melting point.

Lennard - Jones and Devonshire (12) are responsible for most of the fundamental theoretical work on melting. They assumed that melting was the result of an order-disorder process in a solid lattice. If the normal lattice sites of a crystal are termed α sites, then they assumed the existance of an equal number of abnormal β sites, displaced from the α sites such that each α site would be surrounded by n β sites, and each β site would be surrounded by n α sites. The energy of transition from an α to a β site would be large when very few β sites were occupied, but would fall to zero when α and β sites were equally occupied. The authors calculated the partition function for a solid with any fraction of the β sites occupied, and thus showed the co-operative effect of order-disorder on the solid lattice. From the disordered partition function, the authors were able to calculate free energy functions in good agree-

ment with the data for the solid phase of the inert gases. Theoretical work along the lines of Lennard - Jones and Devonshire is limited to the very simplest solids, for which intermolecular force field data are accurately known.

CHAPTER II

THE PHYSICAL AND CRYSTALLINE PROPERTIES OF INDIUM

Indium metal has a face centered tetragonal crystal structure. Its melting temperature is 311°F. It is a soft, white metal, malleable and ductile, with a tin like "squeal" on being deformed. Chemically it is relatively inert, with surface oxidation occurring slowly at room temperature (18).

The commonly listed properties of indium are given In Table 1. The values for the x and y axes are taken from A.S.T.M. data.

In Table 2 are listed the more intense X-ray diffraction peaks for indium (19). The planes are referred to by their Miller indices. On Figs. 1a to 1g the planes in Table 2 are illustrated.

Symbol	In
Valance	3, 2 and 1
Atomic Number	49
Atomic weight	114.8
Atomic radius	1.40 (Wycoff) 1.569 (Goldschmidt)
Atomic volume	15.7
Melting point	311°F
Boiling point	2642°F
Density (gm/cc)	7.3 (68°F)
Linear coefficient of thermal expansion	0.000033 (68°F)
Coefficient of cubical expansion	0.000125 (68°F)
Specific heat (cals/gm)	0.0568
Thermal conductivity (cal/cc/sec/°C)	0.057
Crystal lattice	Face centered tetragonal; x, y 3.2517 A z 4.951 A
Color	Silver-white with a bluish tinge.

Table 1 THE PHYSICAL PROPERTIES OF INDIUM

2θ	hkl	I/I_o	$d_{hkl}(xz)$	d_{hkl}(Å)(cold)
32.96	101	100	$\frac{xz}{\sqrt{x^2+z^2}}$	2.715
36.32	002	21	0.5z	2.471
39.17	110	36	0.707x	2.298
54.47	112	24	$\frac{xz}{1.414\sqrt{z^2+2x^2}}$	1.683
56.60	200	12	0.5x	1.625
63.20	103	16	$\frac{xz}{\sqrt{z^2+9x^2}}$	1.470
67.02	211	23	$\frac{xz}{\sqrt{5z^2+x^2}}$	1.395

Table 2 THE PRINCIPAL X-RAY DIFFRACTION PEAKS FOR INDIUM

(a) 101 Plane

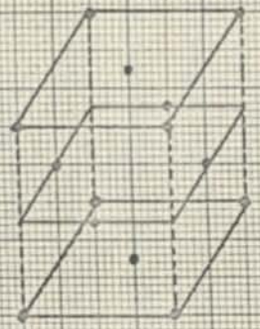

(b) 002 Planes

(c) 110 Plane

(d) 112 Plane

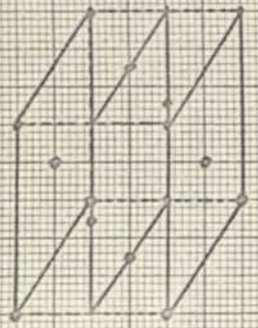

(e) 100 Planes

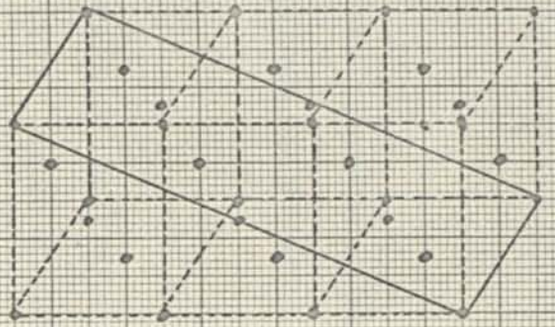

(f) 103 Plane

(g) 211 Plane

Figure 1 Principal Planes of Reflection of the Indium Crystal Lattice

Factors Effecting X-Ray Diffraction Peak Intensity and Width

The crystal lattice properties which are listed below, and the changes in dimensions which occur, are all well understood phenomena, described fully in most texts on X-ray diffraction. The purpose of this section is to list the types of phenomena found in imperfect and hot crystal lattices, and to indicate the way such phenomena will manifest themselves in an X-ray diffraction pattern. One text book (20) is drawn from heavily.

1) Crystal Size

The Bragg equation is the condition which must be satisfied in order for X-ray diffraction to occur:

$$\lambda = 2d \sin \theta \qquad (1)$$

The width of the angular domain of reflection may be investigated by extending Equation (1). Since X-rays are not completely monochromatic, if the angle of incidence for part of the spectrum is θ, for another part it will be $\theta + \varepsilon$. The path difference from one plane to the next is then $2d \sin (\theta + \varepsilon)$, and

$$2d \sin (\theta + \varepsilon) = \lambda + d\varepsilon \cos \theta \qquad (2)$$

Adding N waves of the same amplitude but phase difference 2ϕ,

where

$$2\phi = \frac{4\pi d}{\lambda} \epsilon \cos\theta \tag{3}$$

using the Fresnel Construction (20) we obtain for the amplitude:

$$\sum A = \frac{A \sin N\phi}{\sin \phi} \tag{4}$$

The intensity reflected at $\theta + \epsilon$ is:

$$I(\epsilon) = A^2 \frac{\sin^2 N\phi}{\sin^2 \phi} \tag{5}$$

Since I becomes nearly zero for $n\phi > \pi$, or $\epsilon > \frac{\lambda}{2Nd \cos\theta}$, we see that the width of the angular domain of reflection is inversely proportional to Nd, or to the thickness of the crystal. This is indicated in the approximate Scherrer equation for X-ray diffraction peak width in terms of crystal size:

$$B = \frac{\lambda}{L \cos\theta} \tag{6}$$

where B is the width of the peak at half maximum intensity, and L has units of length, and is characteristic of crystal size. It should be noted that changes in crystal size will cause peak broadening which is uniform for peaks of ascending order, being inversely proportional to the cosine of the Bragg angle of incidence.

2) Peak Broadening Caused by Lattice Distortion

Lattice distortion is caused by dislocations, vacancies in the lattice, or by interstitial sites. In each case there results a non-uniform force field on the surrounding sites, which cause a strain in the lattice. Distortion manifests itself by altering the apparent crystal size L, according to Equation 7:

$$L = \frac{\int y(t)td}{Y(0)} \qquad (7)$$

where y(t) is equal to the product of the structure factors situated at the extremes of a vector t. y(t) is usually ascribed a simple empirical form, one common example being (20):

$$y(t) = \exp(-\gamma|t|) \qquad (8)$$

What must be noted is that the effect of distortion on peak width will vary from peak to peak, depending on the assumed form for y(t).

3) Planar and Linear Disorder

Planar disorder results from lattice planes remaining parallel to each other, but displaced with respect to nearest neighbors. The effect of planar disorder is to increase sharply the intensity of diffraction by the dis-

ordered planes, since the scattering is being concentrated in narrow regions instead of being distributed uniformaly throughout the unit cell. Where the degree of planar disorder is large, scattering is limited to the rows of the reciprocal lattice which are normal to the lattice planes whose structure is intact. Where the degree of planar disorder is small, other reflections are not extinguished, but they may be broadened and displaced. Wagner, Tetelman and Otte (21) discuss layer faults in body centered cubic and face centered cubic crystals. Layer faults are planar disorders accompanied by a change in interplanar distance. They are usually caused by work hardening in metals.

Linear disorder results when rows remain parallel, but become arranged irregularly. Scattering is then concentrated on a family of paralled planes, normal to the rows, and spaced by a distance 1/a, a being the period of the linear lattice.

4) Thermal Disorder

Thermal disorder is the result of greater movement of the atoms or molecules in a crystal, caused by an increase in temperature. These vibrations cause a decrease in diffracted intenstiy, since the occupation probability density decreases at the nodes. Thermal disorder does not cause peak broadening. This is in contrast to long range

disorder, in which the lattice nodes are not fixed, but the distance between neighboring atoms can vary within given limits about a mean interval a. Long range disorder does produce peak broadening, the broadening of reciprocal space nodes increasing with increasing 2θ. On account of the problems of focusing, the peak intensity data obtained were not good enough to establish the precise extent to which thermal disorder was present.

5) Thermal Expansion

Heating a crystal causes changes in the lattice constants. A cubic crystal usually expands uniformly, whereas in this work we find that indium, a tetragonal crystal, expands non-uniformly, and tends towards cubic symmetry. There results a change in d_{hkl}, which, to satisfy Equation (1), causes a peak shift.

6) Long Range Disorder

Long range disorder is determined by first nearest neighbor statistic only. Consider a crystal lattice in which the distance between successive points varies about an average value a, with a probability density h(x), as in Fig. 2 (a) and (b). Since the quantity h(x) is normalized,

$$\int_0^\infty h(x)dx = 1 \qquad (9)$$

and its average value is:

$$a = \int_0^\infty xh(x)dx \tag{10}$$

It can than be shown that the characteristic crystal size L, as measured by the Scherrer equation, is made up of two contributions, one actually due to crystal size, the other owing to long range disorder, according to Equation (11):

$$\frac{1}{L} = \sqrt{\Delta s^2 + \left(\frac{1}{N a}\right)^2} \tag{11}$$

where Na equals the length due to crystal size, and Δs is the contribution of long range disorder. Δs is given by:

$$\Delta s = \frac{1}{a} \pi^2 \left(\frac{\phi}{a}\right)^2 \tag{12}$$

in which

$$\int_0^\infty h(x)(x - a)^2 \, dx = \phi^2 \tag{13}$$

Solving Equation 13, and using Equation 9, we get:

$$\phi^2 = \int_0^\infty x^2 h(x)dx - 2a^2 + a^2 \tag{14}$$

or using Equation 10:

$$\phi^2 = \overline{a}^2 - a^2 \tag{15}$$

Thus

(a)

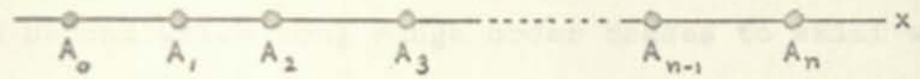

(b)

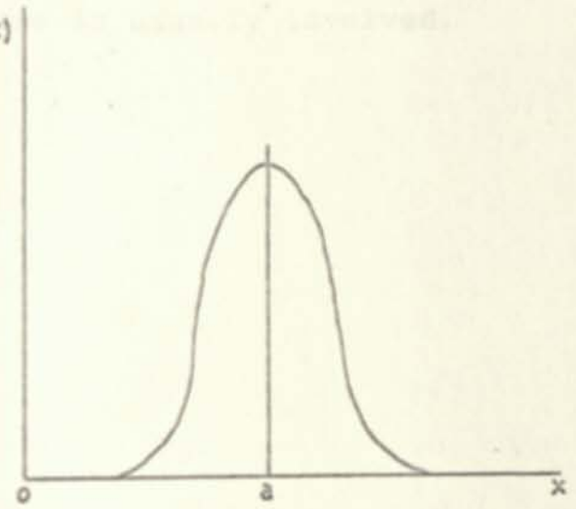

Figure 2 (a) IRREGULAR ONE-DIMENSIONAL LATTICE

(b) DISTRIBUTION FUNCTION H(X) OF THE DISTANCE BETWEEN CLOSE NEIGHBORS.

$$\bar{a} = [a^2 + \phi^2]^{1/2} \qquad (16)$$

An estimate of Δs therefore allows us to estimate the lattice length beyond which long range order ceases to exist with respect to the origin.

7) Phase Changes

The effect of phase changes is usually to produce and entirely new diffraction pattern, since a change in crystal structure is usually involved.

CHAPTER III

EXPERIMENTAL

X-Ray Equipment

A Picker X-ray diffractometer was employed, utilizing copper radiation. Settings were as follows:

Generator:	35 Kvolts
	16 milliamps
Radiation Analyzer:	Gain 4.8
	Mode II A = 1.3
	B = 9.3
	Scalar Time off
	Ratemeter variable cps.
	TC = 3 seconds
Optics:	2° incident beam soller collimator
	2° incident beam aperture
	2° diffracted beam soller collimator
	2° diffracted beam aperture
	0.20° receiving slit
	Nickel filter (0.0005")

Experimental Equipment

The overall layout in relation to the X-ray equipment is shown in Figure 3.

The Furnace

The furnace consisted of a transite box, 4" x 4" x 6", with a 1" wide mylar X-ray window on three sides. The transite walls were lined on the inside with bright copper to reduce radiation heat loss. The walls were 1/4" thick. The box was mounted at the base with a replica of the base of the Picker slide holder. The top face was a removable lid, to the underside of which a teflon slide holder was centrally attached, as seen in Figure 4. Helium entry and exit nozzles were situated at the lower and upper edges of opposite faces of the furnace.

A two-part heating element was employed, as described below. The main element was accordianed in the bottom of the furnace. A small thermal stablizing element surrounded the sample and was attached to the lid. (See Figures 4 and 5)

The Heating Element

The heating element was designed to minimize temperature gradients within the furnace. Accordingly, a heating element of very large surface area and low temper-

ature was employed. In fact, the heating element was designed to operate at only $40^{\circ}F$ above the temperature of the furnace. The element was constructed using 2" x 0.10" Kanthal heating strip. The design criteria were as follows:

The rate of heat loss from the furnace, was determined experimentally at $310^{\circ}F$, by inserting a heater and reducing the voltage till the temperature remained constant. The heater wattage was then 335 watts. Thus

Rate of heat loss $= 335 \times 3.415$

$= 1142$ BTU/Hr.

Let heater surface temperature $= 350^{\circ}F$

Then by Stephan's law, heat radiated

$= 0.173 \times 10^{-8} \times (8.1)^4 \times 10^8$

$= 750$ BTU/Hr. $ft.^2$

where the heating element is black faced

Let the heating strip have a resistance of Ω ohms/ft., and a surface area of s sq. in./ft. Then

$$\frac{s}{\Omega} = \frac{1.525 \times 144}{R}$$

where R is the total resistance of the heating element. The most suitable heating element with the above s/Ω value was found to be Kanthal D.DS strip 2" x 0.01". For this strip,

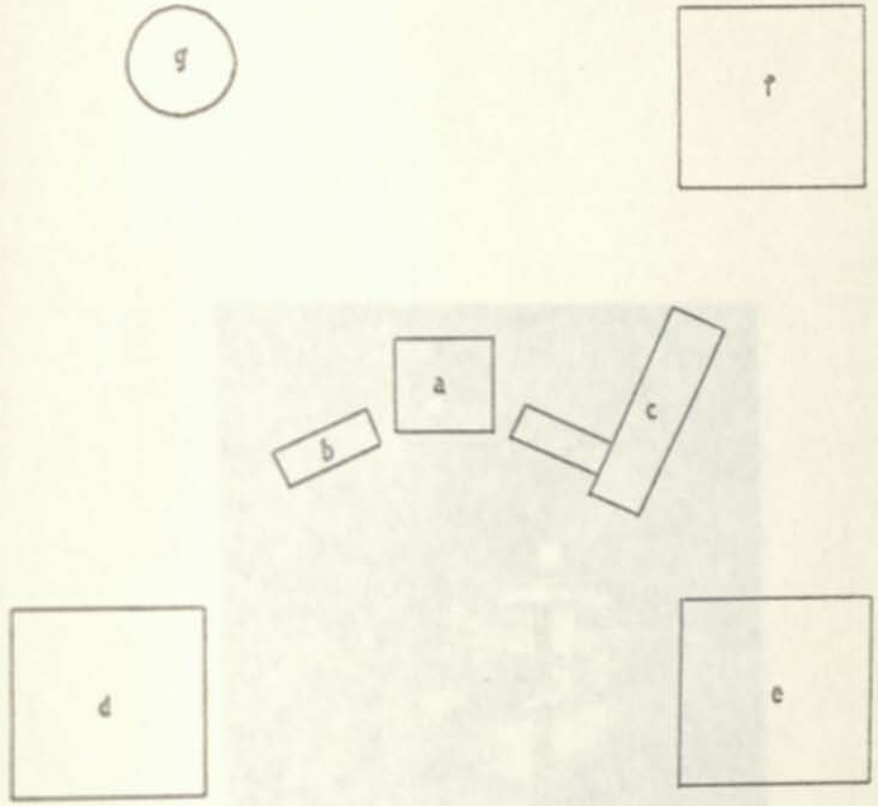

a furnace

b gieger counter and receiving apature

c X-ray tube and incident beam collermator

d radiation analyzer

e X-ray generator

f heating element power generator

g helium bottle

Figure 3 OVERALL EQUIPMENT LAYOUT

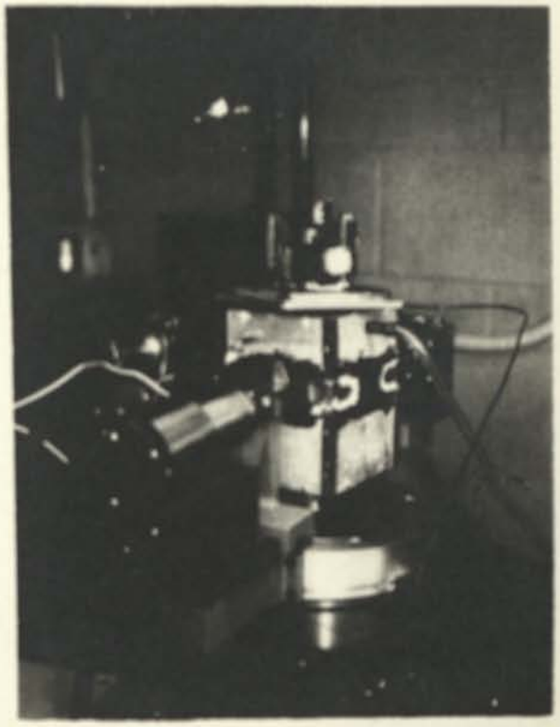

Figure 4 THE FURNACE, SHOWING THE SLIDE HOLDER AND STABLIZING HEATING ELEMENT.

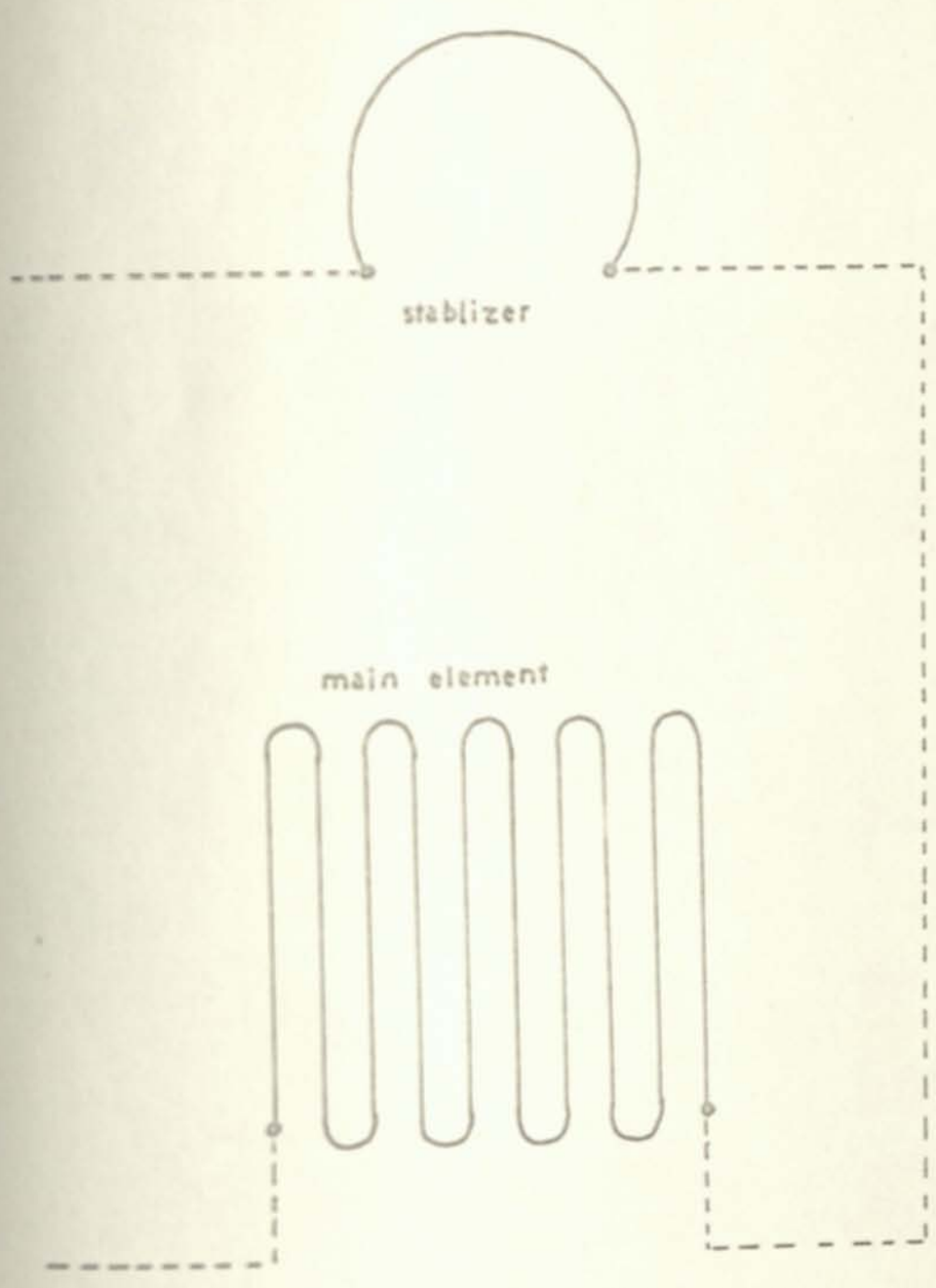

Figure 5 THE HEATING ELEMENTS

$$\frac{S}{\Omega} = 1513$$

so $R = 0.145$ ohms

and since the total wattage = 335 walts,

required heater voltage = 6.96 volts.

When the above heater was fabricated, the required voltage was found to vary from 8.0 volts when all the junctions were clean and bright, to 10.0 volts when the contacts had become tarnished. The discrepency in voltage was due to the resistance of the electric leads, which, even though thick copper was used, was significant compared to the 0.145 ohm resistance of the heating element.

Heating Element Current Generator

The heating element current generator is shown in Figure 6, and diagramatically in Figure 7. The system is made up of:

a) A voltage regulator to stablize line voltage. Stable line voltage was of the utmost importance, since temperature was maintained in the furnace by passing a steady current through the heating element, without any controller.

b) A transformer to step up the amperage and

step down the voltage.

c) A 20 ampere Variac to provide current control.

d) A voltmeter to measure the power input.

Power was taken straight from the Variac to the heating element.

Figures 8 and 9 are further views of the equipment.

Preparation of Samples

Indium samples were prepared by cutting thin wafers of the metal from a bar, using a microtome. The samples were of the order of 0.01" thick. Each sample had a smooth side, next to the microtome blade when the sample was cut, and a rough side. The samples were mounted on microscope slides with the rough side facing the X-ray beams. The rough side would most closely approximate a powder. The adhesive used was Dow Corning Silastic bathtub caulk. This is a silicone material which was found to be inert, and temperature resistant in the experimental temperature range encountered.

Run Proceedure

A freshly cut sample of indium, mounted on a slide,

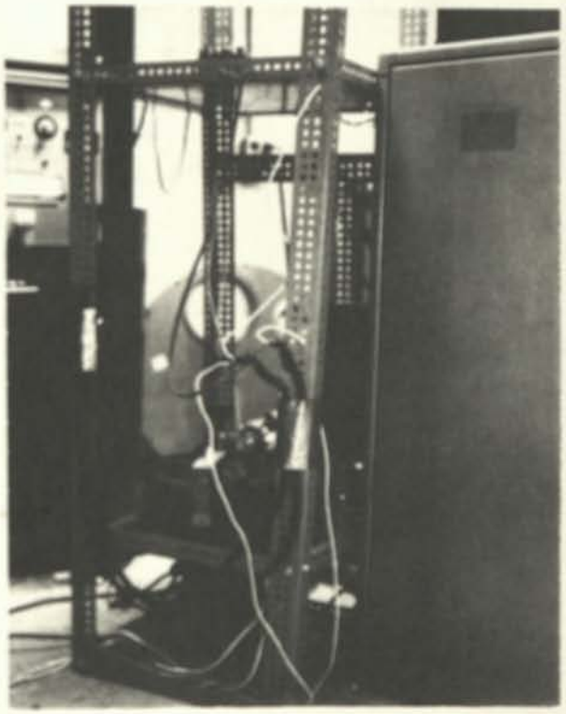

Figure 6 POWER TRANSFORMING AND CONTROL EQUIPMENT FOR THE HEATING ELEMENT.

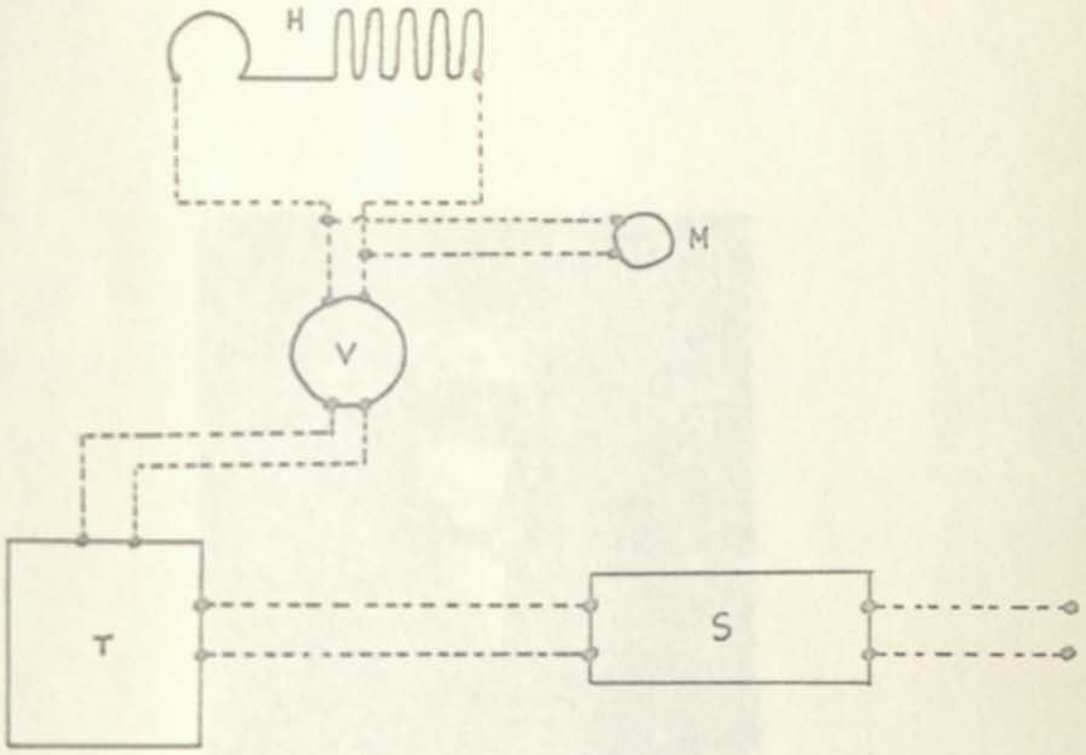

H heating element

M voltmeter

S voltage stablizer

T transformer

V variac

Figure 7 DIAGRAMATIC REPRESENTATION OF FURNACE HEATING SYSTEM.

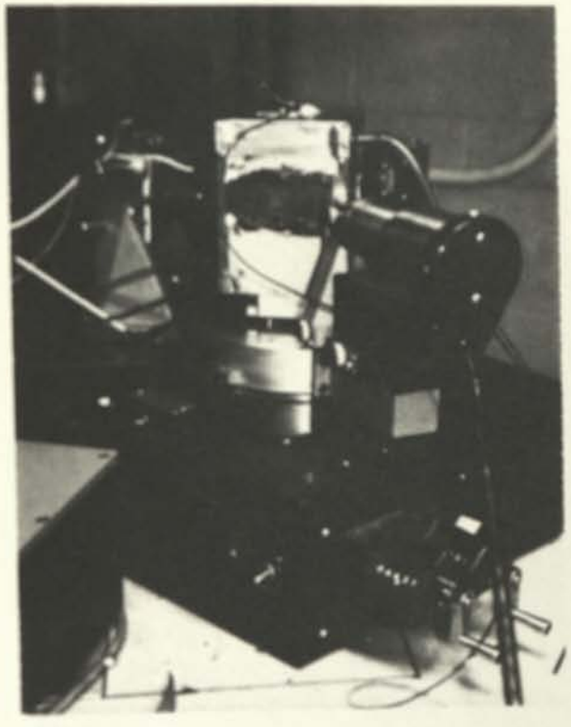

Figure 8 THE FURNACE, SEALED FOR A HIGH TEMPERATURE RUN.

Figure 9 GENERAL LAYOUT OF EQUIPMENT.

was installed in the slide holder. Taking care that the X-ray tube and analyzer had been on for at least twenty minutes in order to warm up and stablize, the sample was brought into sharp focus at 2θ = 32.96°, the angle of maximum intensity. One peak, or all seven peaks, depending on the nature of the run, were then scanned at room temperature. The furnace was then sealed with heating tape to make it relatively gas tight, and it was flushed out with helium gas. A positive pressure of about 1/2" of water was maintained with the helium inside the furnace.

The furnace was heated rapidly to about 290°F, at which temperature the voltage was cut back and marginally adjusted until the required temperature was reached. Temperature was recorded using a potentiometer and thermocouple, with the reference junction in melting ice.

Two type of run were made. During the first type of run, the temperature was stablized, and all seven peaks were scanned before proceeding to the next highest temperature. With the second type of run just one peak was scanned repeatedly at small temperature increments. Owing to the difficulties inherent in focusing, as described below, the second type of run proved more useful, since periodic small adjustments to the focus were all that were required. Each peak was scanned at a 2θ speed of 1/4° per sec.

The sample was always melted, and the potentiometer was callibrated using this melting temperature. The melting point was easily detected by the sudden disappearence of peaks. The furnace was then cooled, and a room temperature scan of the cold sample was made.

It was found necessary to operate the furnace at night, when the line voltage was steady. During the day fluctuations in the line voltage did not allow a constant temperature to be maintained. At night the temperature could be maintained absolutely constant over intervals as small as $1/3^{o}F$. Though some experience was necessary to gain the facility to control temperature without a controller, once this facility had been acquired, the task was relatively simple, requiring only constant supervision of the equipment. Care was taken not to allow the temperature to rise and then fall back to the required value, as the changes with temperature had been found not to be reversible. The most accurate temperature control obtained with and automatic controller was $2^{o}F$.

Discussion of Experimental Proceedure

Indium slowly oxidizes at room temperature. It was found that samples could not be kept more than twenty-four hours without a noticable decrease in peak intensity.

The approximation of the rough side of the indium

samples to a powder was found to be excellent.

Focusing the indium sample to obtain peaks of maximum intensity was made extremely difficult by the physical limitations imposed on the design of the furnace. These limitations were:

1) The furnace had to fit in the space between the incident and receiving soller collimators, allowing 2θ movement. Also, the level of the sample was fixed by the position of the X-ray beam. Thus a very severe limitation was placed on the dimensions of the box.

2) The occupation of a large part of the volume of the furnace by the heating element further limited the extra design features that could be included. Heating systems based on recirculating hot helium were made impractical by the necessary mylar windows, which would have made a gas tight furnace difficult and costly to fabricate.

3) The furnace could not be a large radiator of heat, since X-ray tubes are sensitive to environmental temperature changes, altering the intensity generated. The furnace therefore had to be well insulated.

The fixing of the slide holder to the lid of the furnace was unsatisfactory, since it introduced possible

lateral motion of the slide. That the slide was correctly centered could be assured by obtaining a good intensity peak at the correct 2θ angle. Movement of the slide by thousandth of an inch could result in complete loss in intensity. Since focusing was a trial and error proceedure, it was by necessity time consuming, and runs were eventually designed to avoid refocusing as much as possible, by scanning one peak per run.

In the light of the experience gained by this work, it is possible to make certain recommendations for an improved furnace design. They are:

1) The large surface area heating element should be replaced by a number of short parallel heating wires, placed in front of the sample, and independently controlled to obtain a zero temperature gradient across the sample (22).

2) With a smaller volume allowable, the furnace should be made of steel and insulation, with a reinforced mylar window ring, such that a gas tight press fit could be achieved.

3) The slide holder should be mounted on the base of the furnace. Such a unit should be fabricated with extreme accuracy of dimensions, insuring that the sample would at all times be correctly focused. Otherwise the sample could be permanently slightly out of focus, with no means for

correction.

A design based on the above would be costly to make, but the cost would be justifiable if future applications were anticipated.

CHAPTER IV

RESULTS OBTAINED

Three measurements were made of each peak; they were the peak intensity, I, the change in 2θ angle, Δ, and the peak width at half intensity, B.

Peak intensities are shown in Figures 11 to 17. The units are arbitary, one unit corresponding to one inch height on the strip chart recorder, when the ratemeter setting was 400 cps. at TC = 3 seconds. On Figures 11 to 17, the width of the bars is an estimate of the tolerance of the data. The cold peak intensity is included for reference. Since the figures are derived from a number of runs, two features must be made clear. An overlap of intensities over a range of temperature, for example, from 302°F to 307°F on Figure 11, indicates that for this range of temperature both intensities were obtainable on different runs. On occasion, a substantial increase in intensity could be obtained by refocusing the sample. Such instances are recorded on the figures with a broken line and the word "refocus". It will be noted that on Figure 16 the sample was refocused at the same time as it was

allowed to cool slightly, to recheck the coexistance of two intensity conditions for the 103 plane between 300°F and 350°F.

The extent to which peak intensity depended on very slight adjustments to the focus, render the intensity data somewhat unreliable. Only in Figure 11, for the 101 plane, was the increase in intensity so significant that there was no chance of the effect being due to focusing. Furthermore, the 101 peak showed other striking anomolies, as discussed later.

The changes in 2θ angle, Δ, are reported on Figures 18 to 24, together with the ranges of confidence. Possibilities of error were introduced by the following factors:

1) Random fluctuations of the pen gave rise to false peaks, slightly offset from the correct location. This source of error became progressively worse for the less intense peaks, but it was significant even for the strongest peaks. Reference to Figures 32b and 36 may be made to illustrate this source of error. Possible errors were up to 0.01° for the weakest peaks.

2) The 2θ magnetic drive mechanism was triggered manually when the pen on the strip chart recorder crossed a heavy line, giving rise to the possibility of small human errors in the location of the origin for each scan. The

strip chart and the 2θ drive were synchronized, so that angles were read in terms of distance along the strip chart. Thus errors in locating the origin were transmitted across the whole of the individual scan, but no further error was introduced during the scan. Maximum error from this cause was about 0.005°.

3) Some error was always inherent in estimating the actual peak, which was seldom sharp. Maximum error from this cause was 0.002°.

4) Since peak shift was measured by subtracting the value of 2θ for the cold peak from the value for the hot peak, errors 1, 2 and 3 in the cold peak would produce further error in the hot peak. By averaging a number of cold runs, this source of error was reduced, but a total possible error of 0.01° was still possible.

The maximum error in Δ was therefore 0.027°. Uncertainty in B, the peak width at half intensity was caused by the variations in recorded peak intensity. A further source of error was the need to estimate the intensity owing to α_1 radiation, by subtracting out the contribution of the α_2 radiation (20).

On Figure 10, a double peak is shown, with the α_1 and α_2 contributions. We assume that the contribution of α_2 intensity at the α_1 peak is negligible, and vica versa. Then, since each peak is ideally symmetrical, we

have that:

$$PB = PA + PC = PA + (QD/2) \qquad (17)$$

Half height intensities owing to α_1 radiation are presented on Figures 25 to 31. The average value of the ratio of α_1 radiation width to total double peak width is given for each reflection on Table 3.

On Figures 32 to 38 representative peaks for each diffraction are shown. On Figure 39 a number of interesting peaks diffracted by the 101 plane are shown. These peaks are interpreted in the discussion of results as indicating an ordering of lattice vacancies normal to the 101 plane.

Figure 24 shows the peak shift for radiation diffracted by the 211 plane. The more scattered data points were taken from earlier runs of the first type, that is, where all seven peaks were scanned at each temperature. The later runs scanning the one peak only were in disagreement. This disagreement is attributed to the fact that the incident and receiving soller collimators started hitting the furnace at about 67°, 2θ. Though the error thus introduced was insignificant in the earlier runs, it had and accumulating effect in the later runs where the one peak was being repeatedly scanned.

Reflection Plane	2θ	Temperature Range	$\frac{\alpha_1 \text{ Half height width}}{\text{Total half height width}}$
101	32.96°	290 - 308°F	0.328
		302 - 308°F	0.661
		308 - 311°F	0.559
002	36.32°	290 - 311°F	0.620
110	39.17°	290 - 311°F	0.510
112	54.47°	290 - 311°F	0.480
200	56.60°	290 - 311°F	0.460
103	63.20°	290 - 311°F	0.520
211	67.02°	290 - 311°F	0.590

Table 3 THE RATIO OF HALF INTENSITY PEAK WIDTH OWING TO α_1 RADIATION, AND OWING TO THE COMBINED α_1 AND α_2 RADIATION.

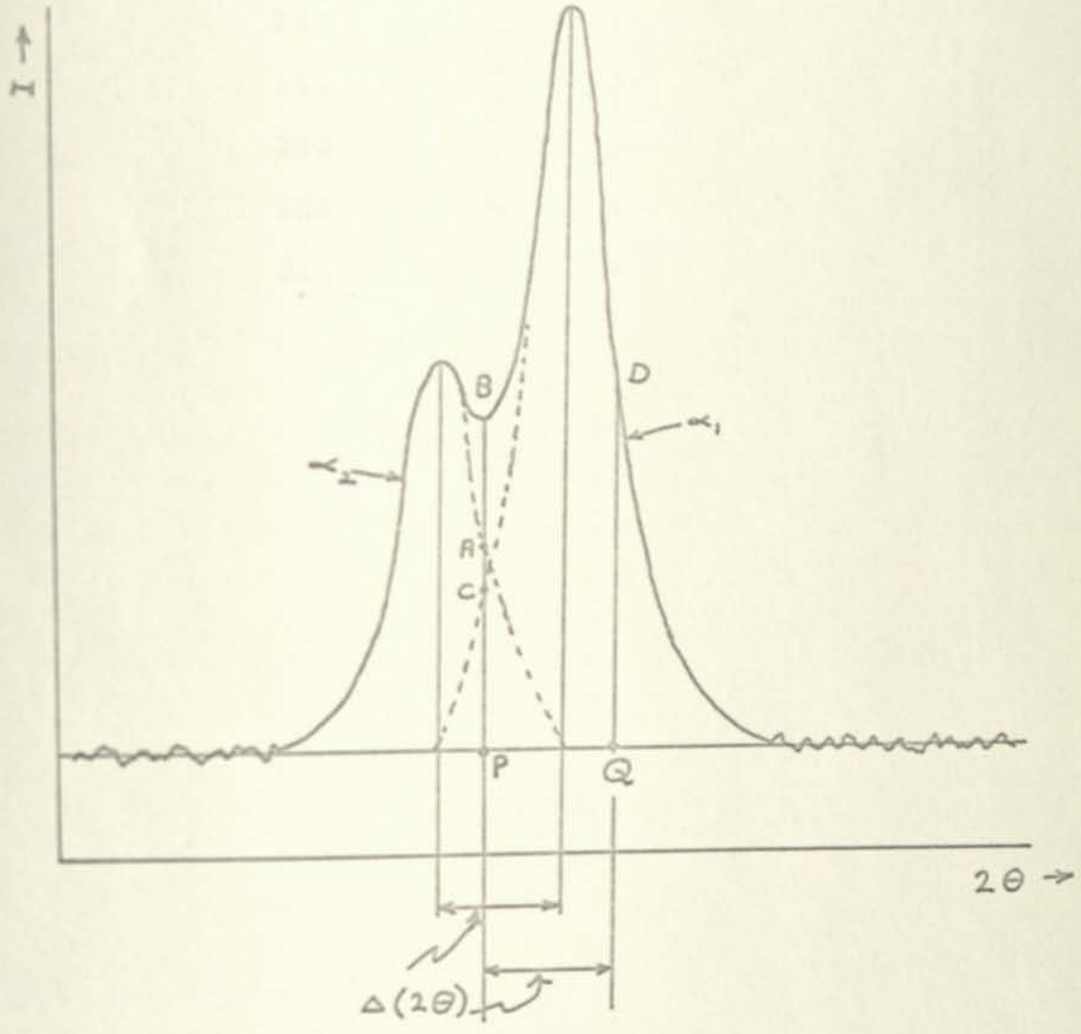

Figure 10 THE CALCULATION OF HALF PEAK INTENSITY WIDTH OWING TO α_1 RADIATION ONLY

The following number of runs were used on Figures 11 to 31 for each of the following planes of reflection:

Plane	Runs
101	4
002	3
110	3
112	3
200	3
103	4
211	4

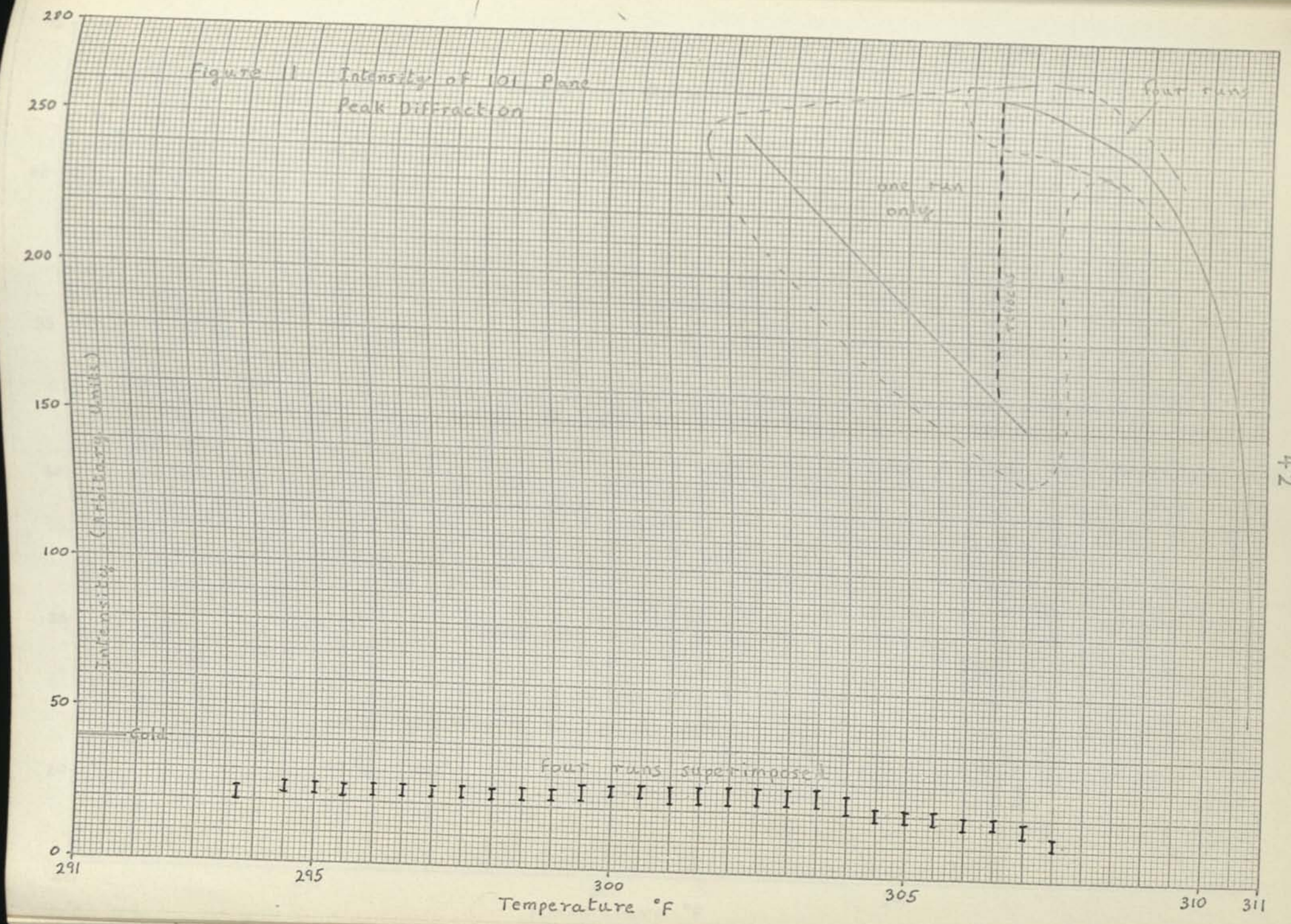
Figure 11 Intensity of 101 Plane Peak Diffraction
four runs
one run only
Cold
four runs superimposed
Intensity (Arbitrary Units)
Temperature °F
250
200
150
100
50
0
291
295
300
305
310
311

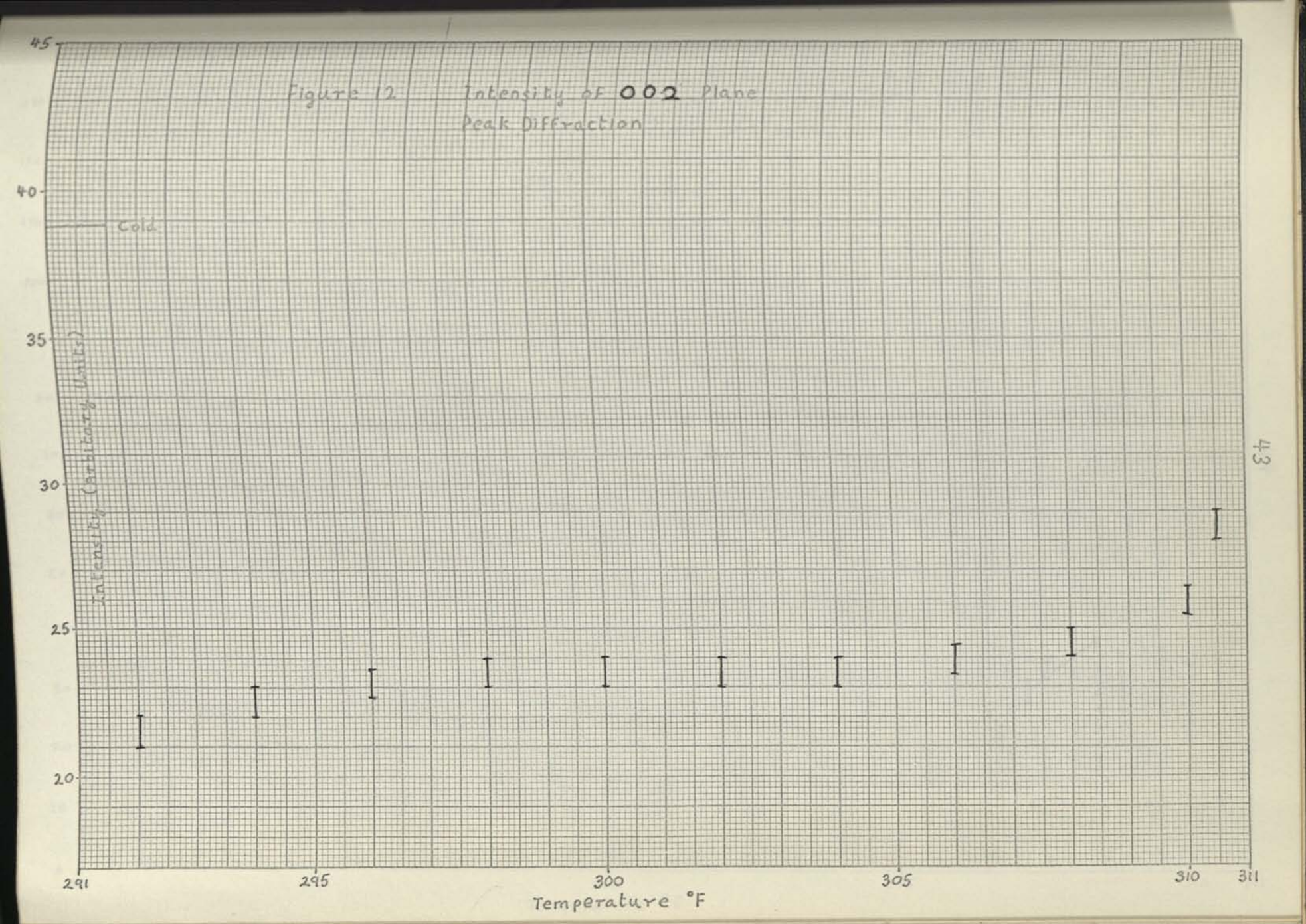
Figure 12 Intensity of 002 Plane
Peak Diffraction
Cold
Intensity (Arbitary Units)
45
40
35
30
25
20
291
295
300
305
310
311
Temperature °F

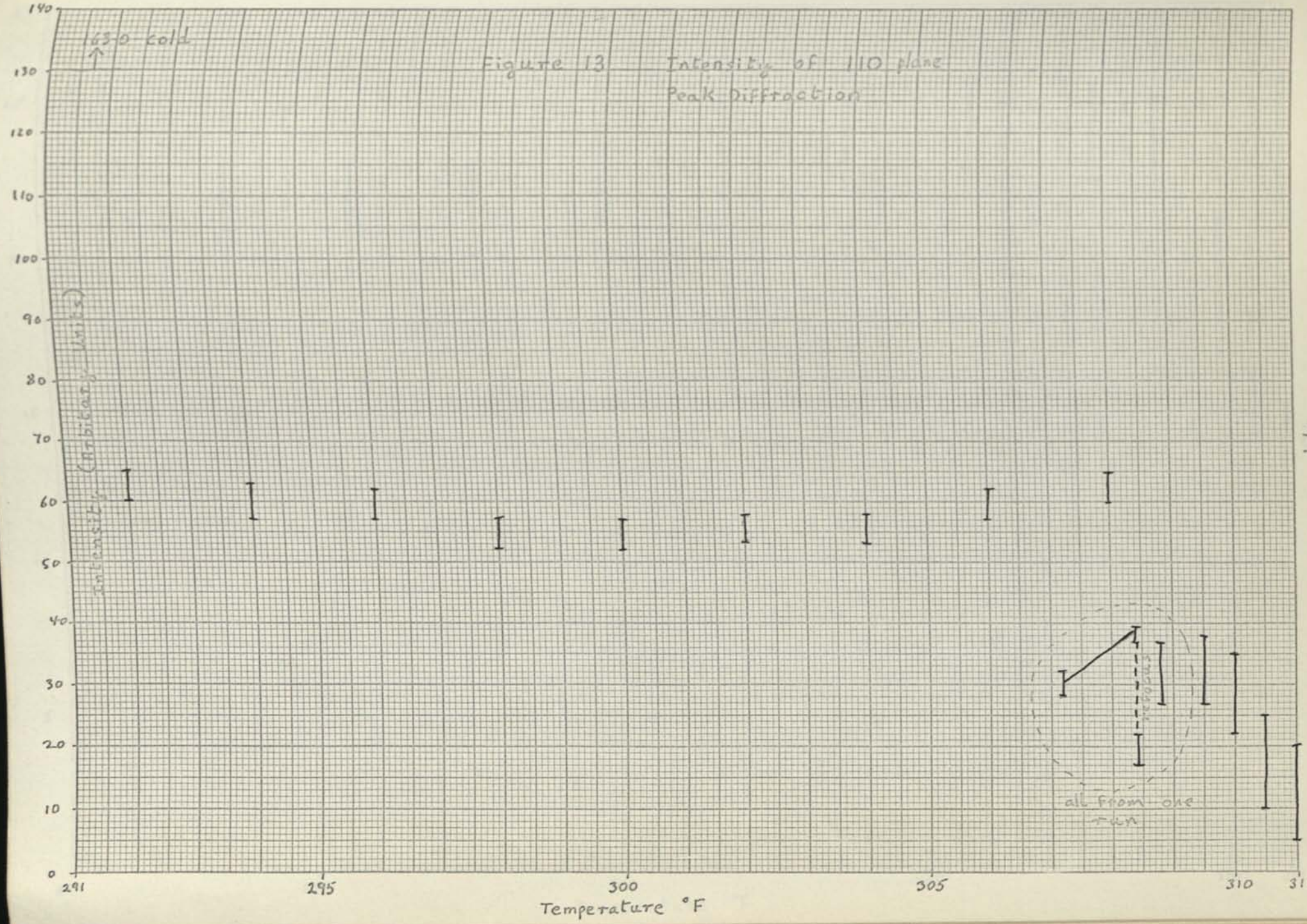

Figure 13 Intensity of 110 plane Peak Diffraction

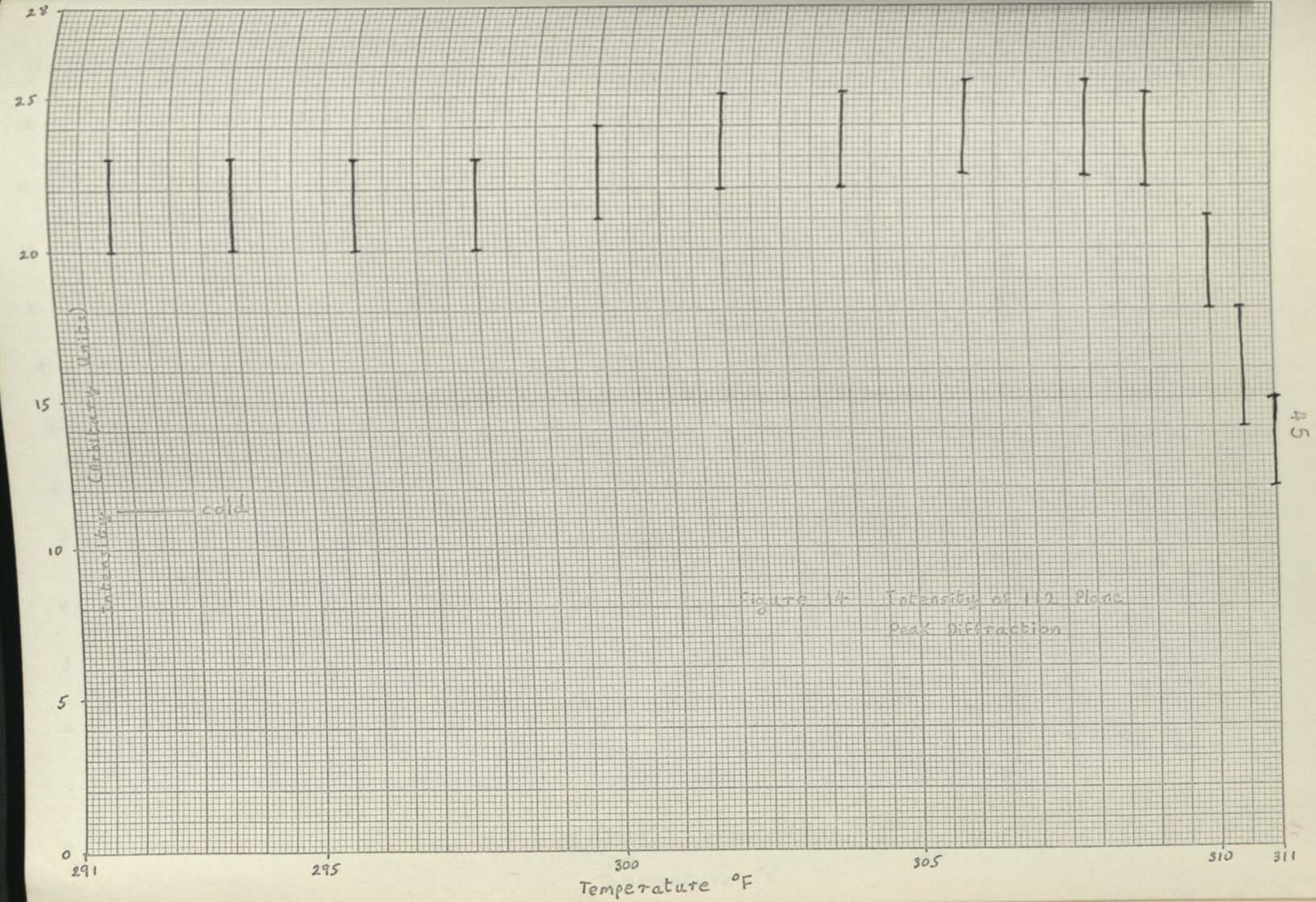

Figure 14 Intensity of 112 plane peak diffraction

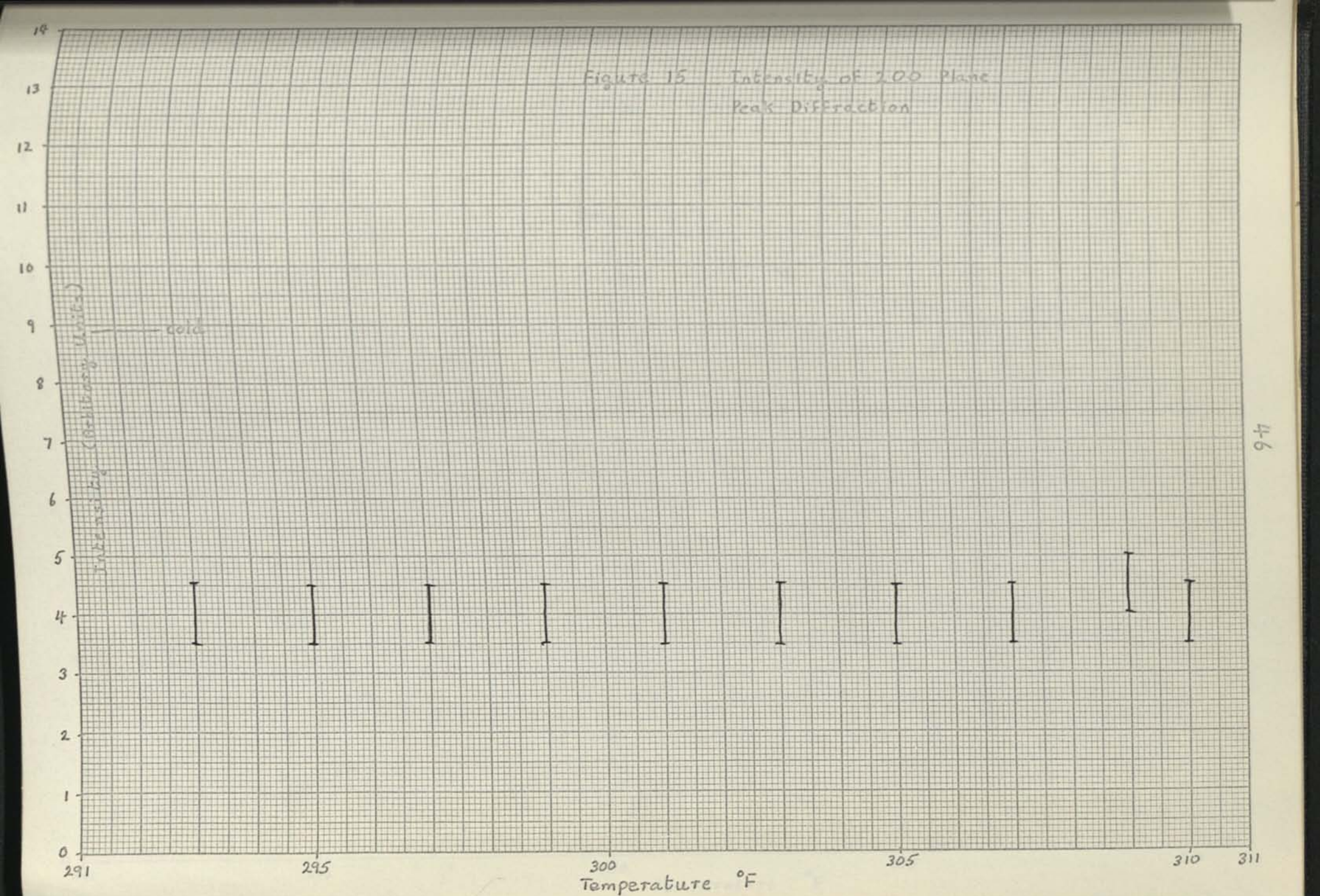
Figure 15 Intensity of 200 Plane Peak Diffraction
Intensity (Arbitrary Units)
cold
0
1
2
3
4
5
6
7
8
9
10
11
12
13
14
291
295
300
305
310
311
Temperature °F

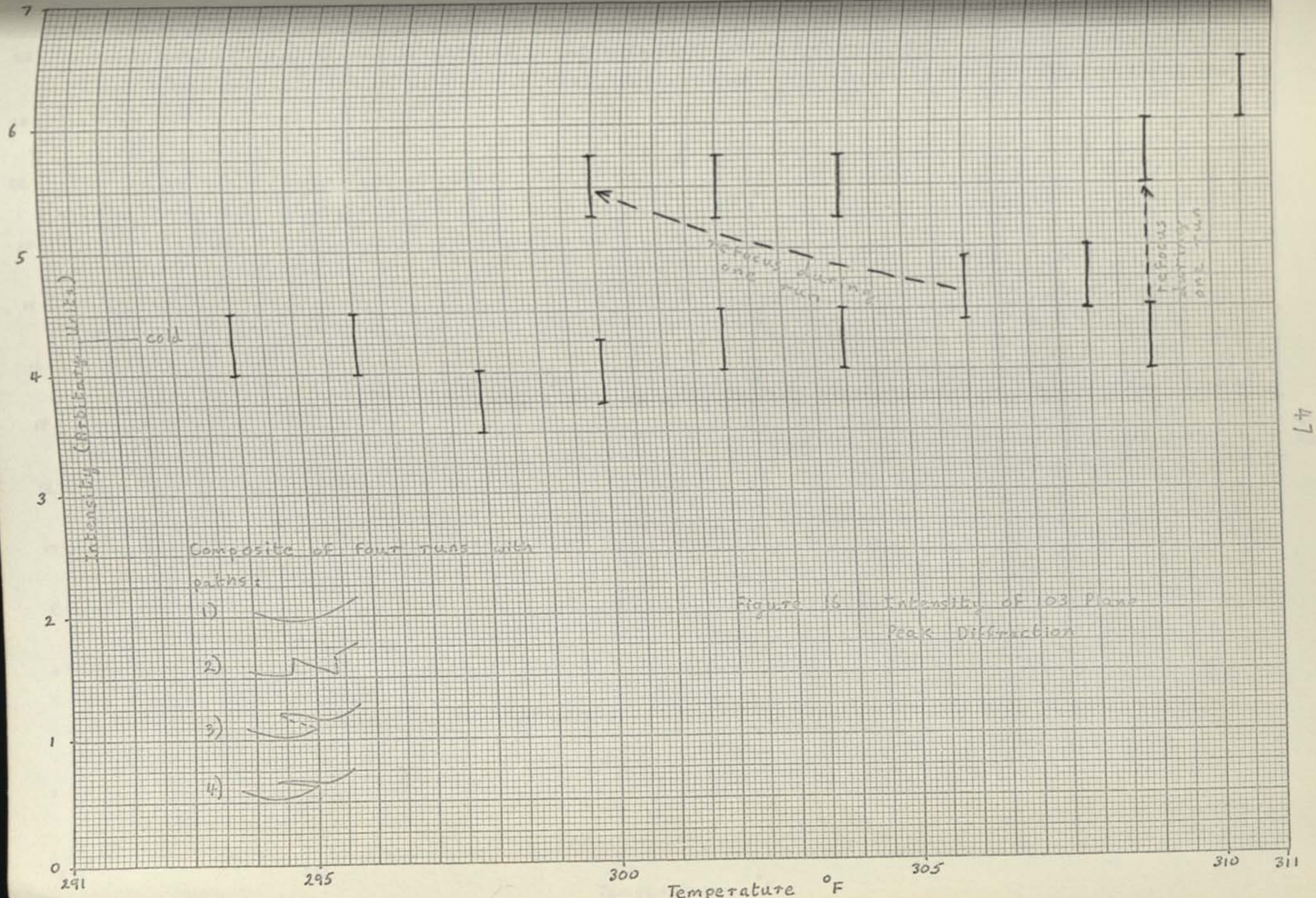

Figure 16 Intensity of 03 Plane Peak Diffraction

47

Figure 17 Intensity of 211 Plane Peak Diffraction

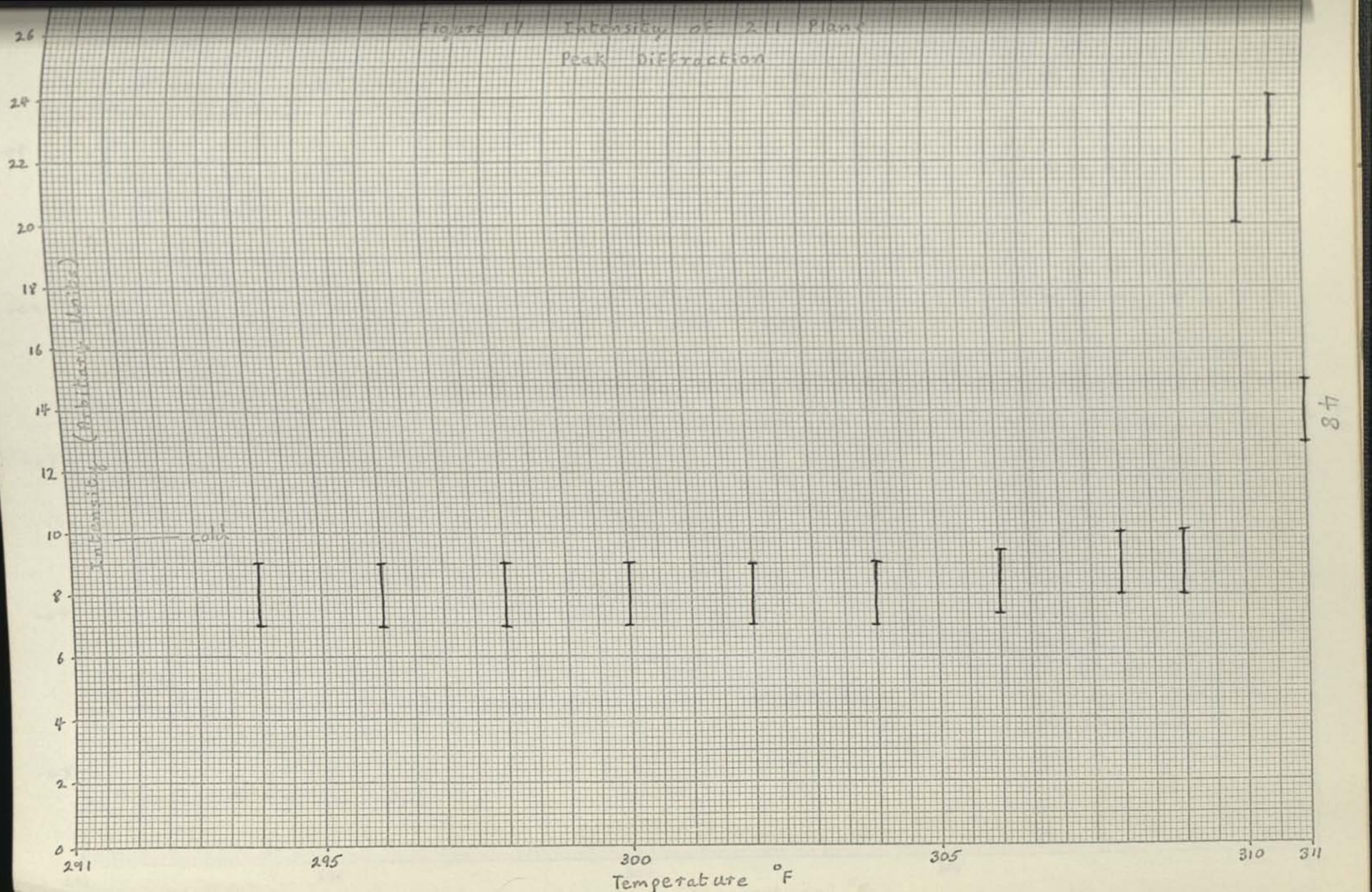

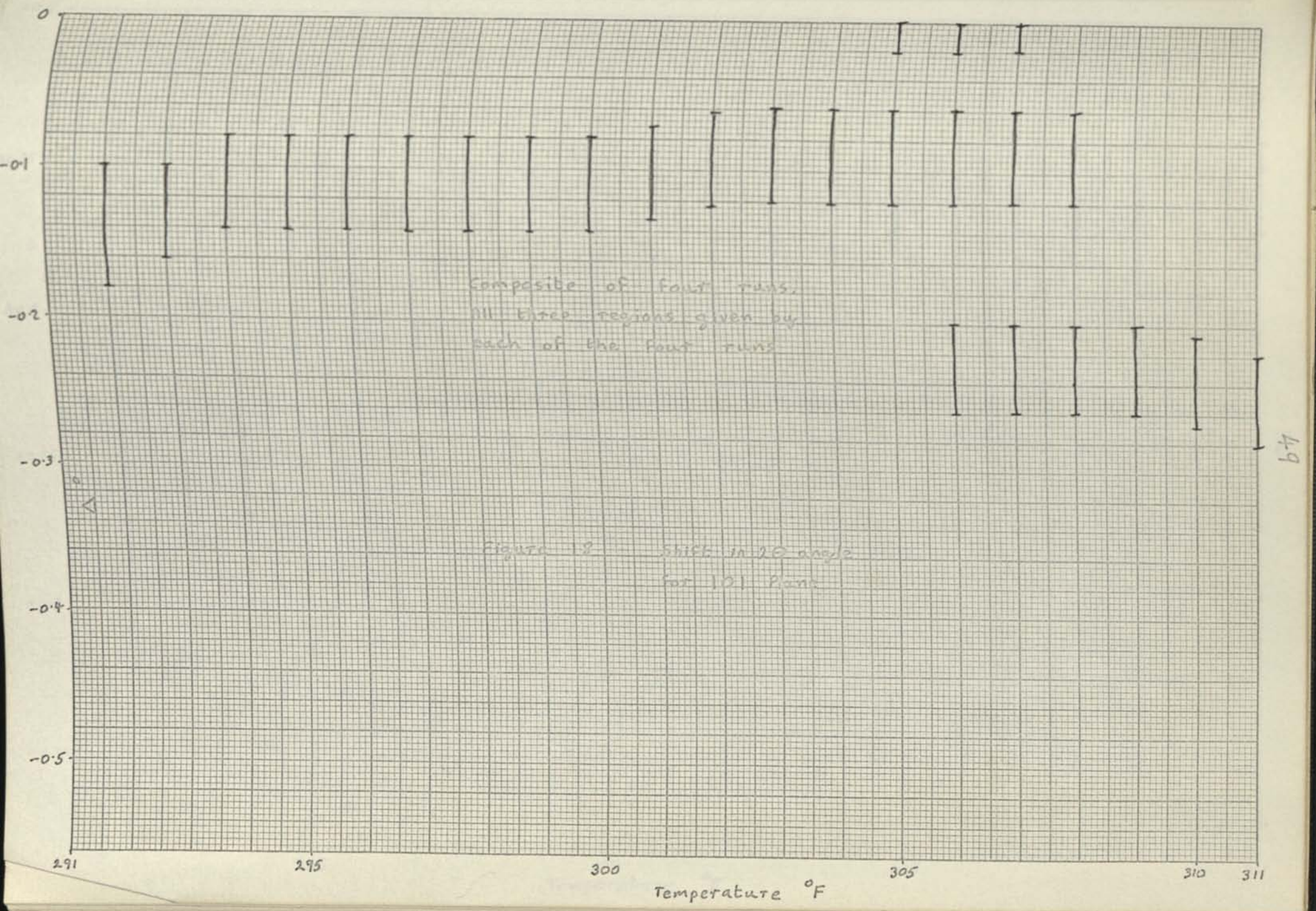

Composite of four runs, all three regions given by each of the four runs

Figure 19 Shift in 2θ angle for 101 Plane

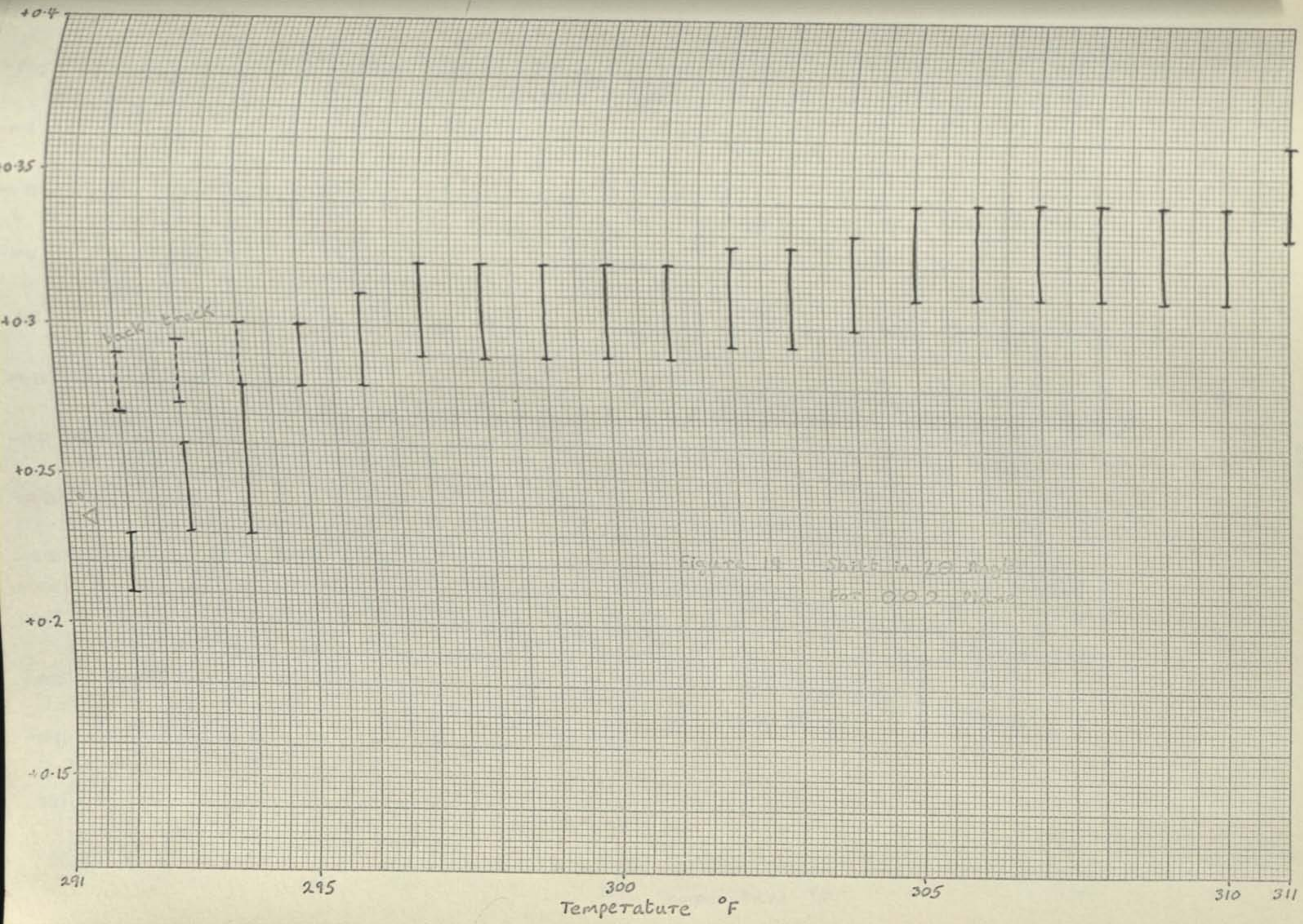

Figure 14 Shift in 2θ Angle for 002 Plane

Figure 20 Shift in 2θ Angle
For 110 Plane

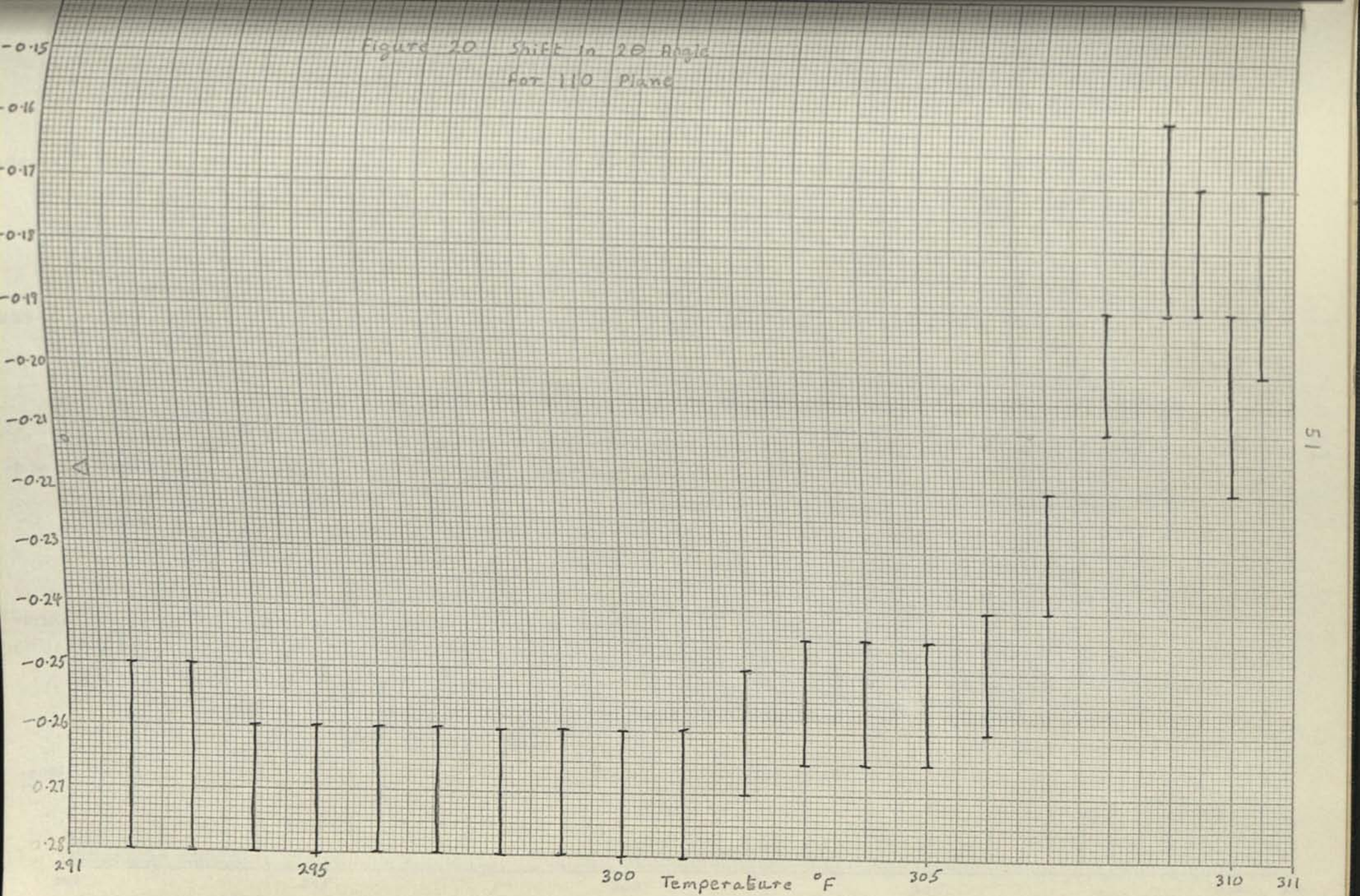

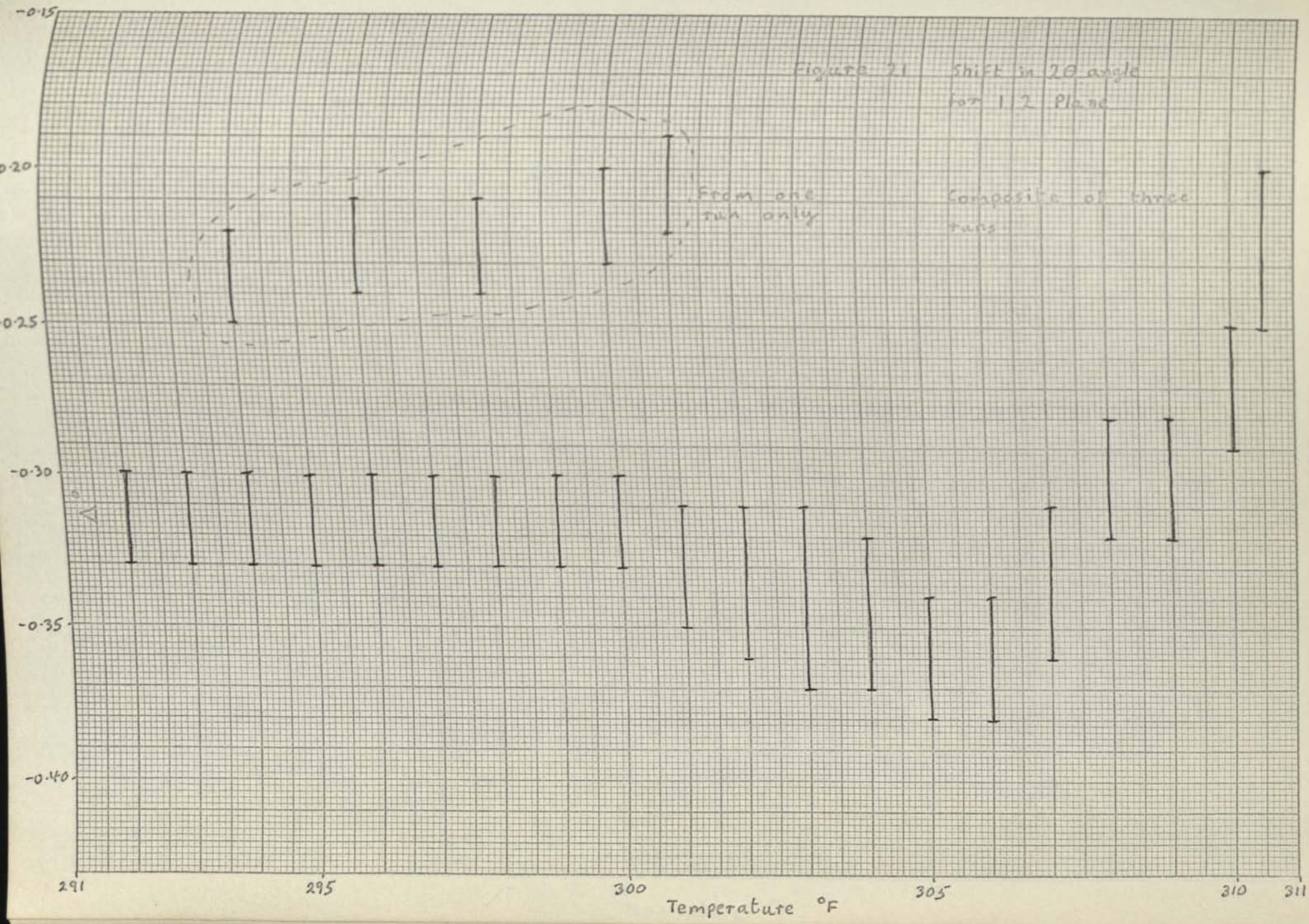

Figure 21 Shift in 2θ angle for 1 2 Plane

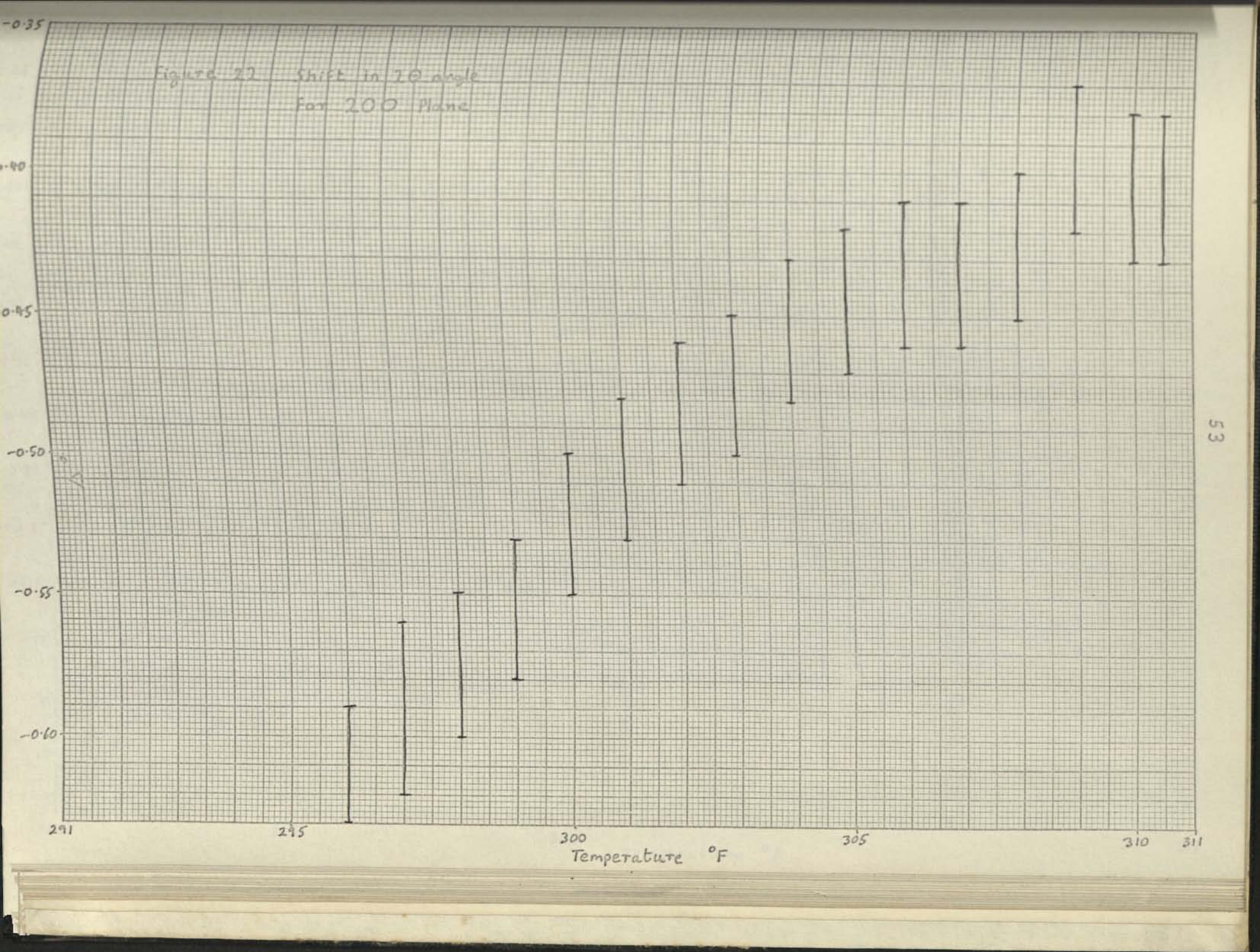

Figure 22 Shift in 2θ angle
For 200 Plane

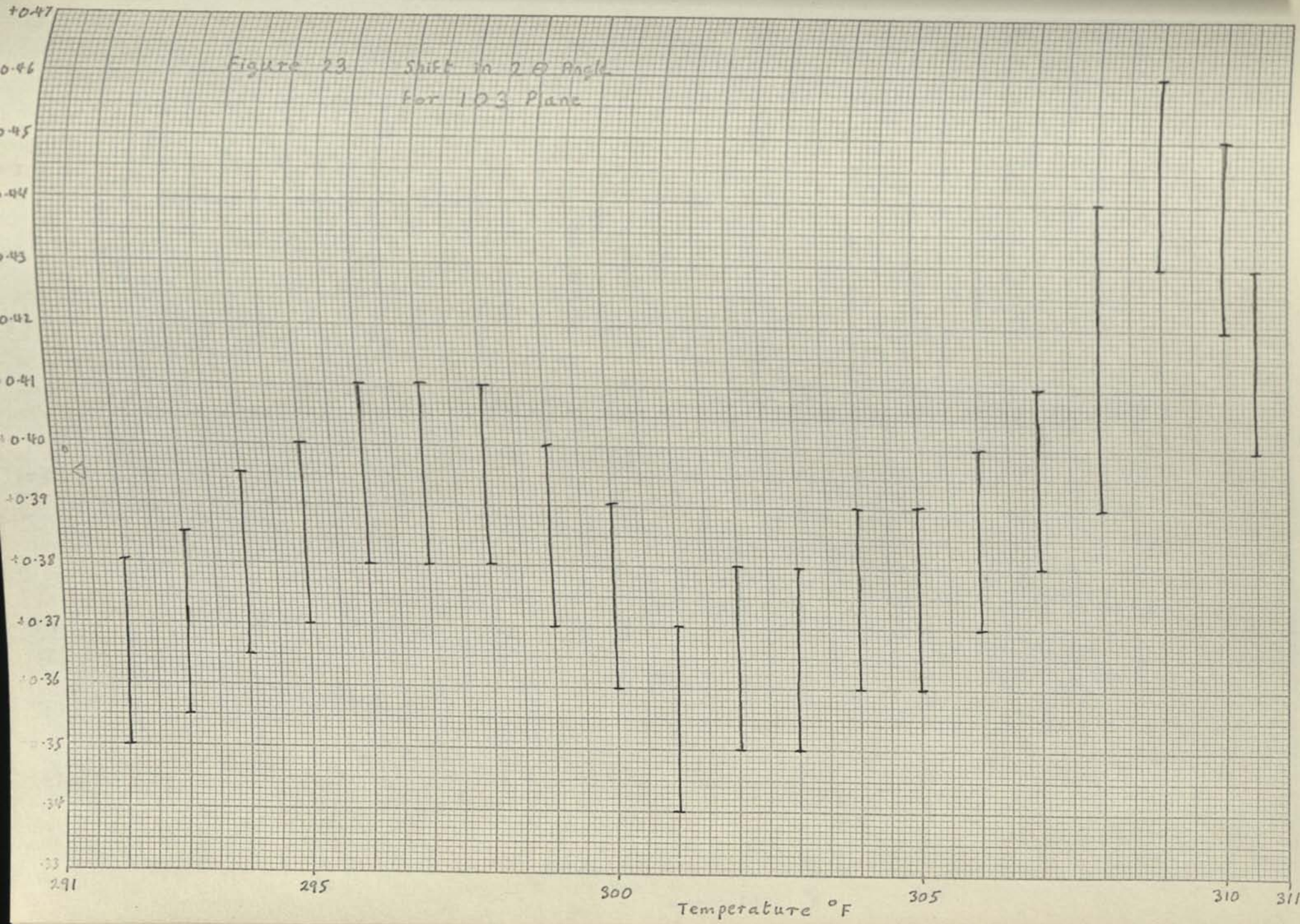
Figure 23 Shift in 2θ Angle for 103 Plane
+0.47
0.46
0.45
0.44
0.43
0.42
0.41
0.40
0.39
0.38
0.37
0.36
0.35
0.34
0.33
291
295
300
305
310
311
Temperature °F

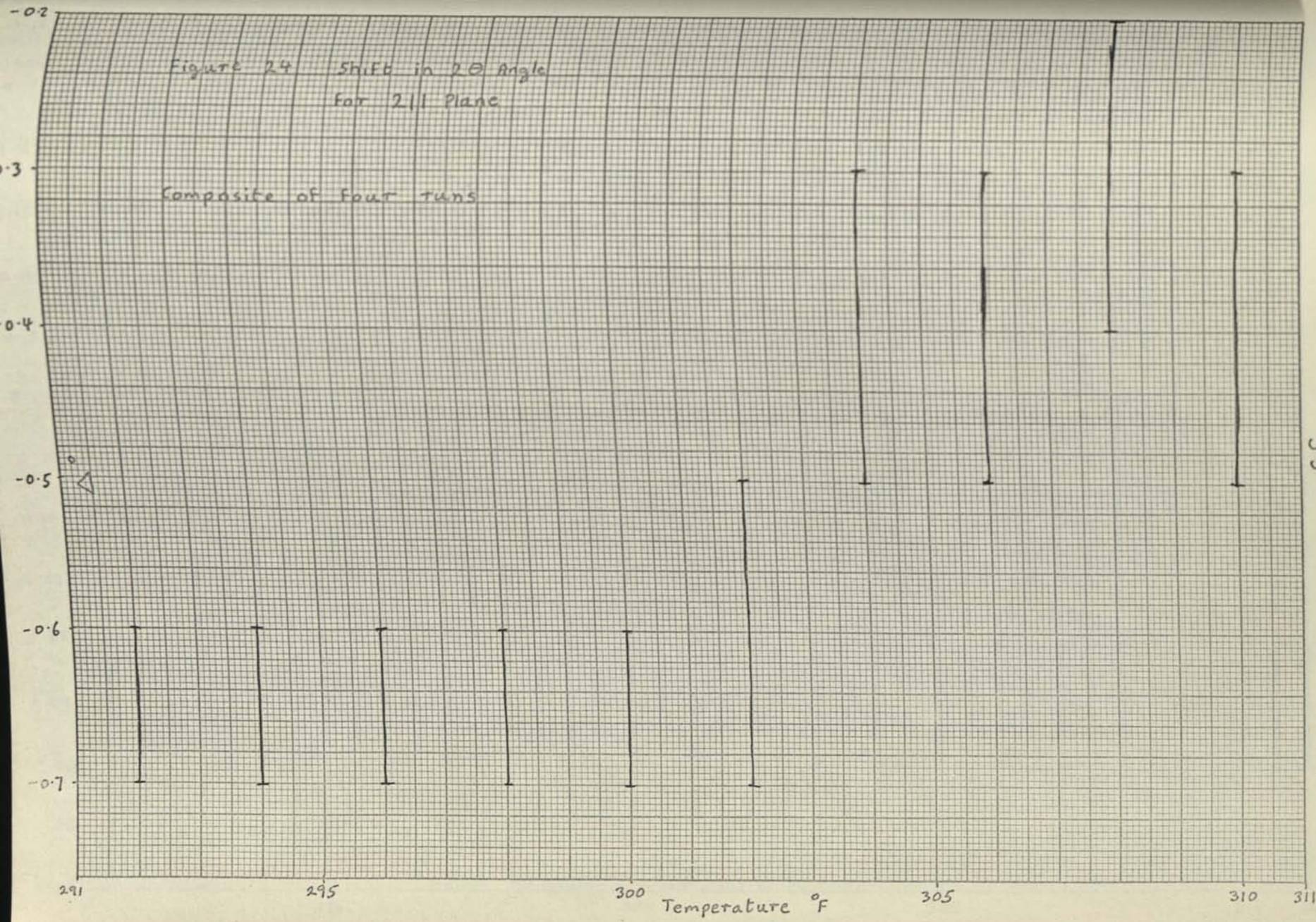

Figure 24 Shift in 2θ Angle
For 211 Plane

Composite of Four Runs

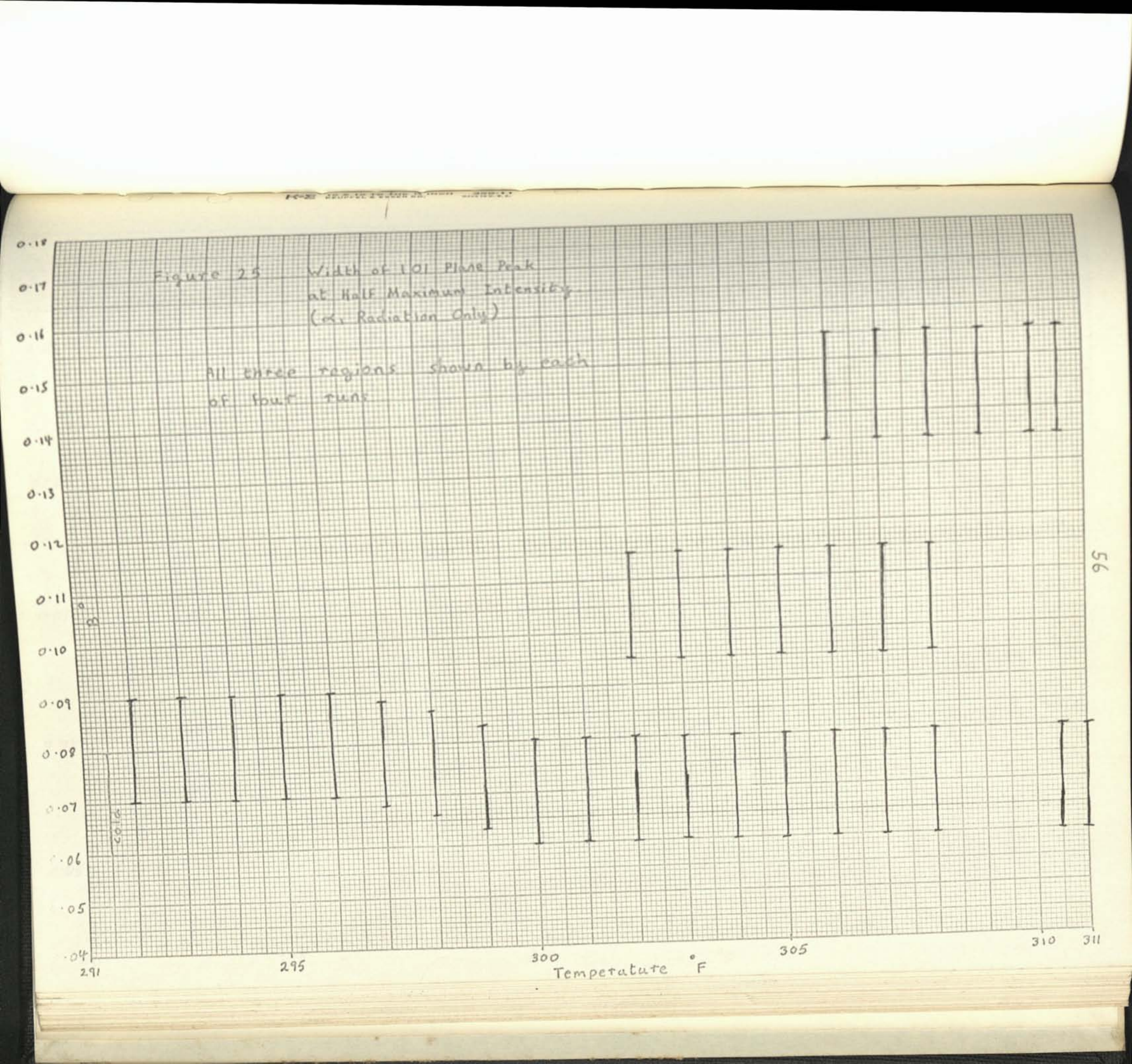
Figure 25 Width of 101 Plane Peak at Half Maximum Intensity (Cu Radiation Only)
All three regions shown by each of four runs
0·18
0·17
0·16
0·15
0·14
0·13
0·12
0·11
0·10
0·09
0·08
0·07
0·06
·05
·04
291
295
300
305
310
311
Temperature °F
95

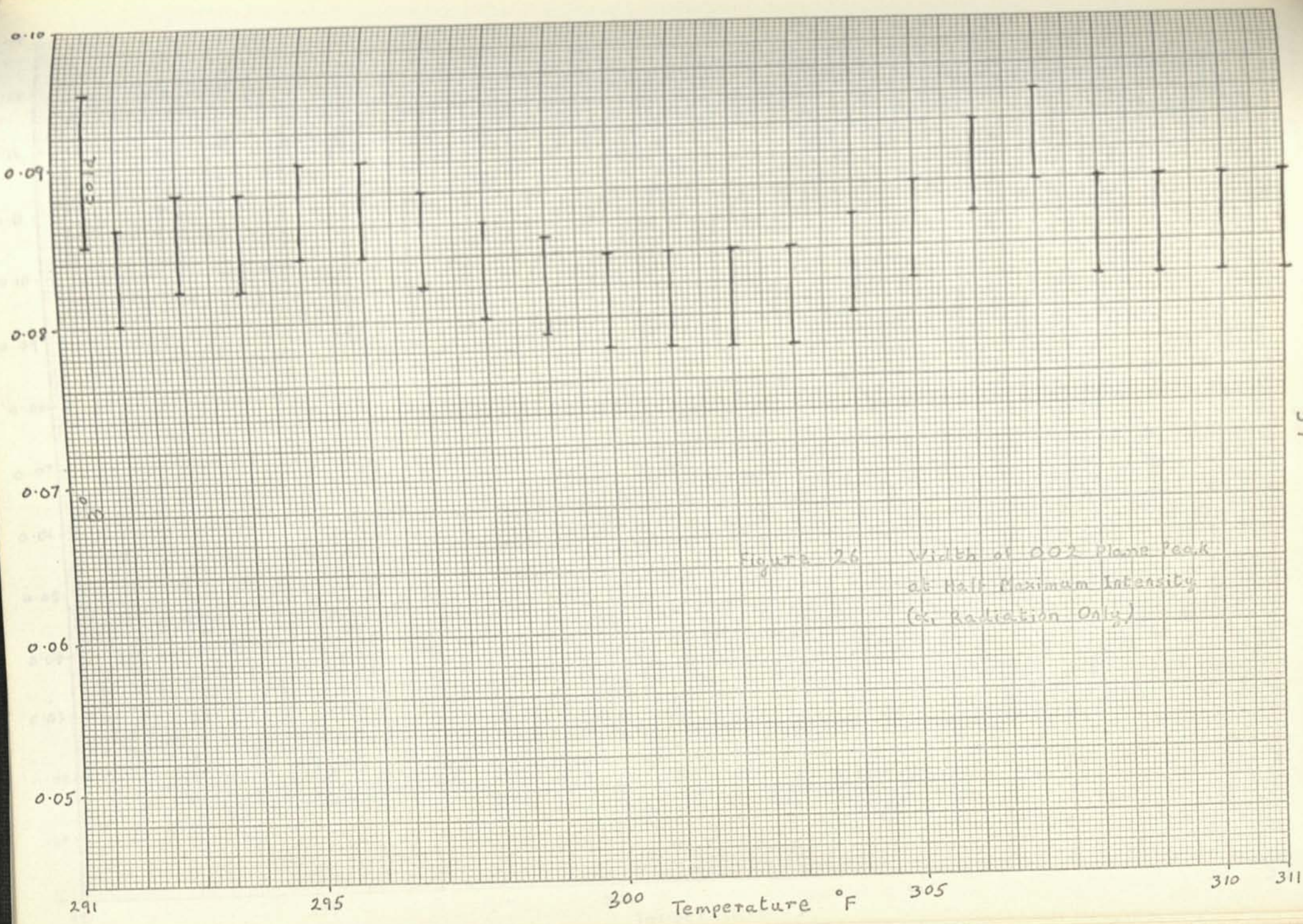

Figure 26 Width of 002 Plane Peak at Half Maximum Intensity (Cu Radiation Only)

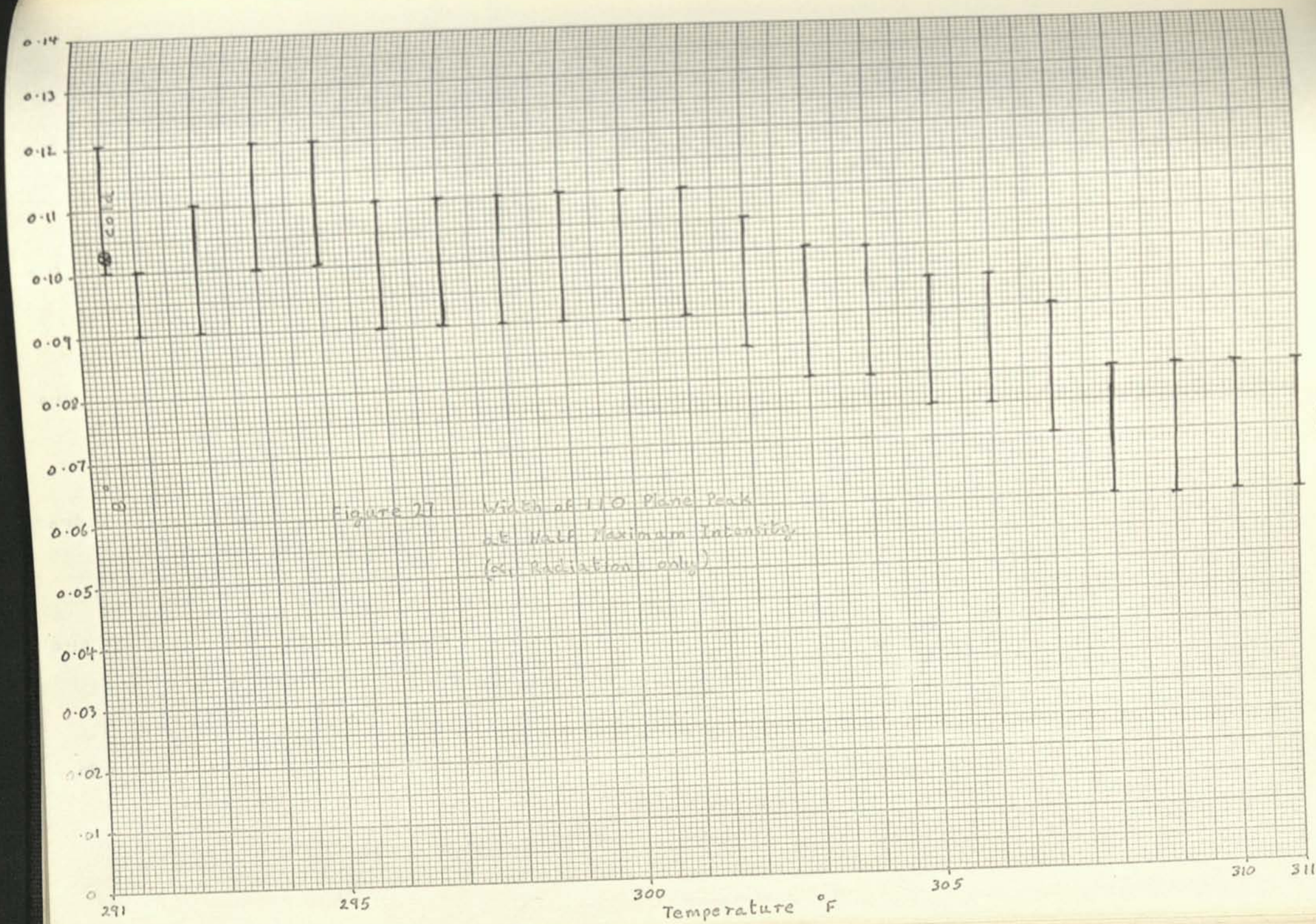

Figure 27 Width at 1/2 Plane Peak at Half Maximum Intensity (α₁ Radiation only)

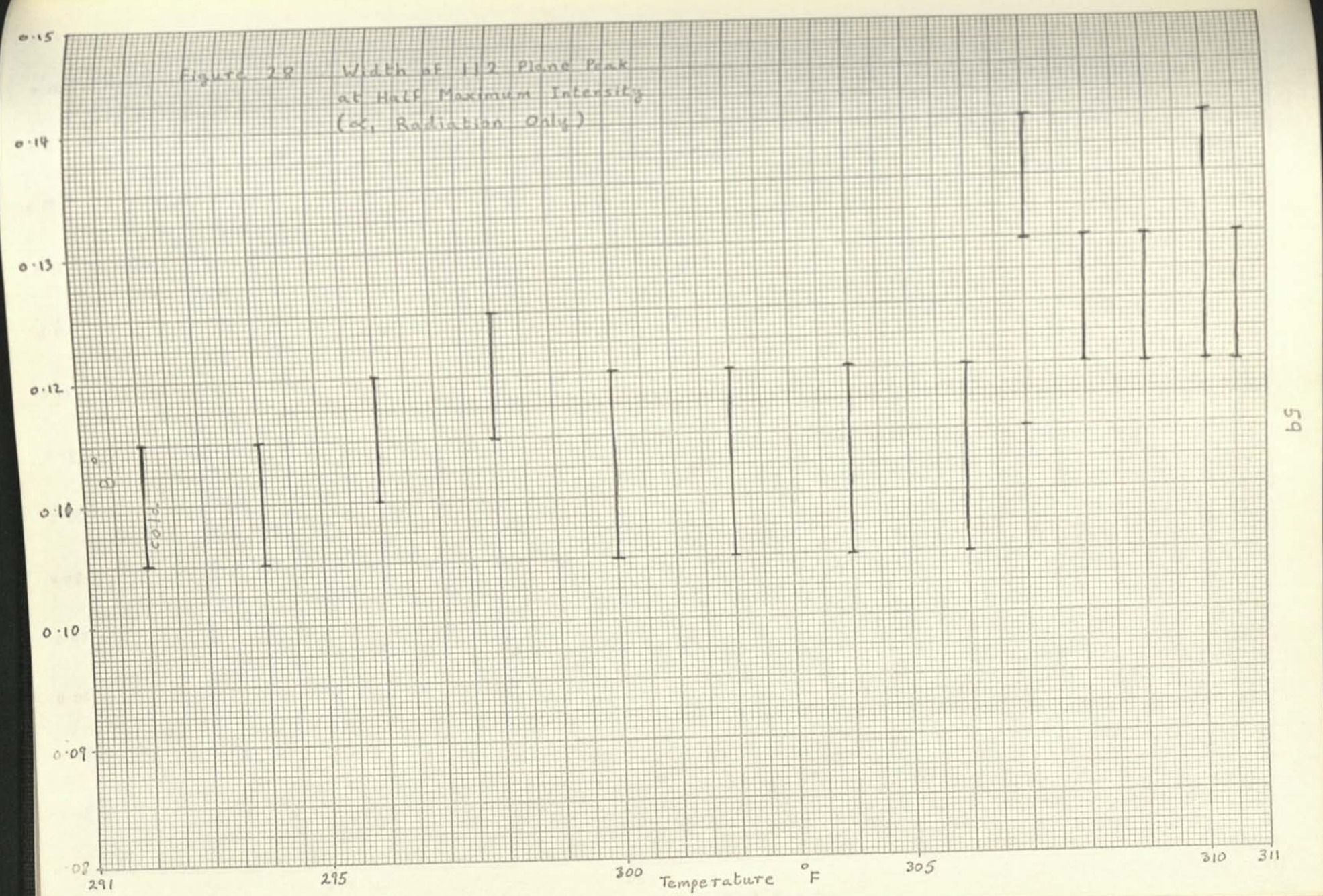
Figure 28 Width of 112 Plane Peak at Half Maximum Intensity (α1 Radiation Only)
0.15
0.14
0.13
0.12
0.11
0.10
0.09
0.08
291
295
300
305
310
311
Temperature °F
65

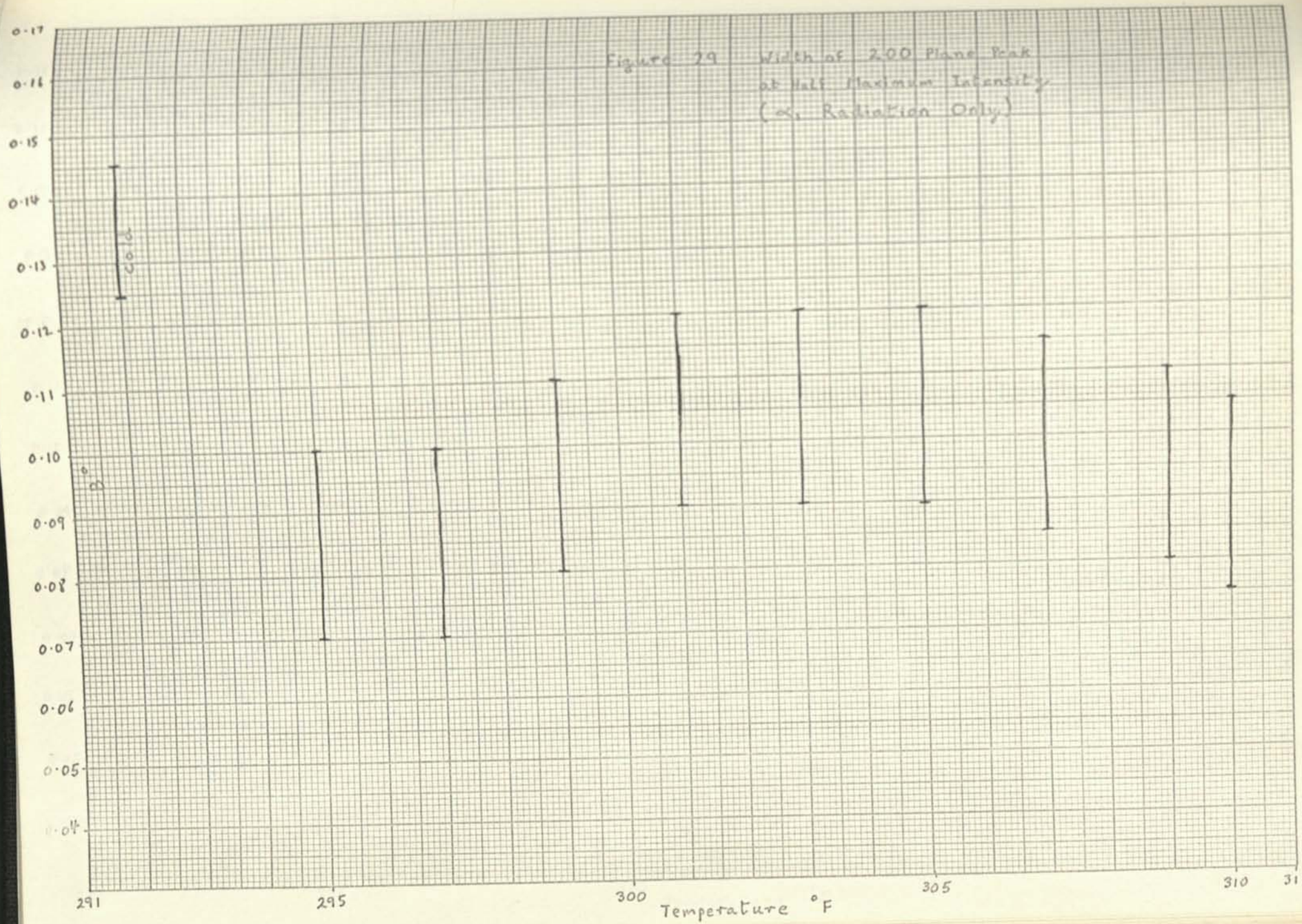

Figure 29 Width of 200 Plane Peak at Half Maximum Intensity (α_1 Radiation Only)

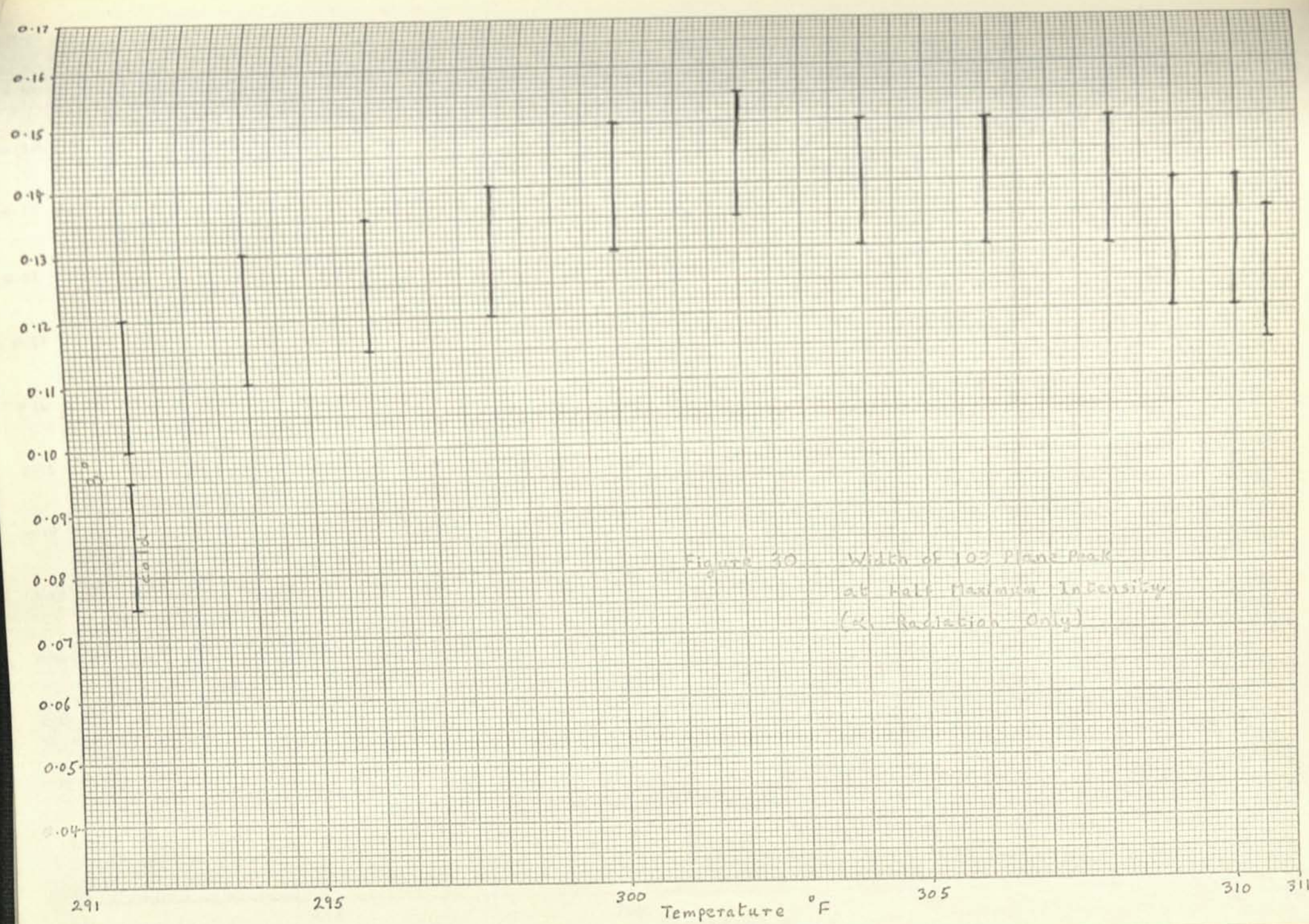

Figure 30. Width of 10-3 Plane Peak at Half Maximum Intensity (Cr Radiation Only)

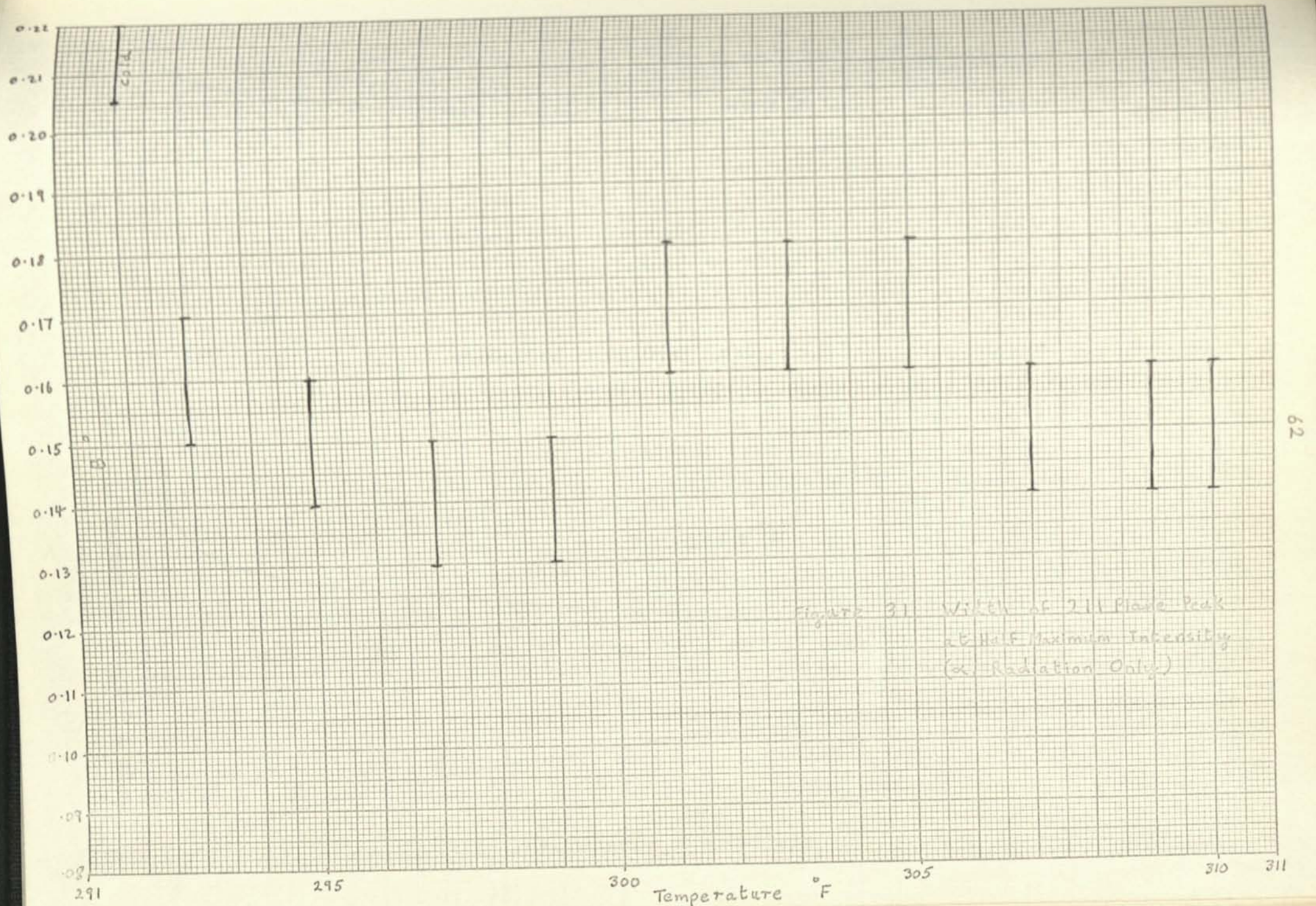

Figure 31 Width of 311 Plane Peak at Half Maximum Intensity (α Radiation Only)

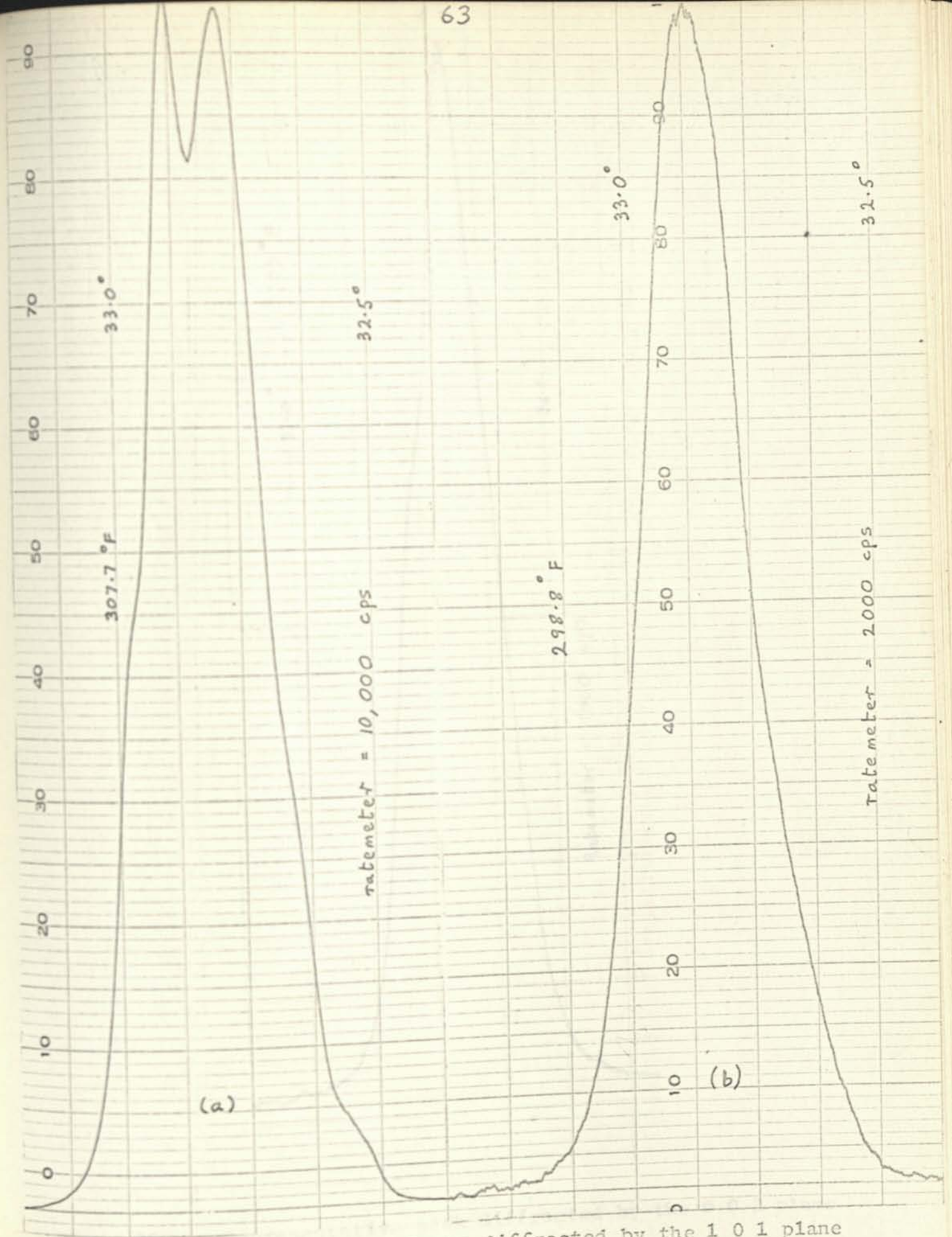

Figure 32 Representative Peaks diffracted by the 1 0 1 plane

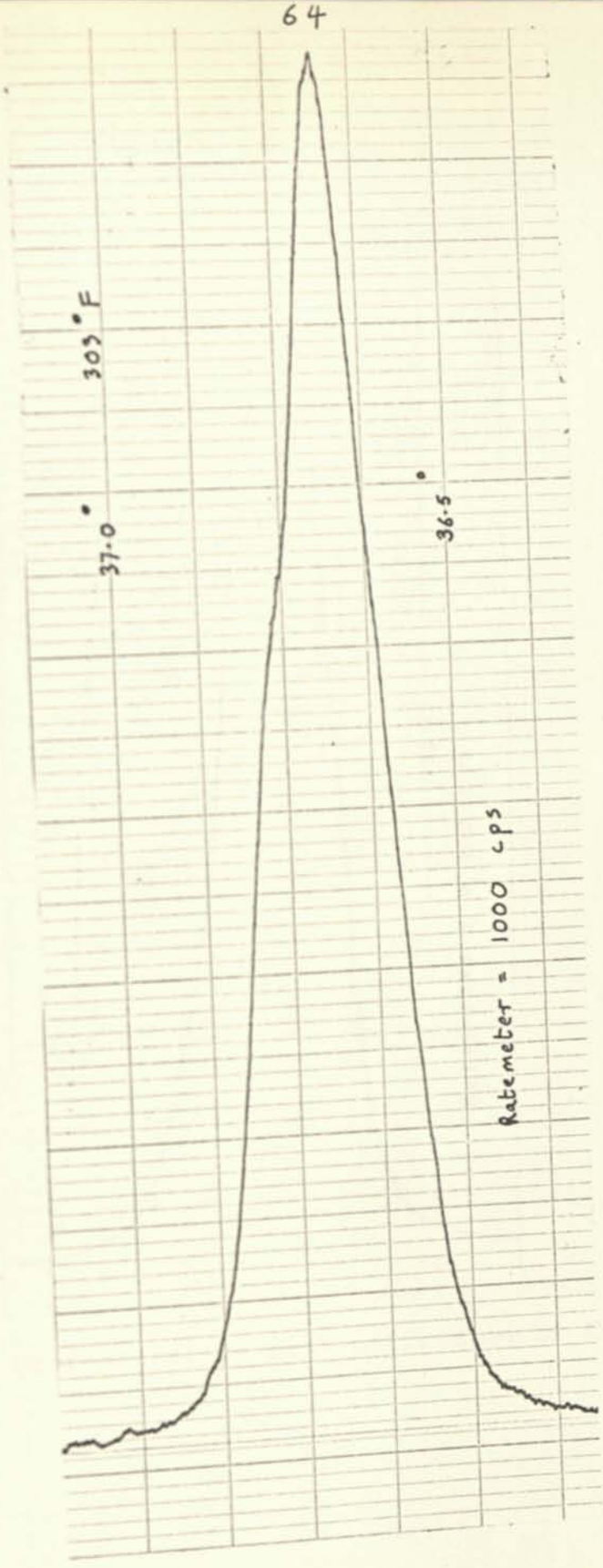

Figure 33 Representative peak diffracted by the 0 0 2 plane

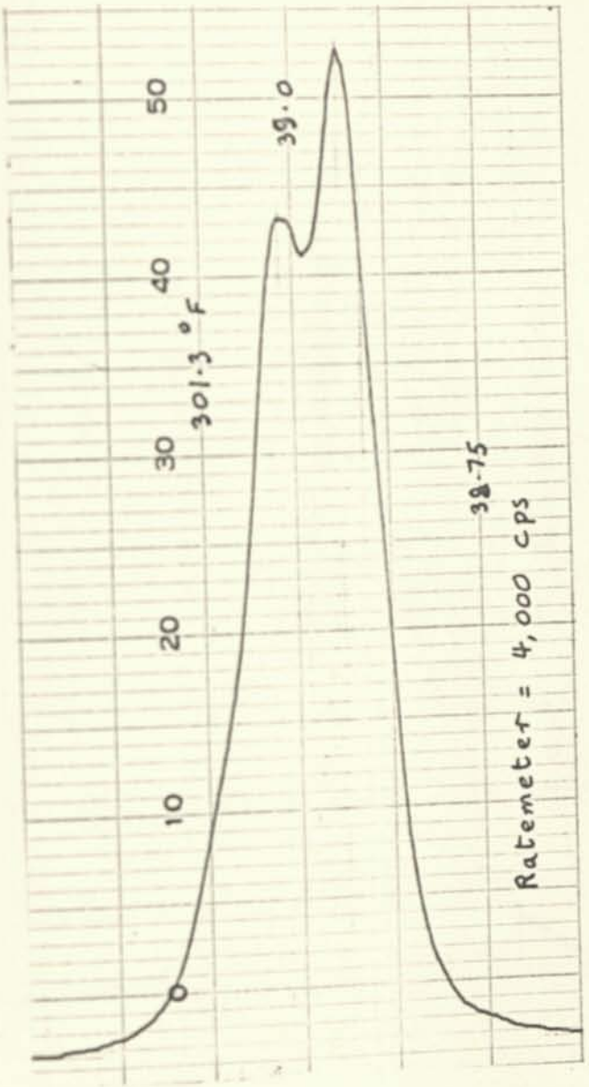

Figure 34 Representative peak diffracted by the 1 1 0 plane

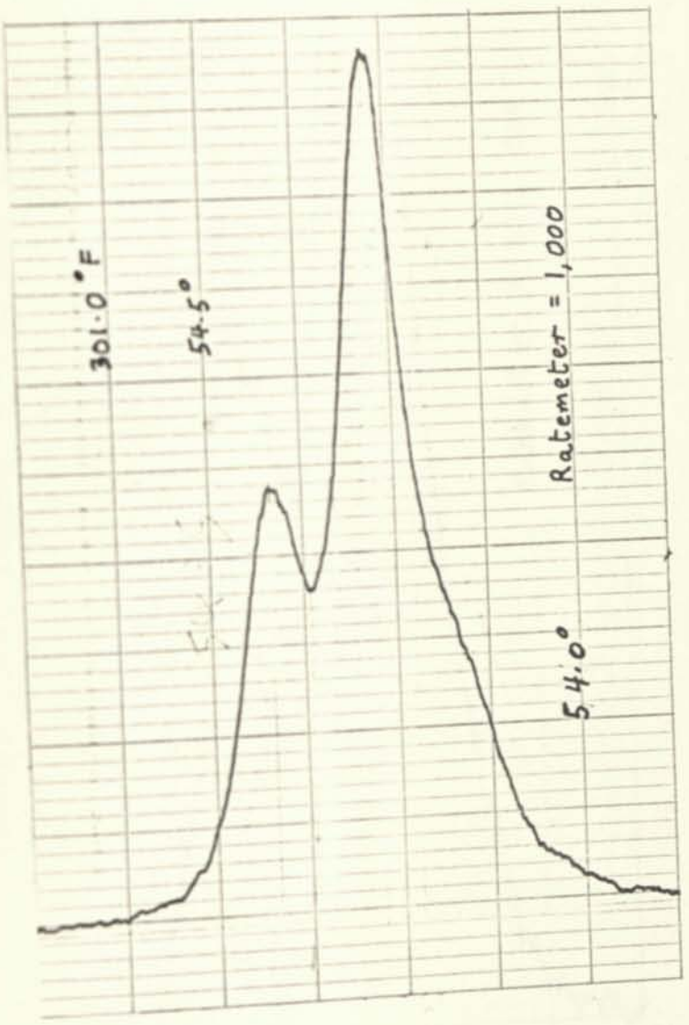

Figure 35 Representative peak diffracted by the 1 1 2 plane

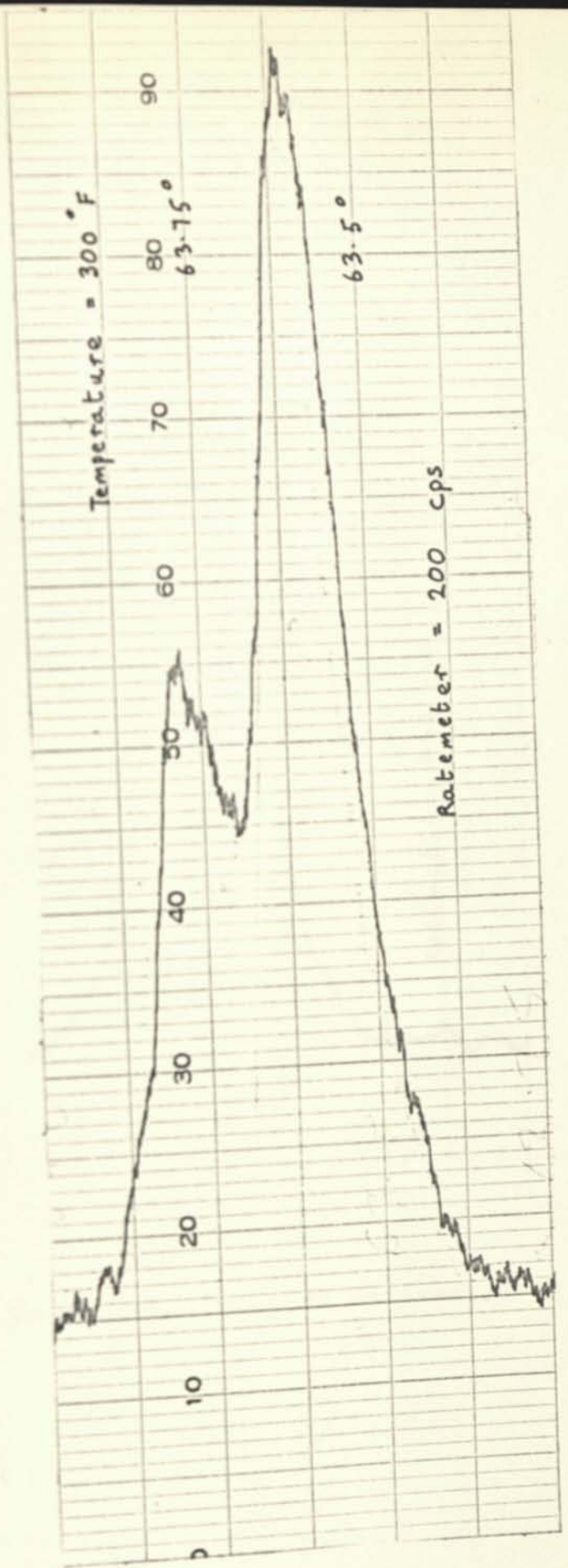

Figure 37 Representative peak diffracted by the 1 0 3 plane

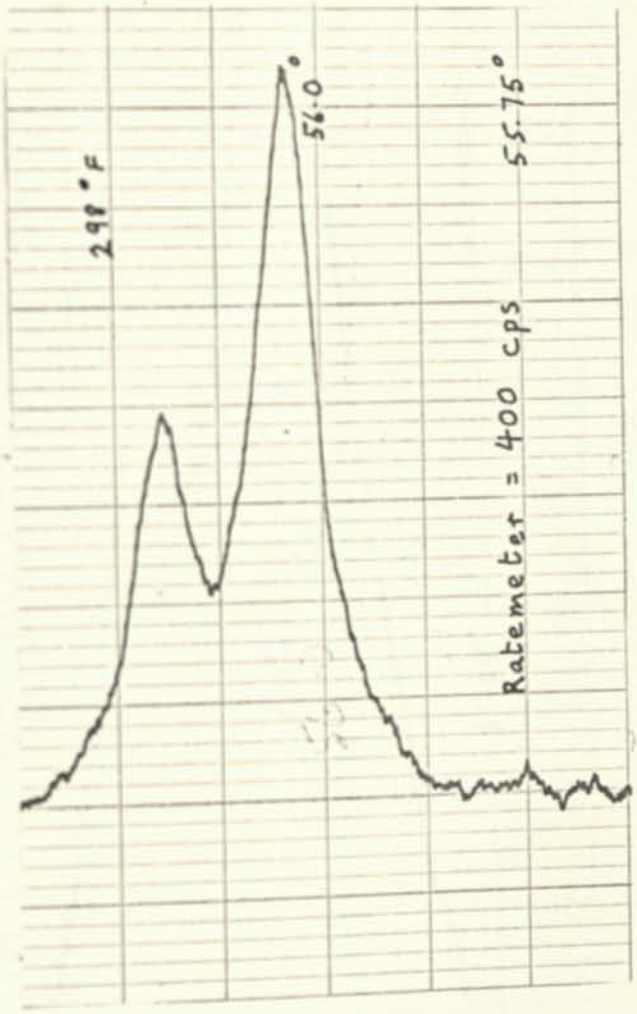

Figure 36 Representative peak diffracted by the 2 0 0 plane

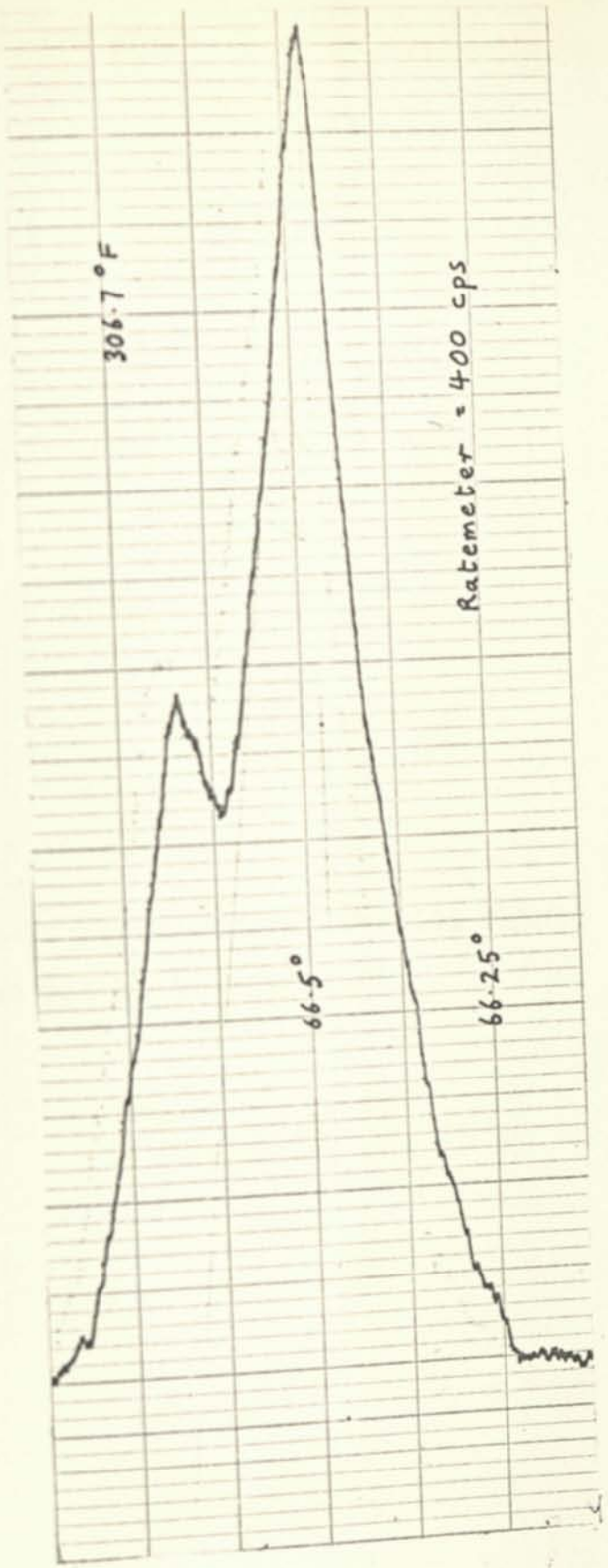

Figure 38 Representative peak diffracted by the 2 1 1 plane

Figure 39 a to m

PEAKS DIFFRACTED BY THE 101 PLANE, SHOWING EVIDENCE OF ORDERING NORMAL TO THE PLANE.

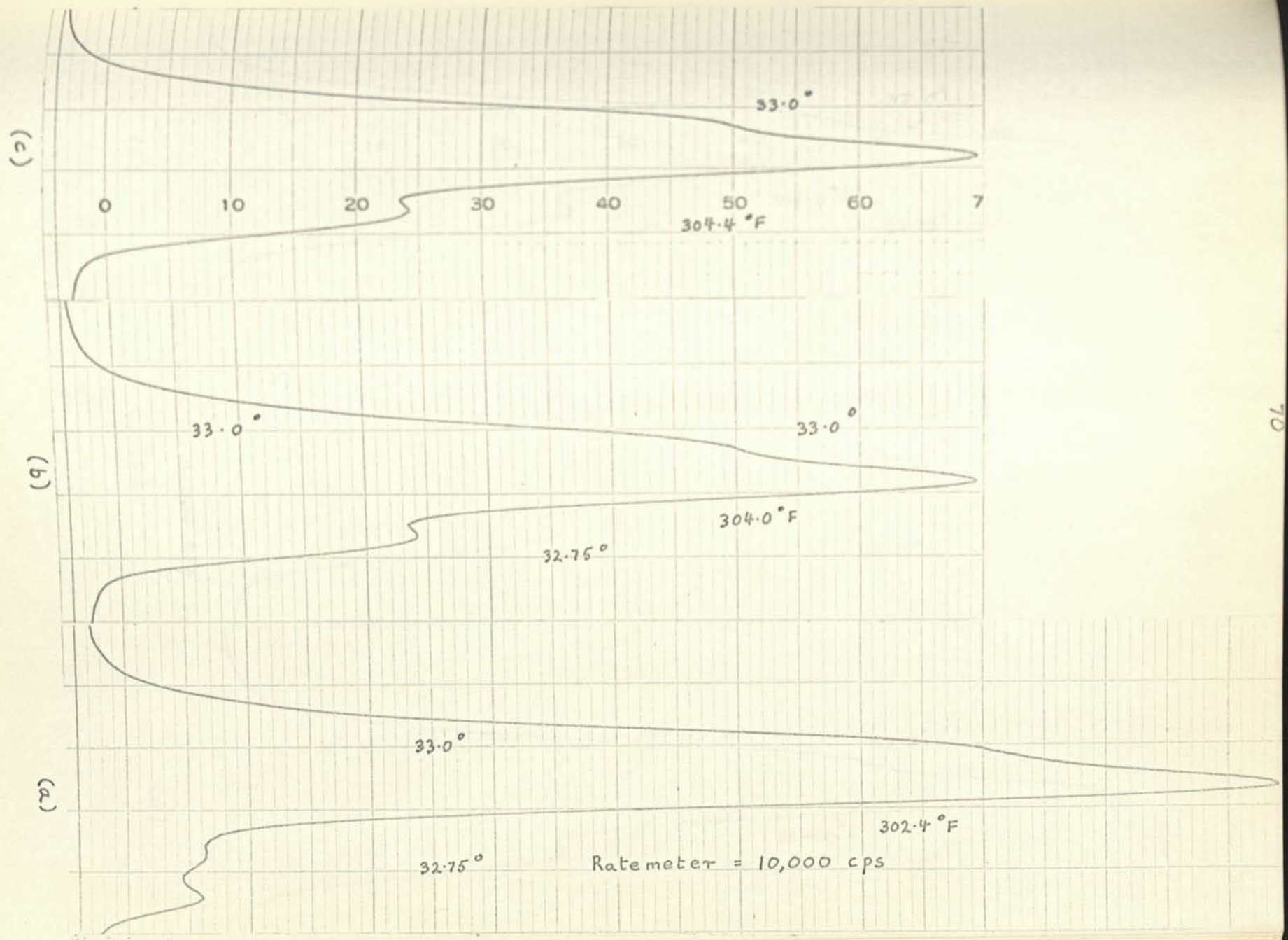
(c)
33·0°
0
10
20
30
40
50
60
7
304·4 °F
(b)
33·0°
33·0°
304·0 °F
32·75°
33·0°
(a)
302·4 °F
32·75°
Ratemeter = 10,000 cps

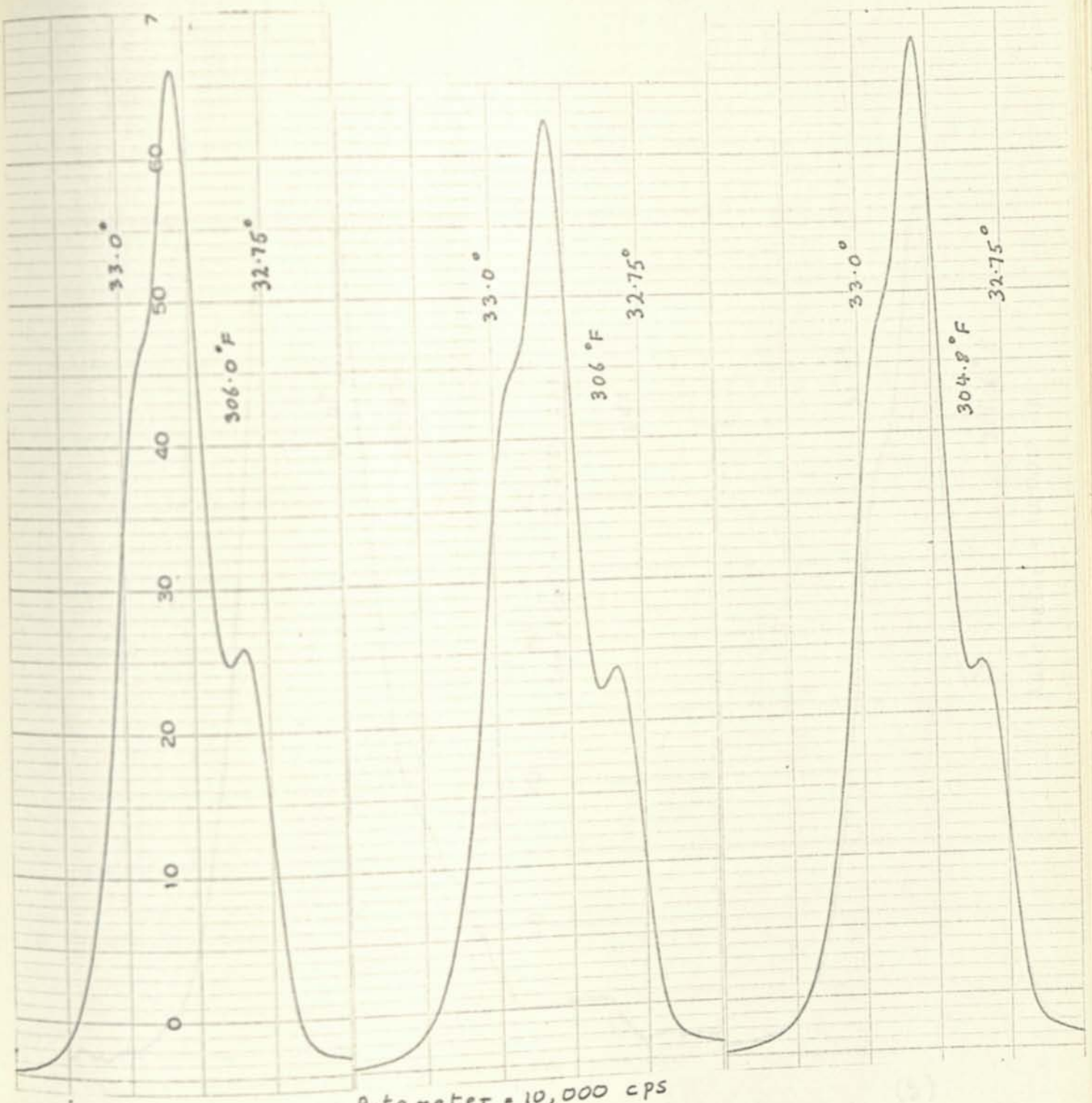

Rate meter = 10,000 cps

(f) (e) (d)

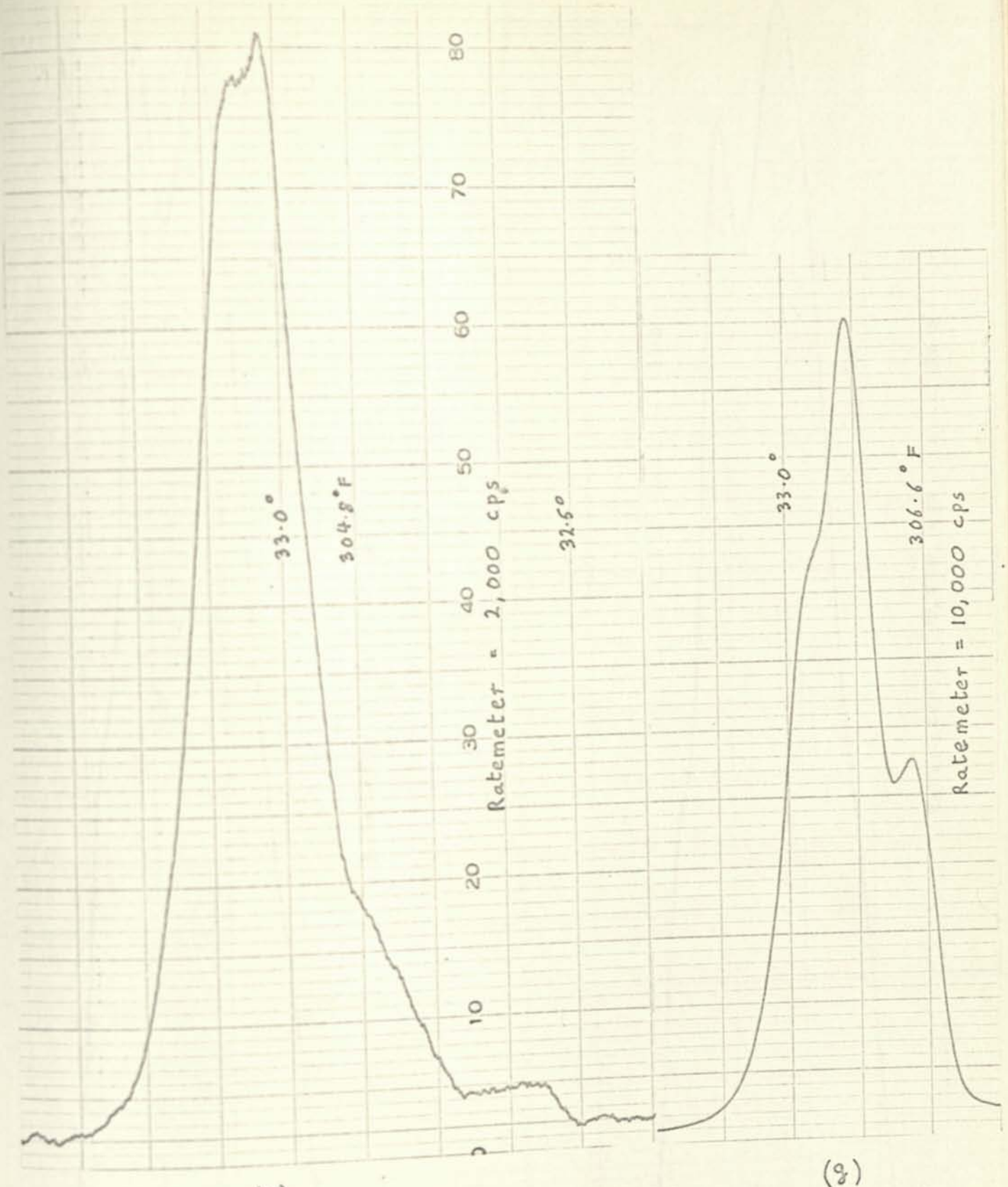
80
70
60
50
40
30
20
10
0
Ratemeter = 2,000 cps
33.0°
304.8°F
32.6°
33.0°
306.6°F
Ratemeter = 10,000 cps

(h) (g)

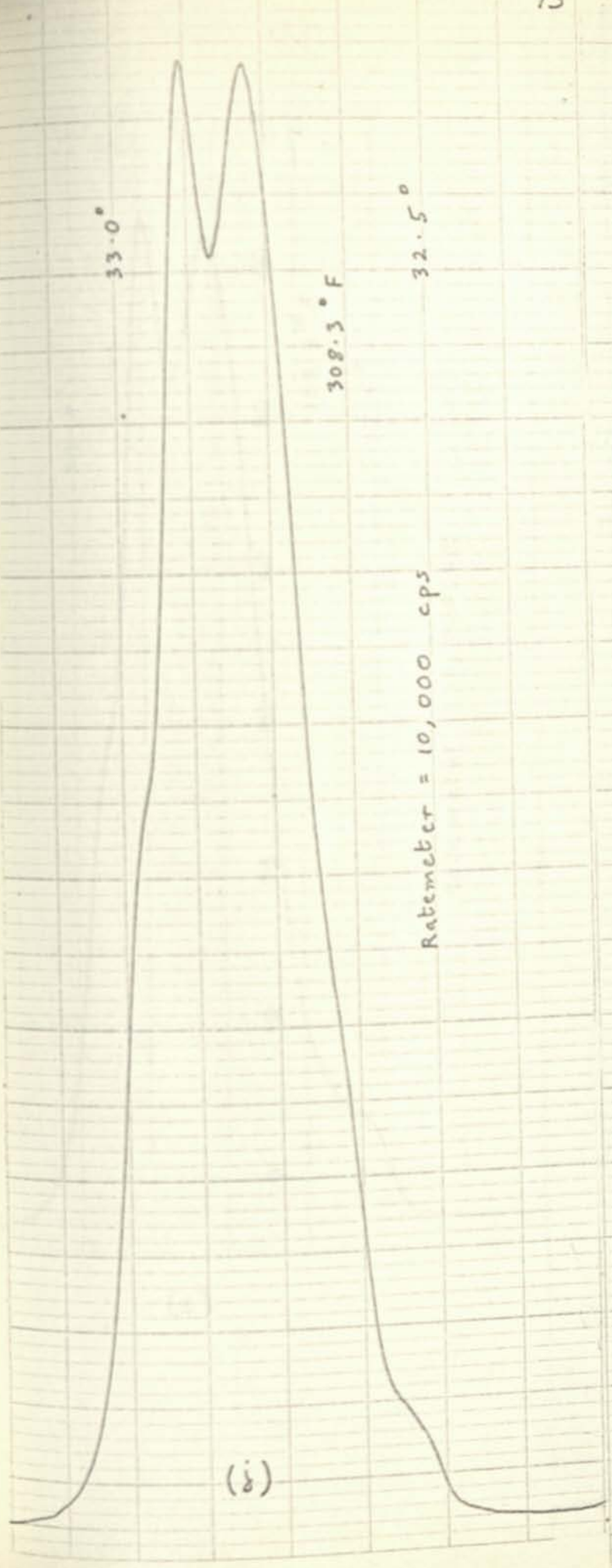
33·0°
308·3 °F
32·5°
Ratemeter = 10,000 cps
(ii)

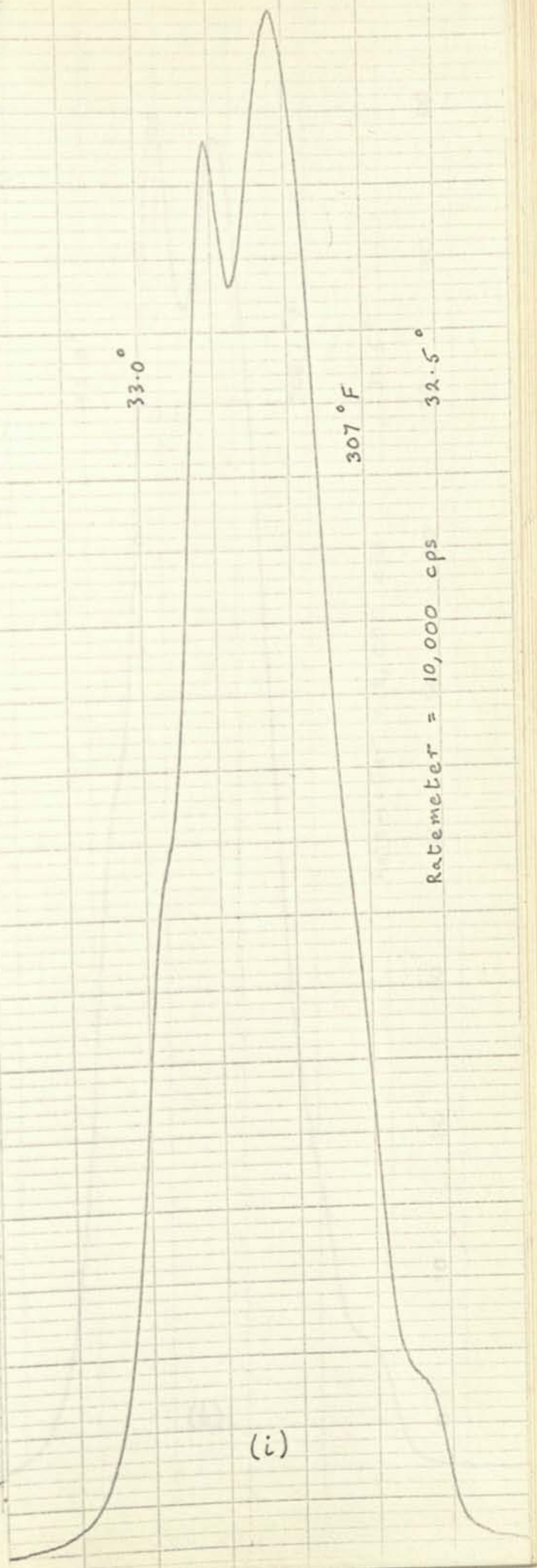
33·0°
307 °F
32·5°
Ratemeter = 10,000 cps
(i)

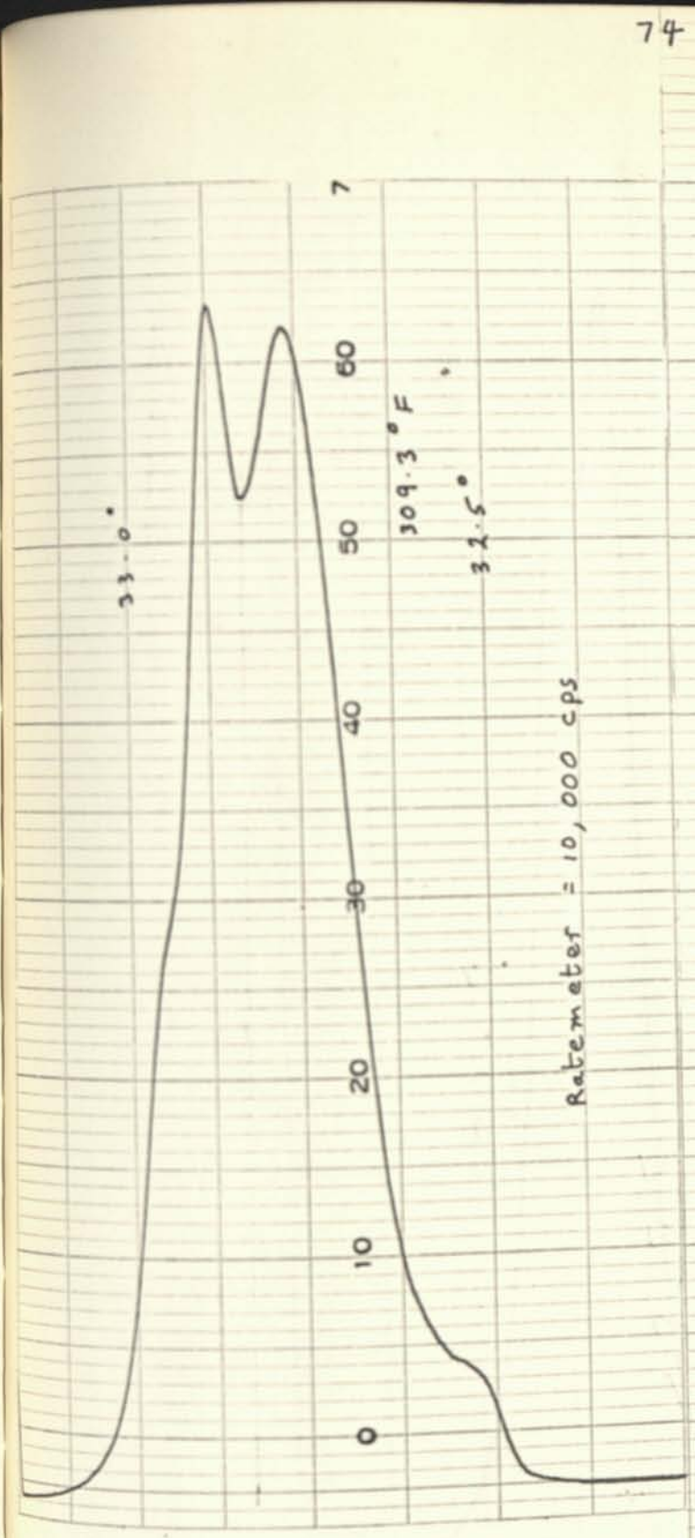
33.0°
309.3°F
32.5°
Ratemeter = 10,000 cps
0
10
20
30
40
50
60
70

(L)

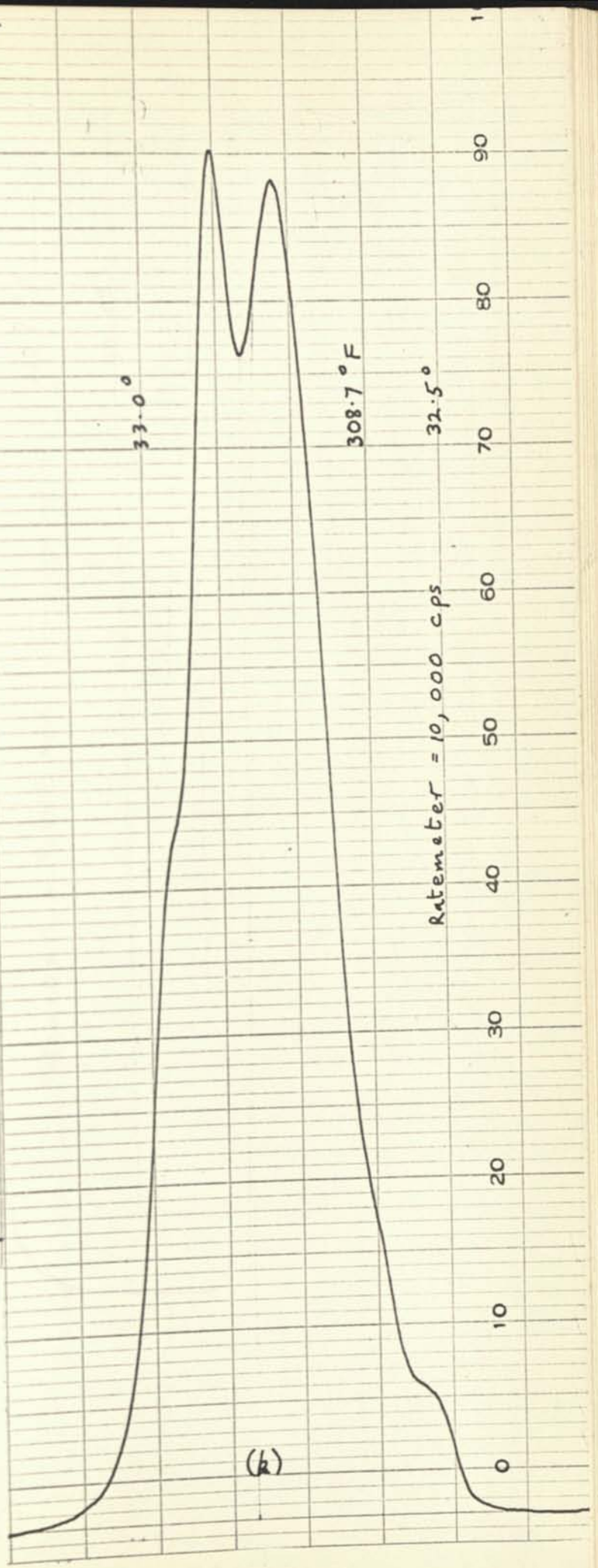
33.0°
308.7°F
32.5°
Ratemeter = 10,000 cps
0
10
20
30
40
50
60
70
80
90

(k)

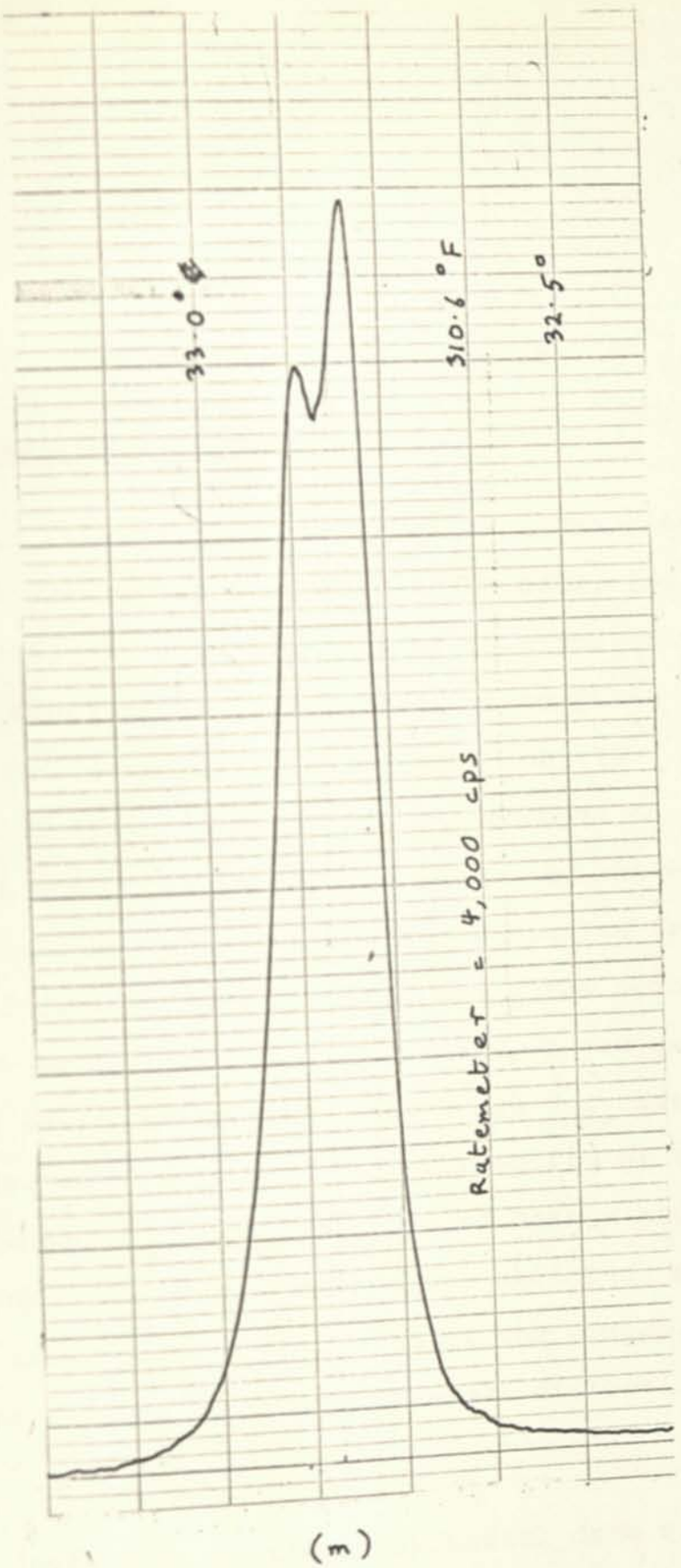

(3)

CHAPTER 5

INTERPRETATION OF RESULTS

Thermal Cell Distortion

In Table 2, d_{hkl} is given as a function of the principal axes x and z of the indium cell, for each order of diffraction. Figures 40 to 46 show the change of d_{hkl}, δd, as a function of temperature, as computed from the experimental data for Δ, using Equation (1). δd could be analysed in order to determine the changes in lattice parameters δx and δz in one of two ways. By one method, best values could be found for the two variables from the seven pieces of data by data fitting, using the method of least squares. By a second method, x and z are measured from the peak shifts of those planes whose d_{hkl} are functions of x only, or of z only. The peak shifts of the remaining planes, whose d_{hkl} are functions of both x and z, are used as a check. The second method was selected, since data fitting does not take into account the probability that there are factors other than thermal distortion effecting d_{hkl}.

Inspection of the experimental data reveal two

obvious anomolies. The 101 plane gave a substantial step change in peak intensity, and thermally concurrent peak width and angle displacements. Also the 112 plane had positive peak displacements. We note that from Table 2,

$$\delta d_{002} = 0.5\delta z \tag{18}$$

$$\delta d_{110} = 0.707\delta x \tag{19}$$

$$\delta d_{200} = 0.5\delta x \tag{20}$$

Using Equation 18 and 19, δd_{hkl} was calculated for the four remaining planes. The results are compared on Figures 40, 43, 45 and 46. It is noted that the agreement is quite good for the 103 and 211 planes, and for the 101 plane outside the anomolous region. Poorer agreement is obtained using the value of δx obtained from Equation 20, due, no doubt, to the low intensity of the peak diffracted by the 200 plane.

Crystal Characteristic Length and Long Range Disorder

Crystal characteristic length is calculated according to Equation 6. The value of L calculated gives an order of magnitude for the individual crystal size, but also includes two other effect:

1) Some machine broadening of the peak may be present. If this is equal to δB, then the true characteristic crystal

Figure 40 Change in d_{111} with Temperature

Experimental

Calculated From δx and $\delta \alpha$

δd Å

+0.025
+0.02
+0.015
+0.01
+0.005
+0.001
0

291 295 300 305 310 311

Temperature °F

BL

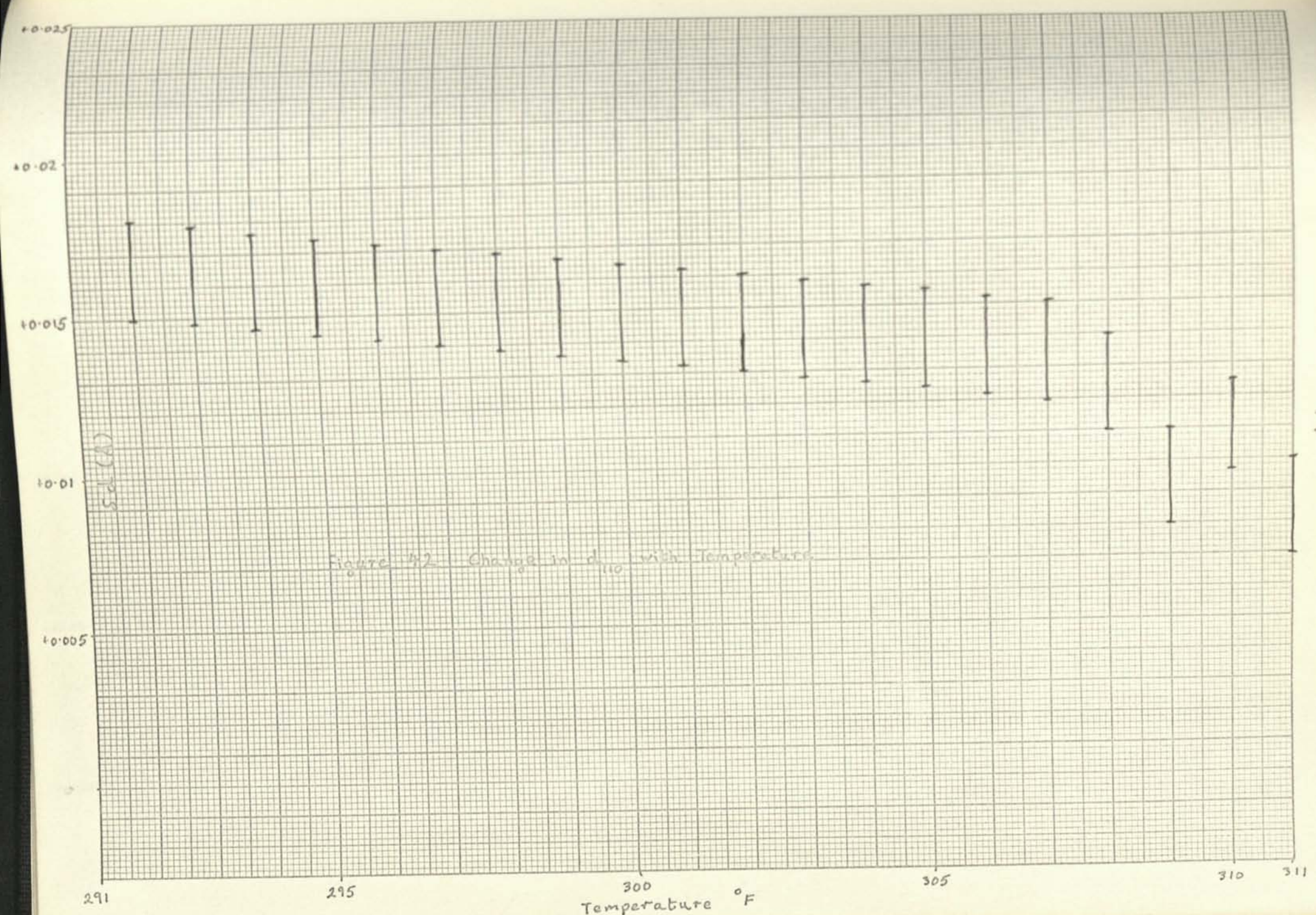

Figure A2: Change in d_{110} with Temperature

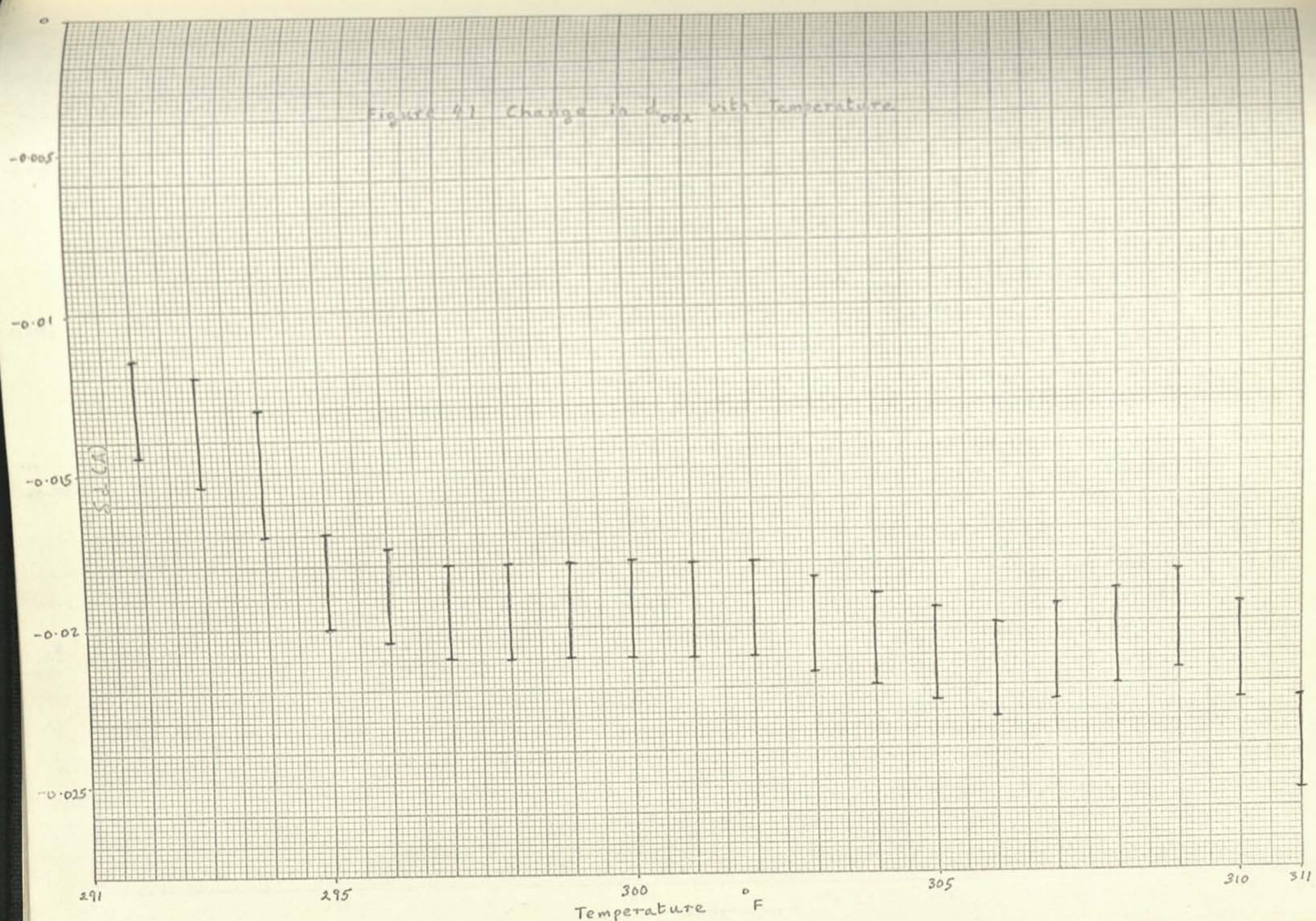
Figure 41 Change in d_{002} with Temperature
0
-0.005
-0.01
-0.015
-0.02
-0.025
Δd (Å)
291
295
300
305
310
311
Temperature °F

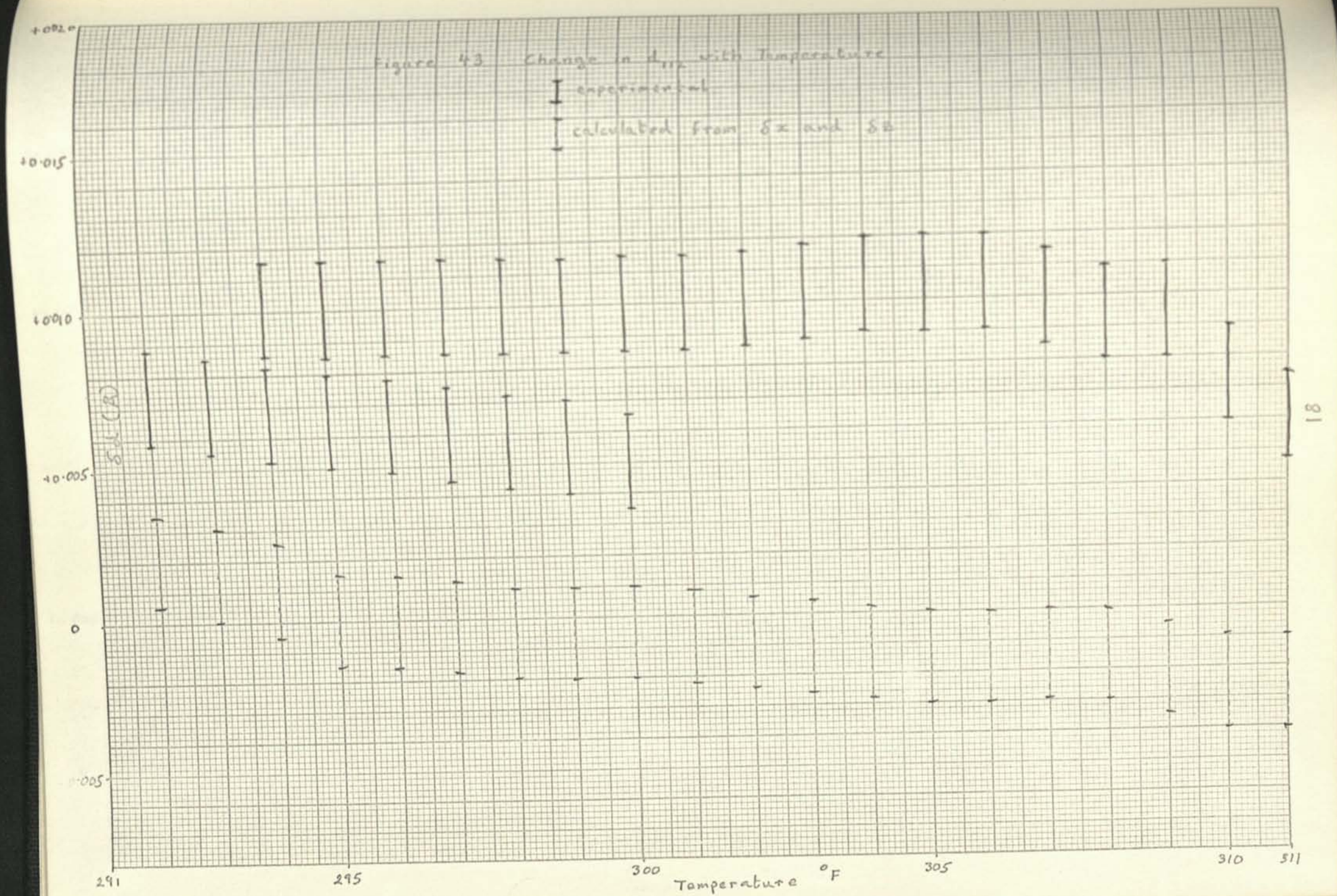
Figure 43 Change in d_{111} with Temperature
experimental
calculated from δx and δB
+.002
+.015
+.010
+.005
0
-.005
δd_{111} (Å)
291
295
300
305
310
311
Temperature °F

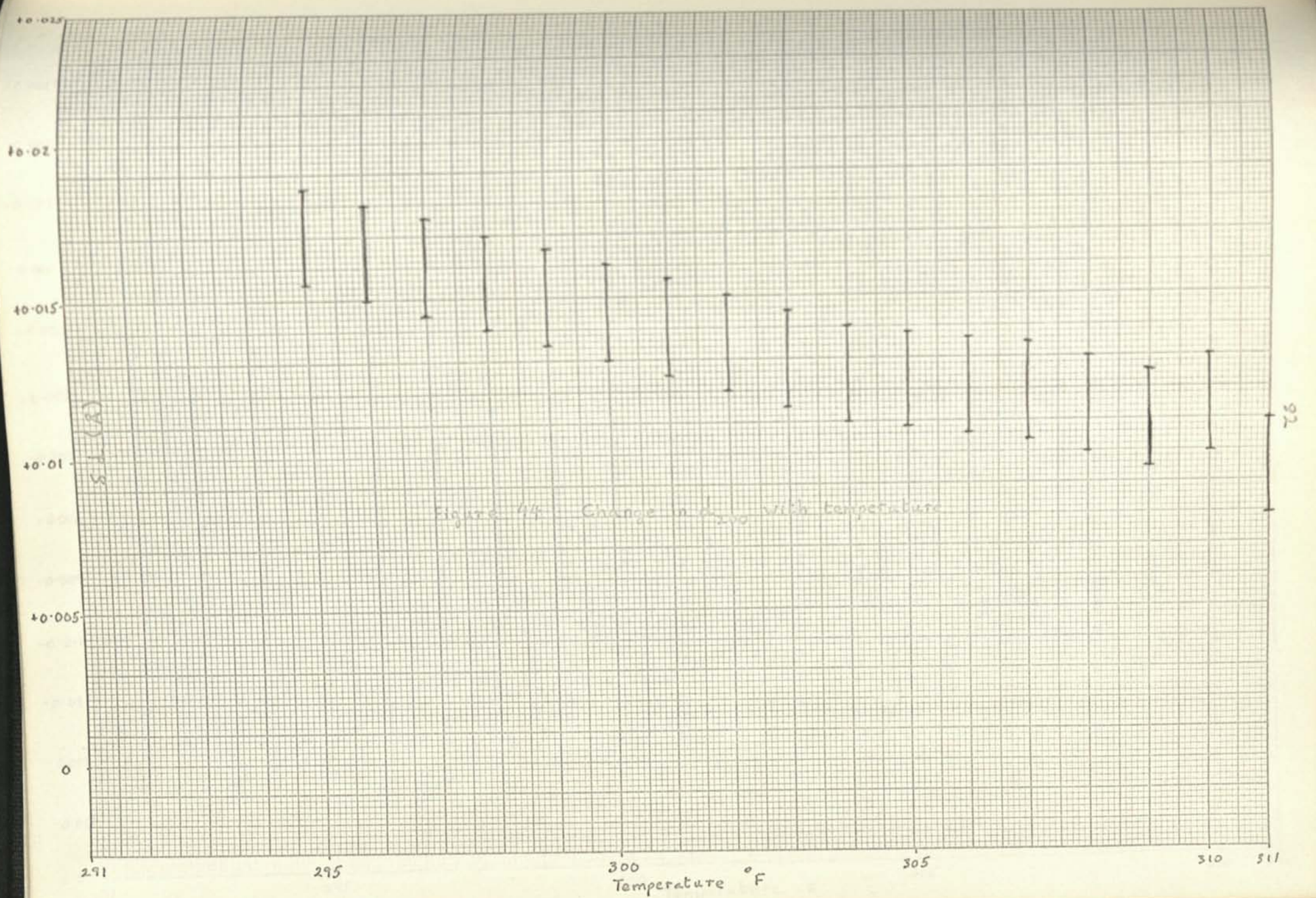

Figure 44 Change in d_{220} with temperature

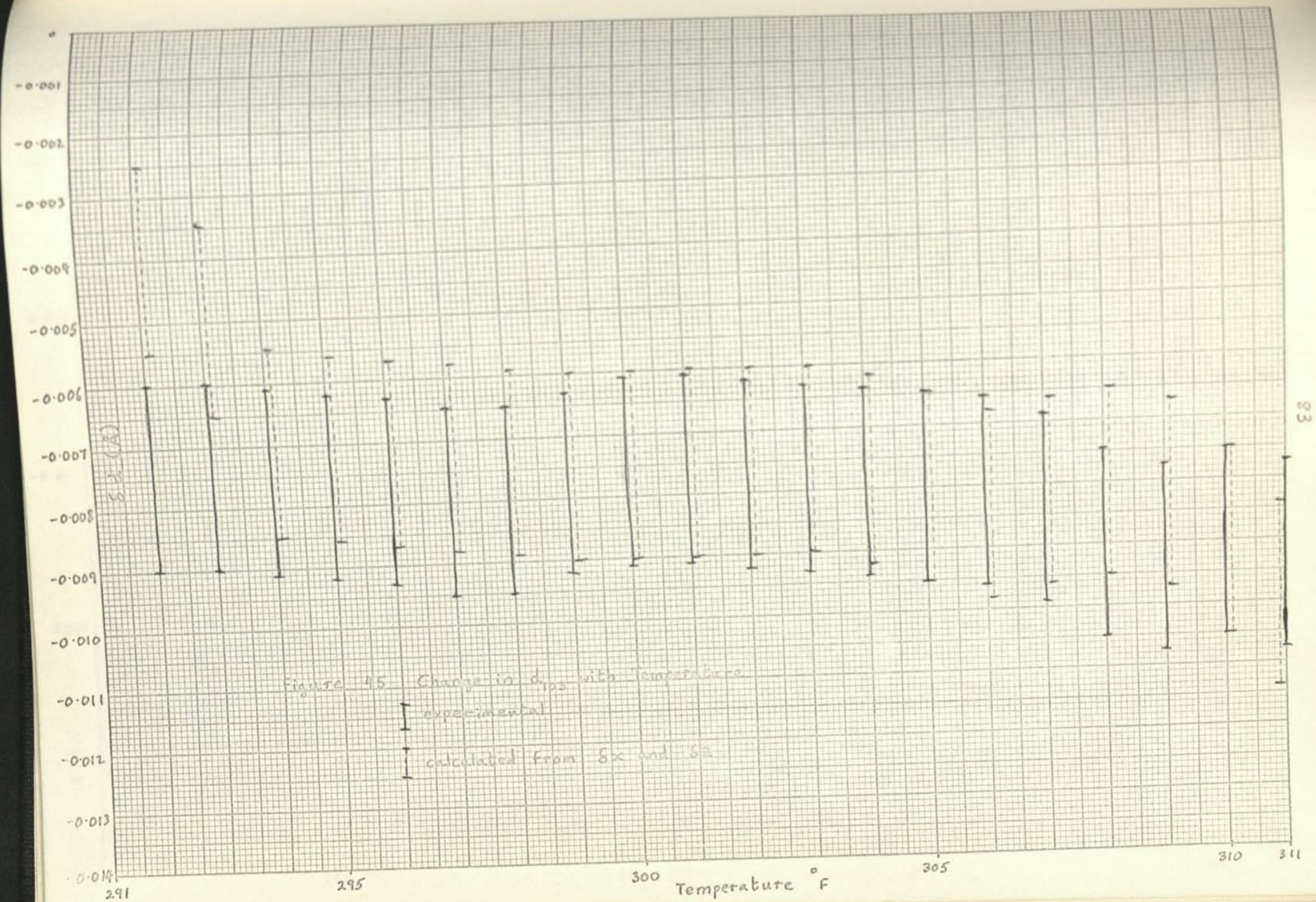

Figure 45 Change in d_{105} with temperature

experimental

calculated from δx and $\delta \alpha$

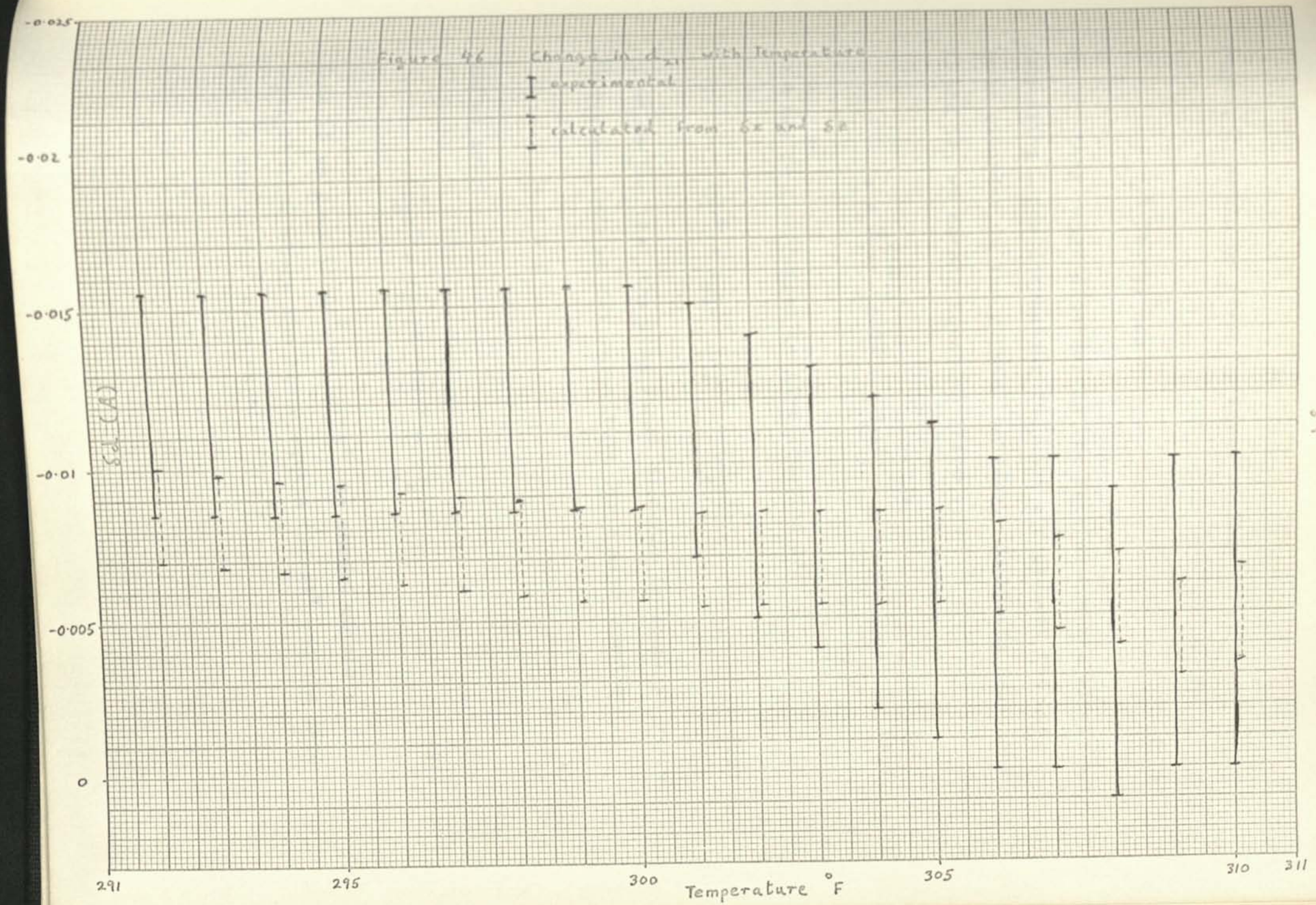

Figure 46 Change in d_{331} with Temperature

I experimental

I calculated from δx and δz

length, $\bar{L}$, would be given by Equation 21:

$$\bar{L} = \frac{\lambda}{(B-\delta B)\cos\theta} \tag{21}$$

2) Long range disorder in the lattice has the effect of decreasing L for increasing 2θ. Let ϕ represent the long range disorder in the crystal lattice. Combining Equations 11 and 12, we obtain Equation 22 for ϕ:

$$\phi = \frac{d^{2/3}}{\pi}\left[(\frac{1}{L})^2 - (\frac{1}{L^x})^2\right]^{1/4} \tag{22}$$

This may be rearranged to give Equation 23:

$$(\frac{1}{d})^6 = (\frac{1}{\pi\phi})^4\left[(\frac{1}{L})^2 - (\frac{1}{L^x})^2\right] \tag{23}$$

If we assume that the long range disorder is equal in every direction, than we may substitute for ϕ with Equation 24:

$$\phi = \mu d \tag{24}$$

and we get:

$$(\frac{1}{d})^2 = (\frac{1}{\pi\mu})^4\left[(\frac{1}{L})^2 - (\frac{1}{L^x})^2\right] \tag{25}$$

Thus if we plot $(1/d)^2$ vs $(1/L)^2$, we should obtain a straight line where the slope equals $(1/\pi\mu)^4$ and the intercept on the $(1/L)^2$ axis equals $(1/L^x)^2$.

On Figure 47, $(1/L)^2$ is plotted against $(1/d)^2$ for cold indium, and at 295°F, 305°F and 311°F. From the data, no temperature effect may be discerned. If we assume that $\delta B = 0$, then from Figure 47, we obtain the results that:

$$L^x = \bar{L} = 5760 \text{ Å}$$

$$\mu = 1.325 \times 10^{-3}$$

$$\bar{a}/a = 1.000612$$

so long range order disappears over 1647 unit cells, which is of the same order of magnitude of L^x, the characteristic crystal length calculated for the undisordered crystal.

It should be noted that the scatter of the data points on Figure 47 is due largely to the uncertainty of deducing peak width due to α_1 radiation only, from the measured peak width due to α_1 and α_2 radiation combined.

Some measure of the machine peak broadening is given from the calculated value of $\bar{L}$. δB could be calculated, and an adjusted value of L used in Equation 25, to produce a second estimate of δB, and so forth. The data, however, are too scattered for such a procedure to be rewarding.

It is of interest to find out what the effect of recooling the crystal is. Peak widths and 2θ angles were measured for the recooled peaks. Weighting the type 2

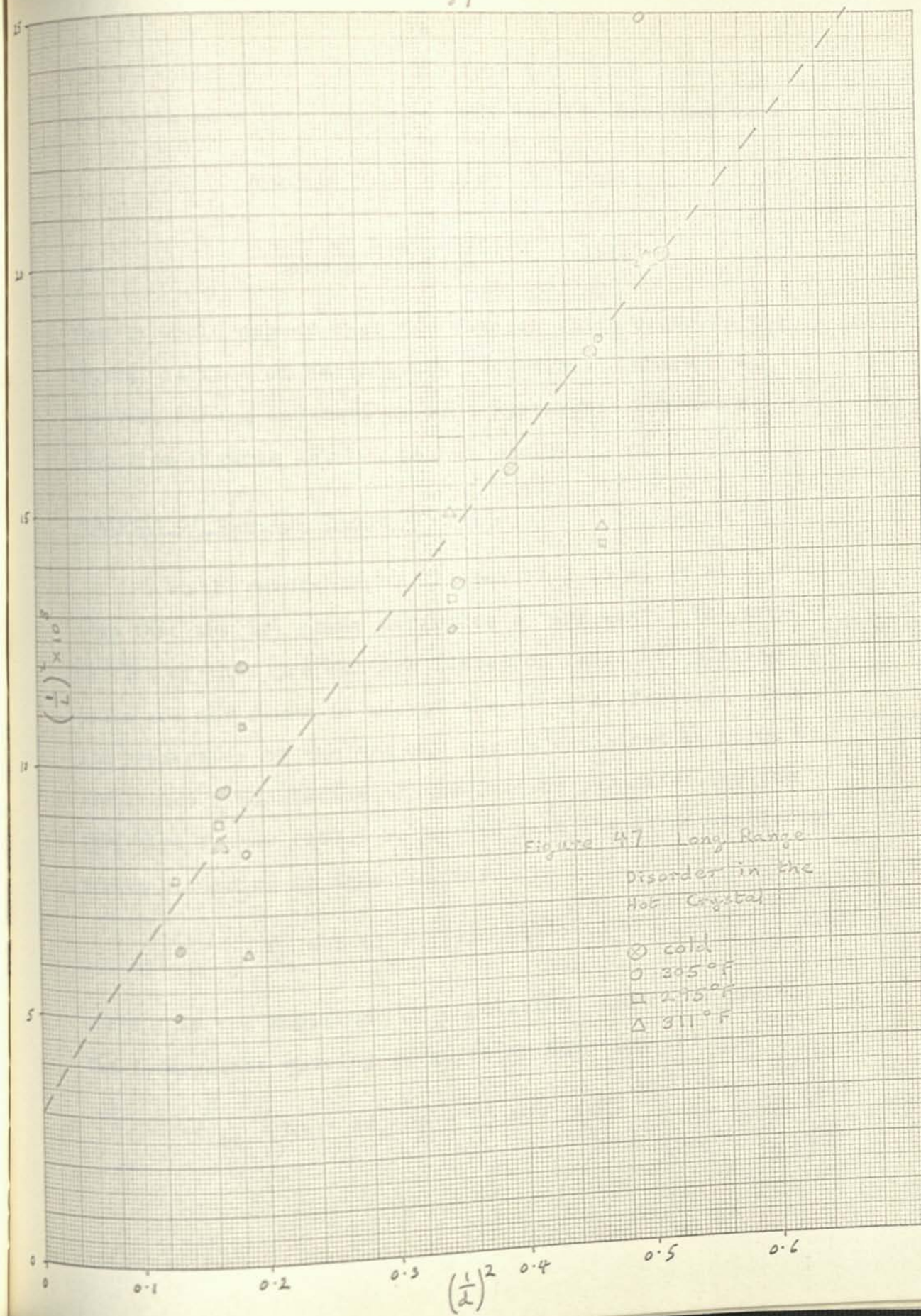

Figure 47 Long Range Disorder in the Hot Crystal

runs by a factor of 5 over the type 1

runs which were less reliable, the results obtained were:

Average peak shift	nil
$\frac{\text{Recooled peak width}}{\text{cold peak width}}$	1.02

Thus it would appear that the changes which occur in the crystal lattice on heating are reversible. There are, however, strong indications of a hysterysis effect, as seen from Figures 16, 18, 19, 21 and 25.

Analysis of the 101 Plane Prepeak

With reference to Figures 39 a to m, it will be seen that the 101 plane diffracts a "prepeak". The properties of this prepeak are listed on Table 4. Similar peaks are not found in any of the other diffraction lines. The properties of the prepeak may be explained in terms of simultaneous modulation of the lattice parameter and the structure factor (20). We assume that the structure factor varies according to Equation 26:

$$f_n = f\left(1 + \eta \sin \frac{2\pi na}{\Lambda}\right) \tag{26}$$

where η is the amplitude of modulation, and Λ the period. The interplanar spacing is given by Equation 27:

$$d_{101} = na + \Delta d_n = na - \frac{\Lambda\varepsilon}{2\pi} \cos 2\pi \frac{na}{\Lambda} \tag{27}$$

where ε is the amplitude of modulation. It is essential to have a sine term in one expression and a cosine term in the other so that the maximum of f_n corresponds to the maximum spacing. The diffracted amplitude is the transform of the function representing the distribution of matter, or

$$F(x) = \bar{f}\ (1 + \eta \sin \frac{2\pi x}{\Lambda}) \sum_n \delta\ (x-x_n) \tag{28}$$

This transform is tedious, but available in the literature (20). It is found that a pair of satellite peaks accompany each node, situated at $\pm\ 1/\Lambda$, with intensity ratios:

$$(\frac{A\varepsilon s + \eta}{2})^2 \text{ for satellite } s = \frac{n}{a} - \frac{1}{\Lambda}$$
$$(\frac{A\varepsilon s - \eta}{2})^2 \text{ for satellite } s = \frac{n}{a} + \frac{1}{\Lambda} \tag{29}$$

Since the satellite for $s = \frac{n}{a} + \frac{1}{\Lambda}$ is of such low intensity as not to be discernable, we may conclude that η is given by Equation 30:

$$\eta = A\varepsilon s \tag{30}$$

and thus:

$$\frac{I'}{I} = (A\varepsilon s)^2 \text{ for } s = \frac{n}{a} - \frac{1}{\Lambda} \tag{31}$$

From the constant value obtained for the prepeak displacement

from 101 node, we calculate that

$$A = 850 \text{ Å}$$

Thus we obtain values of ϵ and η from Equations 26 and 27, as presented in Figure 48. From Figure 48 we may note the following:

1) Both ϵ and η change sharply at $307^{\circ}F$.

2) Above $307^{\circ}F$, $\eta = 1$.

3) If the slopes of the two curves below 306° were maintained, both ϵ and η would approach zero at about $100^{\circ}F$.

One explanation of these results would be that lattice vacancies are ordering normal to the 101 plane. A lattice vacancy would give rise to a zero structure factor, or $\eta = 1$. Such a result would be in agreement with the findings of Eckert and Drickamer (23), except that these workers did not observe anomolously large self diffusion until about $309^{\circ}F$. Jack and Sebba (9) working with very pure gallium, concluded that melting is initiated and propagated along the principal plane of reflection of gallium. It is possible that gallium also showed ordering of lattice vacancies along the principal axis. Kaplow and Averbach (24) do not have any similar finds for lead. Evidence

Temperature ^{o}F	$(2\theta - 2\theta')$	I'/I
304.0	0.053^{o}	0.38
304.4	0.053^{o}	0.38
304.8	0.053^{o}	0.39
305.7	0.053^{o}	0.44
306.0	0.053^{o}	0.44
306.6	0.053^{o}	0.47
307.0	0.053^{o}	∿1.0
307.7	0.053^{o}	∿1.0
309.0	0.053^{o}	∿1.0
309.3	0.053^{o}	∿1.0
310.3	0.053^{o}	∿1.0

Primed symbols refer to the prepeak.

Table 4 PROPERTIES OF THE PREPEAK DIFFRACTED BY THE 101 PLANE.

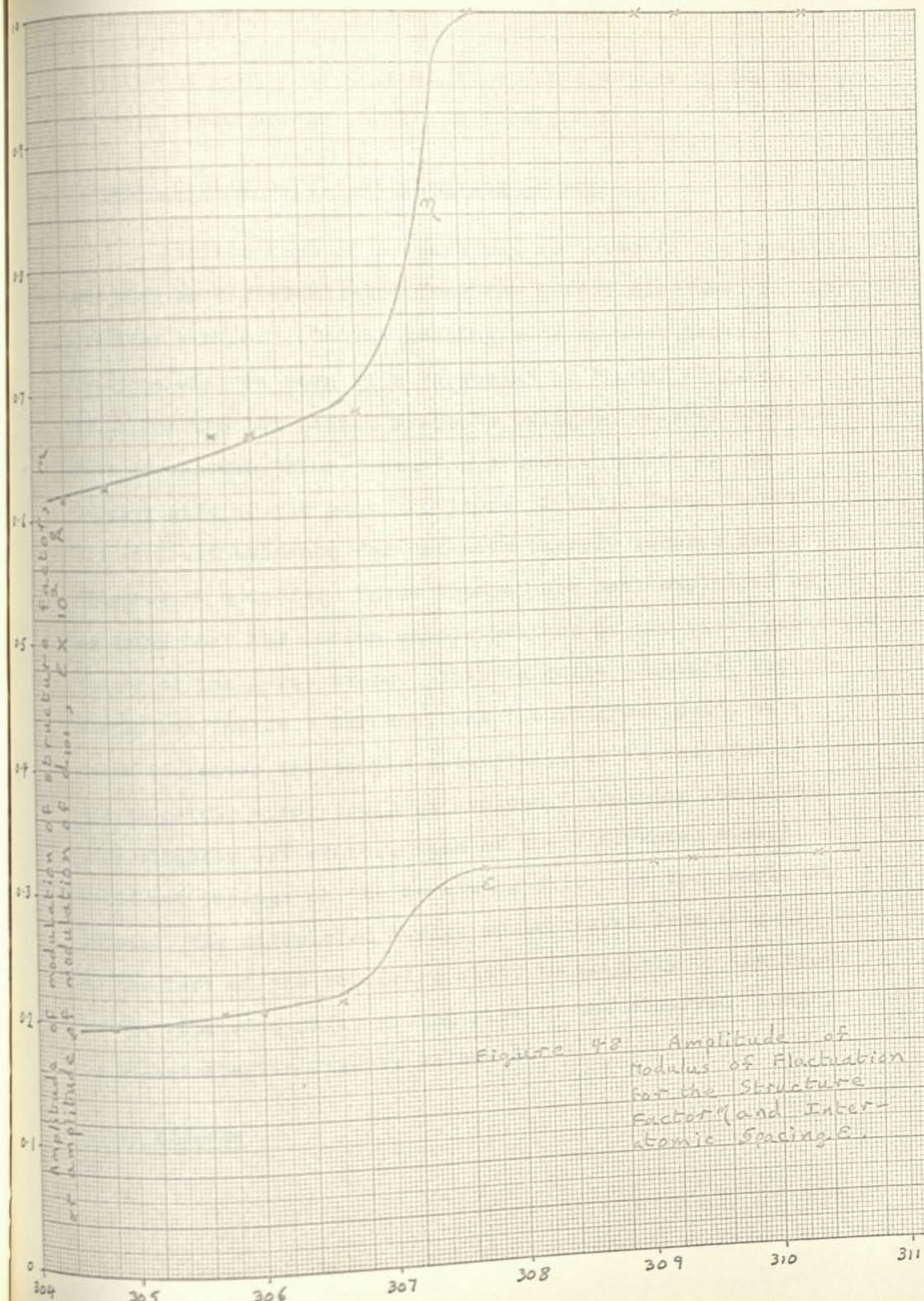

Figure 48 Amplitude of Modulus of Fluctuation and Structure Factor (and Inter-atomic Spacing).

of periodic faults in crystal structures unlike indium are reported elsewhere in the literature (25-28).

Prepeaks Caused by Slight Focusing Errors

Another type of prepeak may be noted in the results, and must be differentiated from the effect discussed in the previous section. On the leading side of most peaks, evidence will be seen of a "prepeak" or "bump" (Figures 32-38). For the 101 plane, prepeaks owing to vacancy ordering have associated "bumps" causing a double "bump" on the leading side of the peak. (Figure 32 (a)) These "bumps" are in least evidence for the most sharply focused peaks (Figures 39 a to f). These "bumps" are best explained by assuming that the indium sample was not at the exact geometric center of the X-ray table. This is quite probable, for the sample was inside a furnace, and though great pains were taken to center the sample accurately, it is doubtful if all geometric error could be avoided. Assuming the sample were slightly off center, some of the diffracted X-rays would not impinge on the receiving slit. As the sample was rotated, the diffracted X-rays would travel from slightly to the left of the receiving slit, to slightly to the right of the receiving slit, giving rise to the observed "bump", as illustrated in Figures 49 and 50.

Other Effects

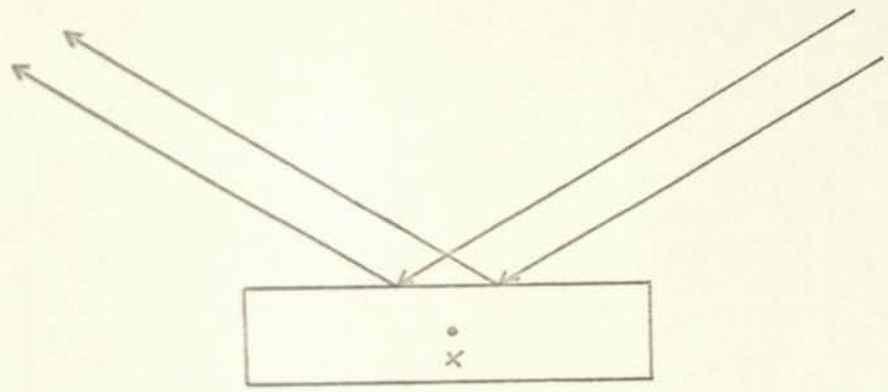

(a) Point of correct orientation

• correct axis
x incorrect axis

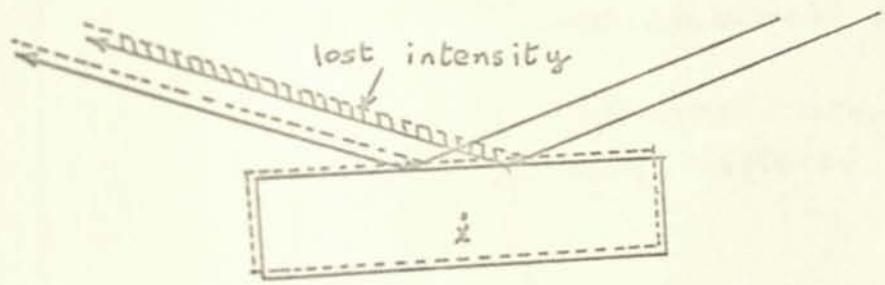

(b) Any other orientation

Figure 49 INTENSITY LOST DUE TO INCORRECT CENTERING.

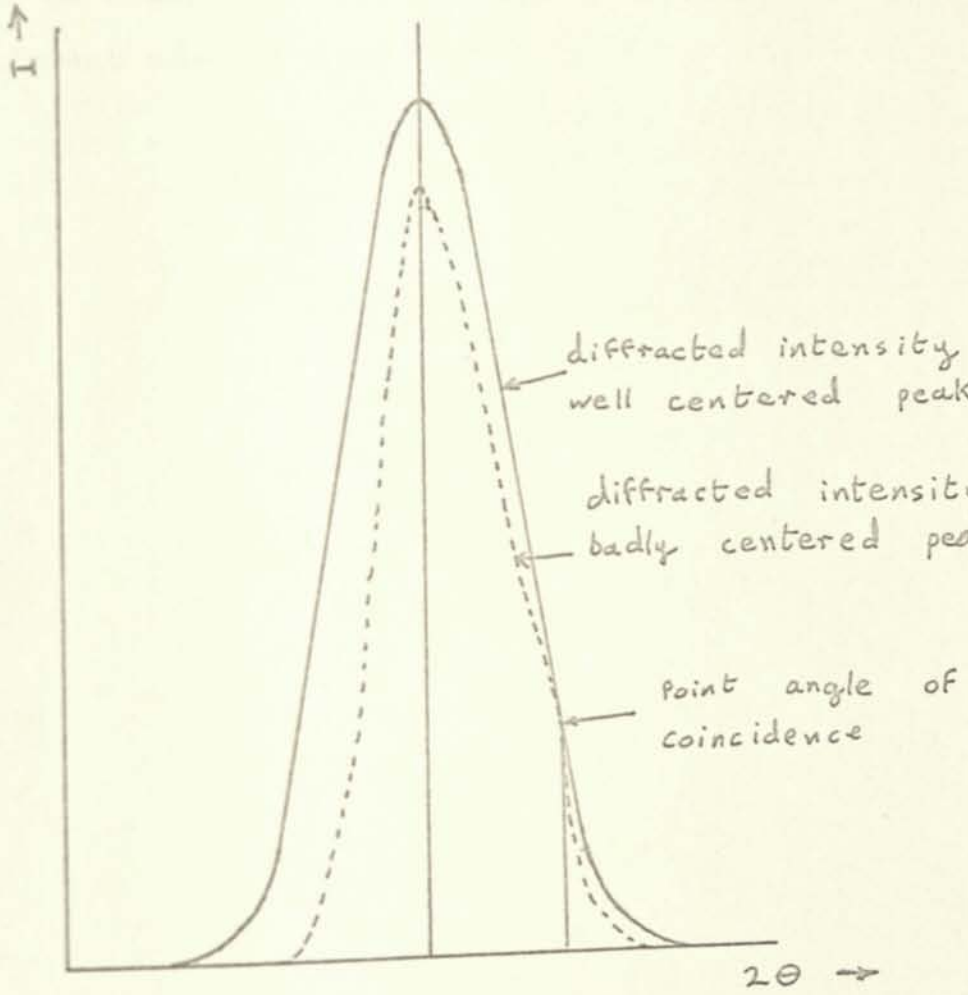

Figure 50 DIFFRACTED INTENSITY FOR A BADLY CENTERED TARGET.

No indications were found of lattice distortion or stacking faults. Phase changes for gallium have been reported (9), and might be expected in induim. However, such changes were found to occur over temperature intervals as small as 0.005°F, which was too fine to be picked up by the equipment used in this work.

CONCLUSION

Melting in indium metal is accompanied by an expansion of the unit cell and a tendency for the rectangular cell to become cubic. The actual breakdown of the lattice on melting originates on, and is propagated along the 101 plane, by the development of self diffusion.

SUMMARY OF RESULTS

Lattice Parameter Changes

The X unit cell parameter (3.2517 Å) increased by 0.7% at 290°F, and by 0.4% at the melting point.

The Z unit cell parameter (4.951 Å) decreased by 0.52% at 290°F, and by 0.97% at the melting point.

The above percentages are subject to ± 10% error. We note the trend towards a cubic structure.

101 Peak Shape

Evidence was found of modulation of structure factor and interatomic spacing along the principal 101 plane. This modulation could be interpreted as the ordering of large numbers of lattice vacancies normal to the 101 plane.

Crystal Size and Long Range Disorder

An approximate cold crystal characteristic length of 5760 Å was calculated. The interplanar spacings were found to vary by approximately 0.06%. No increase in long range disorder was discerned, and the almost complete reversibility of crystal size indicated little crystal

growth on heating. The last point is in agreement with the finding of Kaplow and Averbach (24) for lead.

NOMENCLATURE

A	Amplitude
a	Period of unperturbed lattice
$\bar{a}$	Mean value of a
B	Peak width
d	Interplanar distance
f_n	Structure factor of n^{th} lattice site.
h(x)	Probability density function
I	Intensity
I_o	Cold Intensity
L	Crystal charateristic length
L^x	Cold crystal characteristic length
$\bar{L}$	Mean value of L
n	Any integer
R	Resistance of heating element
s	Surface area per foot of heating element (Pg. 20) $\frac{n}{a} \pm \frac{1}{-}$ (Pg. 89)
Δs	Contribution of long range disorder to L
x	Minor axis of crystal lattice
y(t)	Structure factor function
z	Major axis of crystal lattice

GREEK LETTERS

α	Constant
Δ	Change in 2θ angle
ϵ	Small variation in 2θ (Pg. 10) Amplitude of molulation of planar spacing (Pg. 88)
η	Amplitude of structure factor modulation
θ	Angle of X-ray diffraction
Λ	Period of structure factor modulation
λ	X-ray wave length
μ	ϕ/d
ϕ	Phase difference (Pg. 11) Long range disorder probability density function (Pgs. 15 and 86)
Ω	Electrical resistance

SUPERSCRIPTS

'	Prepeak

SUBSCRIPTS

hkl	Miller indices

BIBLIOGRAPHY

1. Lindemann, F. A., Phys. Z.11, 609, 1910.

2. Frenkel, J., Acta Physicochim 3, 913, 1935.

3. Frenkel, J., J. Chem. Phys. 7, 538, 1939.

4. Frenkel, J., "Kinetic Theory of Liquids", Oxford University Press, 1946.

5. Brillouin, L., Phys. Rev. 54, 916, 1938.

6. Ubbelohde, A. R., Trans. Far. Soc. 34, 292, 1938.

7. Roberts, J. K., Proc. Roy. Soc. A. 106, 385, 1924.

8. Hachkovsky, V. F. and Streklov, P. G., Nature 139, 715, 1937.

9. Jack, J. and Sebba, F., Trans. Far. Soc. 50, 226, 1954.

10. Oldham, J. W. H. and Ubbelohde A. R., Proc. Roy Soc. 176, 50, 1940

11. Siol, M., Z. Physik 164, 93, 1961.

12. Lennard-Jones, J. E. and Devonshire, A. F. Proc. Roy. Soc. 170, 464, 1939.

13. Hermans, J. J., Rec. Trav. Chim. Pays-Bas. 63, 5, 1944.

14. Hosemann, R., Z. Physik 128, 1 and 465, 1950.

15. Eshelby, J. D., J. Appl. Phys. 25, 255, 1954.

16. Feder, R. and Nowick, A. S., Phys. Reviews 109, 1959.

17. Lukasik, S. J., J. of Chem. Phys. 27, 523, 1957.

18. Ludwig, M. T., "Indium", Indium Corporation of America 1959.

19. "Index to the X-ray Powder Data File (1962)", American

Society for Testing and Materials Publication 48-L.

20. Guinier, A., "X-ray Diffraction in Crystals, Imperfect Crystals and Amorphous Bodies", W. H. Freeman and Co. 1963.

21. Wagner, C. N. J., Tetelman, A. S. and Otte, H. M. J. Appl. Phys. 33, 3080, 1962.

22. Schultz, J. M., "Temperature-Sensitive X-ray Small Angle Scattering from Melt Crystallized Polyethylene" Ph.D. Dissertation, Carnegie Inst. of Technology, 1965.

23. Eckert, R. E. and Drikamer, H. G., J. Chem. Phys. 20, 13, 1952.

24. Kaplow, R., Averbach, B. L. and Strong, S. L., J. Phys. Chem. Solids 25, 1195, 1964.

25. Daniel, V. and Lipson, H., Proc. Roy. Soc. A 181, 368, 1943.

26. Chao, S. H. and Taylor, W. H., Proc. Roy. Soc. A 176, 76, 1940.

27. Daniel, V. and Lipson, H., Proc. Roy. Soc. A 182, 378, 1944.

28. Saunder, D. H., Proc. Roy. Soc. A 188, 31, 1946 A 190, 508, 1947.